TU WIEN
DEPARTMENT OF GEODESY
AND GEOINFORMATION
CLIMATE AND ENVIRONMENTAL REMOTE SENSING

DISSERTATION

über

Estimating vegetation productivity from microwave satellite observations

ausgeführt am Department für Geodäsie und Geoinformation,
Forschungsgruppe Klima- und Umweltfernerkundung
zum Zwecke der Erlangung des akademischen Grades einer

DOKTORIN DER NATURWISSENSCHAFTEN (DR.RER.NAT.)

unter der Leitung von
Univ.Prof. Dr.rer.nat. Wouter Arnoud Dorigo, MSc

eingereicht an der Technischen Universität Wien,
Fakultät für Mathematik und Geoinformation
von

Mag. Irene Eva Teubner, MSc

Matrikelnummer: 0502603
Rosenhügel 10
2214 Auersthal

Wien, am 4. November 2021   . . . .

TU WIEN
DEPARTMENT OF GEODESY
AND GEOINFORMATION
CLIMATE AND ENVIRONMENTAL REMOTE SENSING

DISSERTATION

on

Estimating vegetation productivity from microwave satellite observations

submitted at the Department of Geodesy and Geoinformation,
Research Group Climate and Environmental Remote Sensing,
carried out for the purpose of obtaining the degree of

DOCTOR OF NATURAL SCIENCES (DR.RER.NAT.)

under the supervision of
Univ.Prof. Dr.rer.nat. Wouter Arnoud Dorigo, MSc

Research conducted at the Technische Universität Wien,
Faculty of Methematics and Geoinformation,
by

Mag. Irene Eva Teubner, MSc

Matrikelnummer: 0502603
Rosenhügel 10
2214 Auersthal

Vienna, 4. November 2021 ....

Supervisor & Reviewer Univ.Prof. Dr.rer.nat. Wouter Arnoud Dorigo, MSc

Department of Geodesy and Geoinformation

Vienna University of Technology

Wiedner Hauptstraße 8 / E120-01-2, 1040 Vienna

Austria

Reviewer Asst.Prof. Alexandra Konings, Ph.D. M.S.

Department of Earth System Science

Stanford University

473 Via Ortega, Stanford, California 94305

United States of America

Reviewer Prof. Rasmus Fensholt, Ph.D. M.Sc.

Department of Geosciences and Natural Resource Management

University of Copenhagen

Øster Voldgade 10, DK-1350 Copenhagen K

Denmark

Parts of the present work have been published in peer-reviewed journals:

Teubner, I. E., Forkel, M., Jung, M., Liu, Y. Y., Miralles, D. G., Parinussa, R., van der Schalie, R., Vreugdenhil, M., Schwalm, C. R., Tramontana, G., Camps-Valls, G., and Dorigo, W. A. Assessing the relationship between microwave vegetation optical depth and gross primary production. *International journal of applied earth observation and geoinformation*, 65:79–91, 2018. doi: 10.1016/j.jag.2017.10.006.

Teubner, I. E., Forkel, M., Camps-Valls, G., Jung, M., Miralles, D. G., Tramontana, G., van der Schalie, R., Vreugdenhil, M., Mösinger, L., and Dorigo, W. A. A carbon sink-driven approach to estimate gross primary production from microwave satellite observations. *Remote Sensing of Environment*, 229:100–113, 2019. doi: 10.1016/j.rse.2019.04.022.

Teubner, I. E., Forkel, M., Wild, B., Mösinger, L., and Dorigo, W. Impact of temperature and water availability on microwave-derived gross primary production. *Biogeosciences*, 18(11):3285-3308, 2021. doi: 10.5194/bg-18-3285-2021.

In addition to the presented work in my thesis, I have contributed to the following papers during my PhD which are published in or submitted to peer-reviewed journals:

Forkel, M., Dorigo, W., Lasslop, G., **Teubner, I.**, Chuvieco, E., and Thonicke, K. A data-driven approach to identify controls on global fire activity from satellite and climate observations (SOFIA V1). *Geoscientific Model Development*, 10(12):4443-4476, 2017. doi: 10.5194/gmd-10-4443-2017.

Vreugdenhil, M., Wagner, W., Bauer-Marschallinger, B., Pfeil, I., **Teubner, I.**, Rüdiger, C., and Strauss, P. Sensitivity of Sentinel-1 backscatter to vegetation dynamics: An Austrian case study. *Remote Sensing*, 10(9):1396, 2018. doi: 10.3390/rs10091396.

Wild, B., **Teubner, I.**, Moesinger, L., Zotta, R.-M., Forkel, M., van der Schalie, R., Sitch, S., and

Dorigo, W. A. VODCA2GPP - a new global, long-term (1988-2020) GPP dataset from microwave remote sensing. *Earth System Science Data Discussions*, 1-37, 2021. doi: 10.5194/essd-2021-209.

This work has been conducted as part of the following research project:

Erklärung zur Verfassung der Arbeit

Author's Statement

Hiermit erkläre ich, dass ich diese Arbeit selbstständig verfasst habe, dass ich die verwendeten Quellen und Hilfsmittel vollständig angegeben habe und dass ich die Stellen der Arbeit (einschließlich Tabellen, Karten und Abbildungen), die anderen Werken oder dem Internet im Wortlaut oder dem Sinn nach entnommen sind, auf jeden Fall unter Angabe der Quelle als Entlehnung kenntlich gemacht habe.

I hereby declare that I independently drafted this manuscript, that all sources and references are correctly cited, and that the respective parts of this manuscript – including tables, maps, and figures – which were included from other manuscript or the internet either semantically or syntactically are made clearly evident in the text and all respective sources are correctly cited.

<div align="center">

Mag. Irene Eva Teubner, MSc

Rosenhügel 10

2214 Auersthal

</div>

Wien, am 4. November 2021 . . . .

Acknowledgments

Thesis abstract

Vegetation optical depth (VOD) from microwave remote sensing observations has been increasingly used for large-scale monitoring of vegetation dynamics in recent years. Since VOD is sensitive to the vegetation water content, and microwave observations at lower frequencies are not affected by cloud cover (Woodhouse, 2005), VOD holds additional information on the vegetation layer than optical remote sensing data. To which extent the VOD signal can be used to derive certain vegetation properties, however, is still focus of ongoing research. In this PhD thesis, the relationship between VOD and gross primary production (GPP) is analyzed for the purpose of deriving a conceptual model for estimating GPP based on VOD (VOD-GPP model).

For assessing the potential of VOD for estimating GPP, VOD observations from different microwave frequencies, from active and passive sensors and from single sensor or merged products were analyzed and compared with state-of-the-art global remote sensing data sets and in situ GPP estimates. Accordingly, the VOD-GPP model was derived, which represents a carbon sink-driven approach. It consists of a combination of bulk VOD and change in VOD for describing the temporal dynamic and the grid-cell median VOD as a static component representing differences in vegetation cover. Results showed in general good agreement between VOD-based GPP and other GPP estimates. Differences were observed between frequencies, yielding overall best performance with X-band VOD for this application. Results further demonstrated that VOD-based GPP estimates tend to overestimate GPP compared with other global data sets. This behavior was assumed to be related to the lack of temperature dependence of autotrophic respiration in the model formulation. The addition of temperature as further model input could partly reduce the GPP overestimation. An analysis of the impact of water availability demonstrated, however, that the VOD-based GPP estimates are not significantly related to varying conditions of dryness and wetness in large parts of the world, and thus further supports the applicability of the VOD-GPP model.

To conclude, the VOD-GPP model provides an independent, remote sensing based GPP data set that is capable of monitoring vegetation dynamics. Through its sink-driven perspective, it further offers complementary information on carbon related vegetation dynamics than commonly used source-driven approaches. The VOD-GPP model may thus contribute to further our understanding of large-scale responses of vegetation to environmental changes.

Kurzzusammenfassung

Die optische Tiefe der Vegetation (VOD) - ein Parameter, der sich aus Beobachtungen von Fernerkundungssatelliten im Mikrowellenbereich ableitet - hat in den letzten Jahren für die großräumige Auswertung der Vegetationsdynamik an Bedeutung gewonnen. Durch den Zusammenhang zwischen VOD und dem Wassergehalt der Vegetation sowie dem vernachlässigbaren Einfluss der Bewölkung für Mikrowellenbeobachtungen im unteren Frequenzbereich (Woodhouse, 2005), liefert VOD zusätzliche Informationen über die Vegetationsschicht verglichen mit Fernerkundungsdaten im optischen Wellenlängenbereich. Inwieweit das VOD-Signal zur Ableitung bestimmter Pflanzeneigenschaften genutzt werden kann, ist jedoch noch Gegenstand der laufenden Forschung. Diese Arbeit befasst sich mit dem Zusammenhang zwischen VOD und der Bruttoprimärproduktion (GPP) und stellt ein konzeptionelles Modell zur Ermittlung von GPP auf Basis von VOD vor.

Um das Potential von VOD für die Berechnung von GPP zu untersuchen, wurde VOD aus verschiedenen Mikrowellenfrequenzen, aus aktiven und passiven Sensoren sowie Produkten von einzelnen Sensoren bzw. aus mehreren Sensoren zusammengesetzt analysiert und mit modernsten globalen Fernerkundungsdatensätzen und in-situ GPP-Schätzungen verglichen. Daraus abgeleitet wurde das VOD-GPP-Modell erstellt, welches darauf basiert GPP indirekt über die Senken für Kohlenstoff im pflanzlichen Kohlenstoffkreislauf zu beschreiben. Das Modell besteht aus einer Kombination von VOD-Signal und der zeitlichen Änderung von VOD, welche die zeitlich-dynamische Komponente darstellt. Hinzu kommt der Median von VOD je Gitterzelle, welcher als statische Komponente die räumlichen Unterschiede in der Vegetationsbedeckung ausgleicht. Die Ergebnisse zeigen eine gute Übereinstimmung zwischen dem VOD-basierten GPP und den globalen GPP-Datensätzen. Es wurden Unterschiede zwischen den Frequenzen beobachtet, wobei insgesamt die besten Ergebnisse für VOD im X-Band des Mikrowellenbereichs für diese Anwendung erzielt wurden. Im Vergleich mit anderen fernerkundungsbasierten globalen GPP-Datensätzen zeigte sich weiter, dass das VOD-basierte GPP dazu tendiert das jährliche GPP zu überschätzen. Eine mögliche Erklärung war, dass die Überschätzung durch die fehlende Temperaturabhängigkeit der autotrophen Respiration bedingt wird. Bei Hinzunahme der Temperatur als Eingangsvariable, konnte jedoch gezeigt werden, dass dieser Effekt die Überschätzung nur teilweise reduzieren konnte. Eine Analyse des Einflusses von Änderungen in der Wasserverfügbarkeit ergab allerdings auch, dass das Modell in weiten Teilen der Welt nicht signifikant mit Änderungen zwischen trockenen und feuchten Phasen korreliert, was die Anwendbarkeit des Modells weiter stärkt.

Insgesamt liefert das VOD-GPP-Modell einen unabhängigen, fernerkundungsbasierten GPP-Datensatz. Durch den Ansatz die Kohlenstoffsenken zu beschreiben, bietet das Modell ergänzende Informationen zur Vegetationsdynamik in Bezug auf den Kohlenstoffkreislauf im Vergleich mit herkömmlichen Ansätzen, welche direkt GPP abschätzen. Das VOD-GPP-Modell kann somit zu einem besseren Verständnis des Einflusses von Umweltveränderungen auf die Vegetation auf globaler Ebene beitragen.

Contents

CONTENTS

List of Figures

List of Tables

Chapter 1

Introduction

1.1 Introduction and motivation

Vegetation optical depth (VOD) has gained much attention in recent years due its capabilities in vegetation monitoring. As VOD is sensitive to the vegetation water content, it has been employed for deriving various applications including estimation of aboveground living biomass (Liu et al., 2011; Chaparro et al., 2019; Wigneron et al., 2020), ecosystem scale isohydricity (Konings and Gentine, 2017), burned area modeling (Forkel et al., 2017, 2019) or potential for drought monitoring (Crocetti et al., 2020), to name a few. The concept of relating VOD and biomass was first introduced by Liu et al. (2011). Taking this concept a step further, VOD is assumed here to provide also a link to gross primary production (GPP).

GPP is the flux of carbon dioxide uptake by plants though photosynthesis (Bonan, 2015). The resulting carbohydrates are utilized by plants to build up biomass (which contributes to net primary production, NPP) and to support autotrophic respiration (Ra):

$$GPP = NPP + Ra \tag{1.1}$$

GPP plays a vital role in the global carbon cycle since the net uptake by plants acts as a natural sink for atmospheric carbon dioxide (Bonan, 2015). Primary production presents the basis of the food chain and is linked to the evolution of oxygen, which is released during photosynthesis (e.g., Bonan, 2015). In addition, carbon dioxide is the most commonly known greenhouse gas (Intergovernmental Panel on Climate Change, 2018) and, therefore, understanding the terrestrial carbon cycle is of key importance in view of climate change studies. For deriving GPP, a major challenge are the observed uncertainties among GPP estimates. They are mostly, but not exclusively, found in the tropical region (Beer et al., 2010; Anav et al., 2015), where the availability of in situ data is scarce (Pastorello et al., 2020). This lack of in situ data in the tropics hampers model evaluation for this region (O'Sullivan et al., 2020). To tackle the complexity of estimating GPP, different and independent methods are necessary. Although various studies have been conducted with this regard over the time (e.g., Beer et al., 2010; Anav et al., 2015; Sitch et al., 2015; MacBean et al., 2018; Badgley et al., 2019; O'Sullivan et al., 2020; Zhang and Ye, 2021), the quantification of absolute GPP and the reduction of GPP uncertainty at the global scale are still topics of ongoing research.

Methods for estimating GPP range from processed-based to data-driven models. Process-based models describe the ecosystem's carbon balance by simulating the underlying biogeochemical processes (Bonan, 2015; Sitch et al., 2015). Data-driven models for estimating GPP often employ machine-

learning or regression methods to estimate GPP (Tramontana et al., 2016; Jung et al., 2020) and usually rely on optical remote sensing data as main input (e.g., Joiner et al., 2013; Jung et al., 2020). These include the light-use efficiency model, where GPP is quantified based on how much of the photosynthetically active radiation is absorbed by plants (Monteith, 1972; Running et al., 2004), and solar induced fluorescence (SIF), where GPP is determined by the amount of fluorescence that is emitted during photosynthesis (Frankenberg et al., 2011; Guanter et al., 2012; Joiner et al., 2013; Sun et al., 2018). In contrast to process-based models, data-driven methods that try to estimate the right-hand side terms, i.e., the sink terms of equation 1.1, however, are often limited to in situ observations and often focus on NPP alone (Clark et al., 2001a; Nunes et al., 2013; Campioli et al., 2016). Making use of VOD from microwave satellite observations, the concept of the VOD-GPP model provides the opportunity to study sink terms in the plant carbon cycle at a large scale and in addition presents an independent, remote sensing-based dataset.

1.2   Theoretical background for VOD

In radiative transfer theory, VOD (or also referred to as τ) is a coefficient that determines the attenuation of radiation due to absorption and scattering as the signal travels through the vegetation layer (Woodhouse, 2005):

$$\tau = \kappa_e h \tag{1.2}$$

where κ_e is the extinction coefficient and h the path through the volume.
With this definition, the transmissivity of the vegetation layer, which describes how much of the incident radiation arrives at the end of the vegetation layer, can be written as (Woodhouse, 2005):

$$\gamma_v = e^{-\frac{\tau}{cos(\Theta)}} \tag{1.3}$$

with the incidence angle Θ.
The retrieval of VOD, however, differs for active and passive microwave sensors, since the observed physical quantities are different in two cases. For active microwave remote sensing, the concept of deriving VOD is commonly described through the water cloud model (Attema and Ulaby, 1978). In the water cloud model, the vegetation water content is treated as a cloud layer (Attema and Ulaby, 1978). The sensor emits a signal and detects the returned signal that has traveled through the vegetation layer to the soil surface and back. The attenuation along the path is expressed through the two terms optical depth τ and single scattering albedo ω (Woodhouse, 2005). The quantity retrieved from radar observations is the normalized backscatter coefficient or normalized radar cross-section σ^0, which is related to the ratio of backscattered to incident power and depends on the object's dielectric properties, shape, orientation and roughness (Woodhouse, 2005). The backscatter coefficient is composed of three terms - contribution of the soil, the vegetation layer and an interaction term - the latter term is commonly considered negligible (Woodhouse, 2005). The formula for σ^0 is then given by (Attema and Ulaby, 1978; Woodhouse, 2005):

$$\sigma^0 = \gamma_v^2 \sigma_{soil}^0 + \sigma_v^0 \tag{1.4}$$

$$\sigma^0 = \gamma_v^2 \sigma_{soil}^0 + cos(\Theta)\frac{3\omega}{4}(1 - \gamma_v^2) \tag{1.5}$$

with $\omega = \frac{\kappa_s}{\kappa_e}$, where κ_s is the backscattering coefficient.

For passive microwave remote sensing, radiation is detected that is emitted from the target object itself according to its brightness temperature T_B. T_B defines the temperature that a blackbody would have if the object had the same brightness as the blackbody. With the Rayleigh-Jeans law, T_B can be expressed as the product of the object's physical temperature T and its emissivity ϵ (Woodhouse, 2005). The detected signal travels through the vegetation layer only once. Total T_B comprises three terms, direct emissions from the surface T_{Bs} and the volume T_{Bv} (vegetation layer), and emissions from the volume that are first scattered at the surface T_{Bvs} (Woodhouse, 2005):

$$T_B = T_{Bs} + T_{Bv} + T_{Bvs} \tag{1.6}$$

$$T_{Bs} = \epsilon_s T_s \gamma_v \tag{1.7}$$

$$T_{Bv} = T_v (1 - \omega)(1 - \gamma_v) \tag{1.8}$$

$$T_{Bvs} = T_v (1 - \omega)(1 - \gamma_v)\Gamma\gamma_v \tag{1.9}$$

with surface emissivity ϵ_s, surface temperature T_s, volume temperature T_v and surface reflectivity Γ.

Microwave frequencies that are commonly used for earth observation are L-band (1-2 GHz), C-band (4-8 GHz), X-band (8-12 GHz) and Ku-band (12-18 GHz). Since the impact of the atmosphere is small below 20 GHz or even negligible below approximately 10 GHz (Woodhouse, 2005), microwave observations for these frequencies are considered independent of cloud cover (Woodhouse, 2005). This provides an advantage over optical remote sensing data, especially in cloud-prone regions like the tropics.

The relation between microwave frequency and size of the considered objects in the vegetation layer plays an important role. Lower frequencies are more sensitive to large plant parts like trunks and branches and exhibit a high penetration depth of the vegetation layer, while higher frequencies correspond to small plant parts like twigs and leaves but show a low penetration depth (Woodhouse, 2005). All together and with a satellite revisit time of up to twice a day, VOD has the advantage that it can provide large-scale observations for monitoring of vegetation dynamics at a relatively high temporal resolution.

1.3   Research Questions

This PhD thesis evolves around the following questions, which were the basis for the analysis in the three papers and the derivation of the conceptual model.

1. Can the relationship between VOD and aboveground biomass be used to derive a relationship between VOD and GPP?

2. How can a potential relationship between VOD and GPP be described?

3. What input variables are required for estimating GPP based on VOD?

4. What impact does the microwave frequency have on the relationship between VOD and GPP?

5. Do active and passive microwave observations yield similar performance with regard to the GPP estimation?

6. Which frequency is best suited for this application?

7. Does the VOD-based GPP estimation hold true under variations in dry- and wetness conditions?

1.4 Paper summaries

1.4.1 Paper 1: Assessing the relationship between microwave vegetation optical depth and gross primary production

The potential for estimating GPP based on VOD was investigated by comparing different VOD metrics with GPP estimates, both at a local and global scale. These metrics include the bulk VOD signal (VOD), the change in VOD (ΔVOD) and positive changes in VOD (ΔVOD$\geq$0), and rely on approaches that are used for estimating NPP from in situ biomass data. Although NPP presents only part of the right-hand side of the equation for GPP (Eq. 1.1), it provides a first step for developing the modeling approach. In addition to analyzing the potential of input variables, the question of which frequency is best suited for this application arises. Microwave theory states that the frequency strongly corresponds to the size of the considered objects (Woodhouse, 2005). Therefore, it can be assumed that differences between various frequencies exist. To tackle this question, VOD from different frequencies, ranging from L- to X-band, were analyzed. In addition to correlation analysis, the lag between the variables was determined. Results showed that performance differed with microwave frequency, i.e., higher performance for X- than for L-band, and with land cover classes along a gradient of vegetation density. The analysis of the temporal lag between GPP and VOD metrics demonstrated that none of the metrics yielded a lag of zero and that the sign of the lags were opposite. This suggests that the combination of VOD and ΔVOD is required for describing the relationship between VOD and GPP.

1.4.2 Paper 2: A carbon sink-driven approach to estimate gross primary production from microwave satellite observations

For the model derivation, the concept of combining VOD and ΔVOD is further investigated. Generalized Additive Models (GAM) were chosen as regression method. In GAM, the relationship between each input variable and the response variable is estimated from the data itself and thus does not need to be defined beforehand. This is of advantage, since the relationship between VOD and biomass, which presents the overall basis for this approach, in not known a prior. Another aspect is how regional differences in the vegetation layer are reflected in the model. Since the previous analysis yielded a dependence with vegetation density, the grid cell median VOD (mdnVOD) was introduced as a proxy for land cover. Which microwave frequency is best suited for this application, however, was still an open question. Since performance was found to increase with frequency, the current study focused on higher frequencies extending from C- to Ku-band. In order to assess the general applicability, the model was evaluating against global GPP estimates at each single grid point. This gives a first indication of the potential performance that can be expected. Results showed overall good model performance. It was further found that mdnVOD is required as additional input, which appears to support regional differences in the model. The resulting model formulation thus uses VOD, ΔVOD and mdnVOD as input for estimating GPP. With regard to the used frequencies, results showed overall best performance for X-band VOD. An important further result here was that the model tends to overestimate GPP compared to other global remote-sensing based GPP estimates, which was thus analyzed in the third PhD paper.

1.4.3 Paper 3: Impact of temperature and water availability on microwave-derived gross primary production

Two key aspects in the VOD-GPP model have still not been investigated. This is firstly the tendency for overestimation of annual GPP. It could be assumed that this might be related to the missing temperature dependence for Ra. Like the relationship between VOD and biomass, the relationship for the temperature dependence is difficult to determine explicitly and thus is further implemented via GAM again. Considering the temperature dependence in the model formulation demonstrated that an improvement in performance can be achieved in general. The response in the metrics, however, was found to be regionally different. Further, the bias between VOD-based GPP and other remote-sensing based global GPP products largely increased, especially in mid-latitudes. The second question is, how the model performs under variation in dry- and wetness conditions. Since VOD is sensitive to the vegetation moisture content, it was addressed if the estimation of GPP based on VOD holds true when the plants experience variations in dry- and wetness. To test this, the residuals of source- (GPP from optical remote sensing) and sink-driven (VOD-based GPP) approaches were analyzed with respect to water availability as represented through the Standardized Precipitation and Evapotranspiration Index (SPEI). In the ideal case, this analysis should yield no significant relationship. Analyzing SPEI, non-significant correlations were observed for large areas of the world. In some regions, such as Argentina and the US corn belt, however, a response to variations in SPEI was observed.

1.5 Contribution to the scientific community

The presented sink-driven modeling approach has the potential to provide additional information than models based on optical remote sensing data. Given that both source and sink terms represent robust estimates, it is possible to balance those two terms. Such an approach may contribute to our understanding and description of processes in the carbon cycle, e.g., in terms of aboveground versus belowground dynamics or allocation in general. In addition, it provides the possibility to further our knowledge about the response of vegetation to environmental changes at the global scale.

Chapter 2

Assessing the relationship between microwave vegetation optical depth and gross primary production

2.1 Abstract

At the global scale, the uptake of atmospheric carbon dioxide by terrestrial ecosystems through photosynthesis is commonly estimated through vegetation indices or biophysical properties derived from optical remote sensing data. Microwave observations of vegetated areas are sensitive to different components of the vegetation layer than observations in the optical domain and may therefore provide complementary information on the vegetation state, which may be used in the estimation of Gross Primary Production (GPP). However, the relation between GPP and Vegetation Optical Depth (VOD), a biophysical quantity derived from microwave observations, is not yet known. This study aims to explore the relationship between VOD and GPP. VOD data were taken from different frequencies (L-, C-, and X-band) and from both active and passive microwave sensors, including the Advanced Scatterometer (ASCAT), the Soil Moisture Ocean Salinity (SMOS) mission, the Advanced Microwave Scanning Radiometer for Earth Observation System (AMSR-E) and a merged VOD data set from various passive microwave sensors. VOD data were compared against FLUXCOM GPP and Solar-Induced chlorophyll Fluorescence (SIF) from the Global Ozone Monitoring Experiment-2 (GOME-2). FLUXCOM GPP estimates are based on the upscaling of flux tower GPP observations using optical satellite data, while SIF observations present a measure of photosynthetic activity and are often used as a proxy for GPP. For relating VOD to GPP, three variables were analyzed: original VOD time series, temporal changes in VOD (ΔVOD), and positive changes in VOD (ΔVOD$_{\geq 0}$). Results show widespread positive correlations between VOD and GPP with some negative correlations mainly occurring in dry and wet regions for active and passive VOD, respectively. Correlations between VOD and GPP were similar or higher than between VOD and SIF. When comparing the three variables for relating VOD to GPP, correlations with GPP were higher for the original VOD time series than for ΔVOD or ΔVOD$_{\geq 0}$ in case of sparsely to moderately vegetated areas and evergreen forests, while the opposite was true for deciduous forests. Results suggest that original VOD time series should be used jointly with changes in VOD for the estimation of GPP across biomes, which may further benefit from combining active and passive VOD data.

2.2 Introduction

Vegetation plays an important role in the Earth system as plants take up atmospheric carbon dioxide through photosynthesis and transport water from the soil into the atmosphere through transpiration (Lambers et al., 2008). In addition, vegetation can influence the Earth's surface energy balance through differences in surface albedo compared to bare soil or snow cover, which is especially pronounced for boreal forests (Bonan, 2008). Therefore, monitoring the vegetation state in terms of photosynthetic activity as well as plant water status is of importance for hydrological, ecological and climate change applications (Bonan, 2015).

The uptake of atmospheric carbon dioxide by vegetation through photosynthesis is commonly referred to as Gross Primary Production (GPP) and is the largest carbon flux in the global carbon cycle (Ciais et al., 2013). GPP can be determined at site level from eddy covariance measurements of carbon dioxide net exchange, which is partitioned into GPP and ecosystem respiration (Baldocchi et al., 2001; Reichstein et al., 2005; Jung et al., 2011; Lasslop et al., 2012). Another approach is the biometric method, which combines estimates of plant growth, chamber flux measurements and stock inventories (Campioli et al., 2016). GPP can be assessed from local to global scales using process-based models that describe the canopy light absorption and the energy and enzyme limitations of the carboxylation rate to estimate gross carbon assimilation (e.g. Farquhar et al., 1980; Collatz et al., 1992). However, current process-based models show large uncertainties because of a limited understanding of the processes that are involved in photosynthesis (Rogers et al., 2017). Alternatively, data-driven approaches that combine satellite observations with empirical models can be used to estimate GPP at large scales (Beer et al., 2010).

Most of the approaches to estimate GPP from satellite observations use optical data to characterize biophysical properties or photosynthetic activity. Biophysical properties such as the Fraction of Absorbed Photosynthetically Active Radiation (FAPAR) are used in light-use efficiency models to estimate GPP, assuming a linear relationship between FAPAR and GPP which is modulated by temperature and water stress (Monteith, 1972; Nemani et al., 2003). Additionally, machine learning algorithms, driven by meteorological and/or satellite data, have been used to upscale site-level observations of GPP (Beer et al., 2010; Jung et al., 2011; Tramontana et al., 2016). Alternatively, Solar-Induced chlorophyll Fluorescence (SIF), an estimate of photosynthetic activity, has been proposed as a global proxy for GPP in recent years (Frankenberg et al., 2014; Guanter et al., 2014; Damm et al., 2015; Zhang et al., 2016b).

Optical remote sensing data, however, are often affected by clouds and aerosols (Myneni et al., 2002; Forkel et al., 2013) and sun-sensor geometry (Dorigo, 2012; Morton et al., 2014). A common method to reduce the influence of cloud cover on optical data is temporal compositing (Huete et al., 2011; Holben, 1986), which decreases the native temporal resolution. Alternatively, time series filtering can be applied (Chen et al., 2004).

In contrast to optical data, microwave radiation below a frequency of 10 GHz is less influenced by clouds and is independent of the sun as source of illumination (Woodhouse, 2005). Microwave satellite observations over vegetation are thus able to provide crucial information in areas with extensive cloud cover like the tropics or high latitudes. The penetration depth of the microwave radiation into the vegetation canopy depends on frequency, dielectric properties, size and geometry of the interacting vegetation parts. As such, microwave observations from different frequencies theoretically contain information from different parts of the vegetation (Woodhouse, 2005). Whereas high frequencies (short wavelengths) predominantly interact with small structures like leaves and twigs at the top of the

vegetation layer, low frequencies (long wavelengths) can penetrate deeper into the vegetation and are more sensitive to large structures like branches or trunks (Woodhouse, 2005). Accordingly, microwave radiation exhibits a higher penetration depth than optical radiation due to its longer wavelength, and should theoretically be better suited for monitoring denser canopies, as the observed signal does not saturate as quickly as for optical sensors (Woodhouse, 2005; Dorigo et al., 2007). Therefore, microwave satellite observations have the potential to provide valuable information on the vegetation state complementary to optical satellite data which are traditionally used for estimating GPP.

Microwave Vegetation Optical Depth (VOD) describes the attenuation of radiation due to scattering and absorption within the vegetation layer, which is caused by the water contained in the vegetation (Woodhouse, 2005). At low biomass, VOD is linearly related to the vegetation water content (VWC; expressed in kg/m^2) (Jackson and Schmugge, 1991; Woodhouse, 2005). In addition, VOD can be related to aboveground living biomass (Liu et al., 2015; Tian et al., 2016) and to Leaf Area Index (LAI), especially in crop- and grasslands (Zribi et al., 2011; Kim et al., 2012; Sawada et al., 2015).

VOD data have been analyzed for different applications such as long-term trends in biomass (Andela et al., 2013; Liu et al., 2013a,b, 2015), forest loss (Van Marle et al., 2016), phenology metrics (Jones et al., 2011, 2012), vegetation water stress (Miralles et al., 2016), evaporation retrievals (Miralles et al., 2011; Martens et al., 2016) and ecosystem resilience (Verbesselt et al., 2016). However, short-term variations in VOD have not been assessed with regard to GPP.

The aim of this study is to explore the relationship between VOD and GPP and assess if VOD can provide additional information about GPP on top of what is provided by SIF. In addition, this study investigates the effect of different microwave frequencies (between 1 and 10 GHz) and of active and passive sensors (hereafter referred to as active and passive VOD) on the relationship between VOD and GPP.

2.3 Data and methods

2.3.1 Vegetation remote sensing data

The analysis is based on five VOD data sets, upscaled GPP estimates, and SIF observations (Table 3.1). The data sets have different temporal coverage with a common overlap of about one year. The period from January 2007 to December 2015 was selected in order to obtain a minimum number of four years of overlap with the GPP data set.

VOD ASCAT

Active microwave VOD data were retrieved from microwave backscatter measurements of the Advanced Scatterometer (ASCAT) onboard the meteorological operational satellite A (MetOp-A). ASCAT measures backscatter at 5.25 GHz (C-band) in vertical co-polarization. The retrieval of VOD is based on slope estimates of the angular backscatter dependency, which are calculated during the soil moisture retrieval using the TU-Wien change detection algorithm. VOD is obtained by relating the angular sensitivity of measured backscatter to the sensitivity of modelled bare soil backscatter (Melzer, 2013; Vreugdenhil et al., 2016, 2017) and, therefore, represents a measure of volume scattering due to vegetation relative to bare soil volume scattering. VOD is derived jointly from measurements in ascending and descending mode (9:30 a.m./p.m. equatorial crossing).

VOD AMSR-E

Measurements at 6.9 GHz (C-band) and 10.7 GHz (X-band) were used from the Advanced Microwave Scanning Radiometer for Earth Observation System (AMSR-E). For both frequencies, VOD was obtained with the Land Parameter Retrieval Model (LPRM) v06 (van der Schalie et al., 2017). The algorithm uses a radiative transfer model (Mo et al., 1982) and includes an analytical solution for VOD using the Microwave Polarization Difference Index (MPDI) (Meesters et al., 2005). LPRM retrieves VOD and soil moisture simultaneously under the assumption of a globally constant single scattering albedo and further assumes that soil and canopy temperature are similar (Owe et al., 2001). Since the latter assumption generally does not hold for daytime observations, we only used observations from the descending mode for this analysis (1:30 a.m. equatorial crossing).

VOD SMOS

VOD from the Soil Moisture Ocean Salinity (SMOS) radiometer, which provides observations at 1.4 GHz (L-band), was also retrieved with the LPRM v06 (van der Schalie et al., 2016, 2017). Only data from the ascending mode were analyzed (6 a.m. equatorial crossing) as soil and canopy temperatures are usually more similar in the morning than in the late afternoon although seasonal and latitudinal variations exist.

VOD merged

In addition to the single frequency data sets, a merged passive microwave VOD data set developed by Liu et al. (2015) was included in this analysis. For the period 2007-2012, the data set comprises observations from AMSR-E (6.9 GHz, C-band), WindSat (6.8 GHz, C-band), and the FengYun-3B Microwave Radiometer Imager (10.7 GHz, X-band). Prior to merging, the single sensor data sets were rescaled by applying the cumulative distribution function (CDF) matching technique with AMSR-E as the reference (Liu et al., 2009).

GPP FLUXCOM

The FLUXCOM GPP data set presents an upscaling of flux tower measurements based on multiple machine learning algorithms and satellite data (Tramontana et al., 2016). Different remotely sensed data in the optical domain from the Moderate Resolution Imaging Spectroradiometer (MODIS) were used as input, including the Enhanced Vegetation Index (EVI), LAI, band 7 - Middle Infrared Reflectance (MIR), Normalized Difference Vegetation Index (NDVI), and Normalized Difference Water Index (NDWI) (Tramontana et al., 2016).

SIF GOME-2

The GOME-F v26 SIF data were obtained from the Global Ozone Monitoring Experiment-2 (GOME-2) sensor. The retrieval is based on the filling-in of Frauenhofer lines, which is caused by the chlorophyll fluorescence emitted from the Earth's surface (Joiner et al., 2013). The algorithm uses principal components analysis and radiative transfer theory to determine SIF at 740 nm (Joiner et al., 2013, 2014, 2016). In this study, SIF observations from the MetOp-A platform were used.

Table 2.1: Data set overview. Acronyms: Enhanced Vegetation Index (EVI), Leaf Area Index (LAI), MODIS band 7 - Middle Infrared Reflectance (MIR), Normalized Difference Vegetation Index (NDVI), Normalized Difference Water Index (NDWI), and Land Parameter Retrieval Model (LPRM).

Name	Data set	Period used	Frequency/ wavelength/ data input	Spatial resolution	Temporal resolution	Type	Method/ algorithm	Reference
SMOS	SMOS	7/2010 - 12/2015	1.4 GHz	0.25°	Daily	Passive microwave	LPRMv06	van der Schalie et al. (2017)
ASCAT	ASCAT	1/2007 - 12/2015	5.25 GHz	12.5 km	Daily	Active microwave	TU-Wien change detection	Melzer (2013); Vreugdenhil et al. (2016, 2017)
AMSRE_C	AMSR-E	1/2007 - 9/2011	6.9 GHz	0.25°	Daily	Passive microwave	LPRMv06	van der Schalie et al. (2017)
AMSRE_X	AMSR-E	1/2007 - 9/2011	10.7 GHz	0.25°	Daily	Passive microwave	LPRMv06	van der Schalie et al. (2017)
VODmerged	AMSR-E, WindSat, FY-3B	1/2007 - 9/2011, 1/2007 - 6/2012, 11/2010 - 12/2012	6.9 GHz, 6.8 GHz, 10.7 GHz	0.25°	Daily	Passive microwave	LPRMv05	Liu et al. (2015)
GPP	FLUXCOM	1/2007 - 12/2015	MODIS EVI, LAI, MIR, NDVI, NDWI	10 km	8-daily	Optical	Machine learning	Tramontana et al. (2016)
SIF	GOME2_F v26	1/2007 - 12/2015	740 nm	0.5°	Monthly	Optical		Joiner et al. (2013, 2014)

2.3.2 Ancillary data

CCI land cover

The European Space Agency (ESA) Climate Change Initiative (CCI) global land cover data set v1.6.1 was used for identifying homogenous grid cells and stratifying results according to land cover. The data set is derived from Medium Resolution Imaging Spectrometer (MERIS) surface reflectance time series and has a spatial resolution of 300 m (Bontemps et al., 2013). The maps are available for three epochs that cover the periods 1998-2002, 2003-2007, and 2008-2012, respectively. In this study, the map for the period 2008-2012 was used as it falls within the overall data period.

GPCP

Precipitation data from the Global Precipitation Climatology Project (GPCP) are displayed as reference in the time series plot. GPCP 1DD version 1.2 provides daily precipitation estimates at 1° spatial resolution (Huffman et al., 2001). The precipitation estimates are produced from satellite data in the high frequency microwave (>10 GHz) to infrared region in combination with gauge data (Huffman et al., 2001).

ERA-Interim

Skin temperature and snow depth from ERA-Interim were used to mask VOD. ERA-Interim is the current global atmospheric reanalysis produced by the European Centre for Medium-Range Weather Forecasts for the period from 1979 onwards (Dee et al., 2011). Data are assimilated using a 4-dimensional variational analysis. The horizontal resolution is about 0.7° at the equator.

Topographic complexity

Topographic complexity was used to mask VOD during the analysis of homogeneous grid cells. It is described by the standard deviation of elevation within a grid cell. A map of topographic complexity is available as ancillary data for the ESA-CCI soil moisture v02.2 data set (Dorigo et al., 2015) with a spatial resolution of 0.25°. The topographic complexity is computed from the USGS 30-Arc-Second Global Elevation Data Set (GTOPO30) (USGS, 1996).

2.3.3 Variables for relating VOD to GPP

In this study, three variables for comparing VOD with GPP are investigated: (1) original time series of VOD, (2) change in VOD (ΔVOD), and (3) positive changes in VOD (ΔVOD$_{\geq 0}$). The latter two variables treat VOD as a proxy for aboveground biomass of the vegetation layer, which includes leaves and woody components. Liu et al. (2015) showed that the relationship between VOD and forest biomass data is monotonically increasing, which makes VOD a suitable proxy for biomass. Changes in VOD may thus relate to changes in biomass and hence to Aboveground Net Primary Production (ANPP), which contributes to total Net Primary Production (NPP).

1) Original VOD time series: For crop- and grasslands, VOD is proportional to total VWC (Jackson and Schmugge, 1991; Woodhouse, 2005) and thus scales with LAI (Zribi et al., 2011; Kim et al., 2012; Sawada et al., 2015), which in turn is related to GPP (Suyker et al., 2005; Gitelson et al., 2014). The original time series of VOD may thus be related to GPP.

2) ΔVOD: For forests, ANPP is commonly estimated through biomass changes between two consecutive measurements (Clark et al., 2001a; Campioli et al., 2011; Nunes et al., 2013; Wagner et al., 2013a; Campioli et al., 2016). Therein, biomass changes are determined from changes in stem circumference, which are converted to whole-tree biomass using allometric relations, and from litter traps or LAI. In this study, this method is adopted by calculating the change in VOD.

$$\Delta VOD(t) = VOD_t - VOD_{t-1}$$

where ΔVOD(t) is the change in VOD at time t, and VOD$_t$ and VOD$_{t-1}$ are VOD observations at time t and t-1, respectively.

3) ΔVOD$_{\geq 0}$: For grasslands, common metrics for determining annual ANPP include peak standing biomass, difference between maximum and minimum standing biomass, sum of positive biomass changes with negative values set to zero, and change in biomass (Scurlock et al., 2002). These metrics are designed for a low number of observations as the sampling of herbaceous vegetation is destructive and is often carried out once per growing season. Since the study focuses on the temporal agreement instead of annual metrics and the change in VOD is already analyzed as the second variable, the method of positive biomass changes is used as third variable.

$$\Delta VOD_{\geq 0}(t) = \begin{cases} \Delta VOD(t) & \text{if } \Delta\text{VOD(t)} \geq 0 \\ 0 & \text{otherwise} \end{cases}$$

In order to compare the results of all three variables, changes in VOD (ΔVOD and ΔVOD$_{\geq 0}$) are also compared with the FLUXCOM GPP data set although, conceptually, they should relate more closely to NPP than GPP. However, direct measurements of large-scale NPP are not possible and, therefore, NPP is often derived from remote sensing-based GPP estimates using either a constant NPP:GPP ratio at annual time scales (Waring et al., 1998) or the difference between GPP and autotrophic respiration at shorter time scales (Running et al., 2004; Zhao et al., 2005). For this reason, VOD variables in this study are related to GPP and not to NPP.

Table 2.2: CCI land cover abbreviations.

Abbreviation	CCI land cover class
CRO	Cropland, rainfed
EBF	Tree cover, broadleaved, evergreen, closed to open (>15%)
DBF	Tree cover, broadleaved, deciduous, closed to open (>15%)
ENF	Tree cover, needleleaved, evergreen, closed to open (>15%)
DNF	Tree cover, needleleaved, deciduous, closed to open (>15%)
SHR	Shrubland
GRA	Grassland
SPARSE	Sparse vegetation (tree, shrub, herbaceous cover) (<15%)

2.3.4 Data preparation

The global data sets of VOD and GPP were resampled to a common resolution of 8 days and 0.25°. Resampling was performed by averaging over the 8-day period for VOD data sets or over the grid points within each 0.25° by 0.25° grid cell for GPP. Prior to the resampling of the daily VOD data sets, the data were masked for conditions of frozen soil or snow based on ERA-Interim. Observations were excluded if the daily mean skin temperature was ≤ 0 °C or snow cover was present. For consistency with the VOD data sets, GPP and SIF were also masked accordingly. Passive microwave observations can be affected by radio frequency interference (RFI), which is caused by artificial sources of radiation and hence is not related to land surface properties (Li et al., 2004; Njoku et al., 2005). Therefore, passive VOD data were additionally masked for RFI. For ASCAT, negative values can occur due to a lower sensitivity of the modelled bare soil backscatter compared to the observed backscatter in the angular dependency (Vreugdenhil et al., 2016). These negative values were not set to zero in order to avoid introducing a bias. For the comparison with SIF observations, GPP and VOD data sets were further resampled to monthly and 0.5° resolution using temporal and spatial means, respectively.

Land cover data were converted into fractional land cover at 0.25° (or 0.5°) resolution using the level 1 legend of the CCI classification scheme. The resulting map of dominant land cover at 0.25° resolution is displayed in Figure 2.A.1. The corresponding abbreviations are summarized in Tables 2.2 and 2.A.1. For global correlation maps, grid cells with a dominant land cover class of permanent snow/ice or water were systematically excluded.

For stratifying the results according to land cover, only homogeneous grid cells were evaluated in order to minimize the influence of pixel heterogeneity. Using the ESA CCI land cover map, a grid cell was considered homogeneous if the fraction of dominant land cover within a 0.25° by 0.25° grid cell exceeded an arbitrary threshold of 75%. Additionally, grid cells were discarded if either topographic complexity or percentage of water bodies were higher than 10% following Draper et al. (2012) and Dorigo et al. (2015), since both factors have a strong impact on the emitted or reflected microwave signal (Owe et al., 2008).

Data smoothing was applied in two cases: 1) prior to calculating changes in VOD (ΔVOD and ΔVOD$_{\geq 0}$) and 2) for visualization purposes in the time series plots. The smoothing was performed using a Savitzky-Golay filter of order three with a window size of 11 observations.

2.3.5 Statistical analysis

Linear relationships were assessed using correlation analysis. Prior to the correlation analysis, the assumption of normality was tested following D'Agostino (1971) and D'Agostino and Pearson (1973). As not all grid cell data were normally distributed (p>0.05), the non-parametric Spearman rank

correlation was used instead of the parametric Pearson correlation. Due to this absence of normal distribution for some grid cell data, non-parametric measures were used when analyzing full-length time series data: the median for displaying the global distribution of the data sets and the coefficient of quartile variation (CQV, Kokoska and Zwillinger, 2000) for assessing signal variability. CQV is calculated using the 25th (Q1) and the 75th (Q3) percentile:

$$CQV = (Q3 - Q1)/(Q3 + Q1)$$

In addition to the zero-lagged correlation analysis, time lags for which the cross-correlations maximized were calculated as an additional measure to determine how well the signals match. Results for homogeneous grid cells are displayed as violin plots, which are similar to box plots but visualize the kernel estimation of the data distribution.

To compare the data sets independent of the strong seasonal signals that affect vegetation properties in many regions, anomalies relative to the mean seasonal cycle were calculated. The mean seasonal cycles were obtained from the 8-daily or monthly time series by averaging over each valid day in a year within the study period. Due to the relatively short data periods, no detrending was applied prior to calculating the mean seasonal cycles.

Residuals of the GPP-SIF relationship were analyzed to assess the potential use of VOD for estimating GPP. Residuals were calculated using a linear regression model following Guanter et al. (2014) and Damm et al. (2015). The regression models were evaluated for each grid cell separately with SIF as predictor variable. For grid cells with a significant regression ($p < 0.05$), residuals were obtained as the difference between the observed and the SIF-based estimate of GPP.

In addition to temporal correlations, spatial correlations were calculated to assess the similarity between maps. Since the spatial data were not normally distributed ($p > 0.05$), Spearman rank correlation was used.

2.4 Results

2.4.1 Global patterns of VOD, GPP and SIF

Temporal median values of VOD, GPP and SIF reveal similar spatial patterns (Figure 2.1a-g), although spatial coverage of SMOS is reduced due to RFI masking. The spatial agreement with GPP is highest for SIF ($r=0.87$), followed by the passive VOD data sets ($0.73 < r < 0.79$) and is lowest for ASCAT ($r=0.47$). In general, regions of high VOD, i.e. high biomass, coincide with highly productive regions, which are primarily located in the tropics. In addition, high values are also found at high latitudes. In these regions, data masking due to low temperature and snow results in wintertime data gaps, which in turn increases temporal median values as they represent medians over the growing season only. Nevertheless, these relatively high values of productivity or VOD at high latitudes are mainly consistent across data sets.

Considering the absolute values of the VOD data, the data range differs between the data sets, which relates on the one hand to differences in the retrieval algorithm and version number and on the other hand to differences in sensor frequency. Since the focus of this study, however, is the temporal agreement between the data sets, differences in the absolute values were not further analyzed.

Global temporal correlations between the original VOD time series and GPP at lag zero reveal positive agreement across large areas (Figure 2.2a-e). However, also some regions with negative
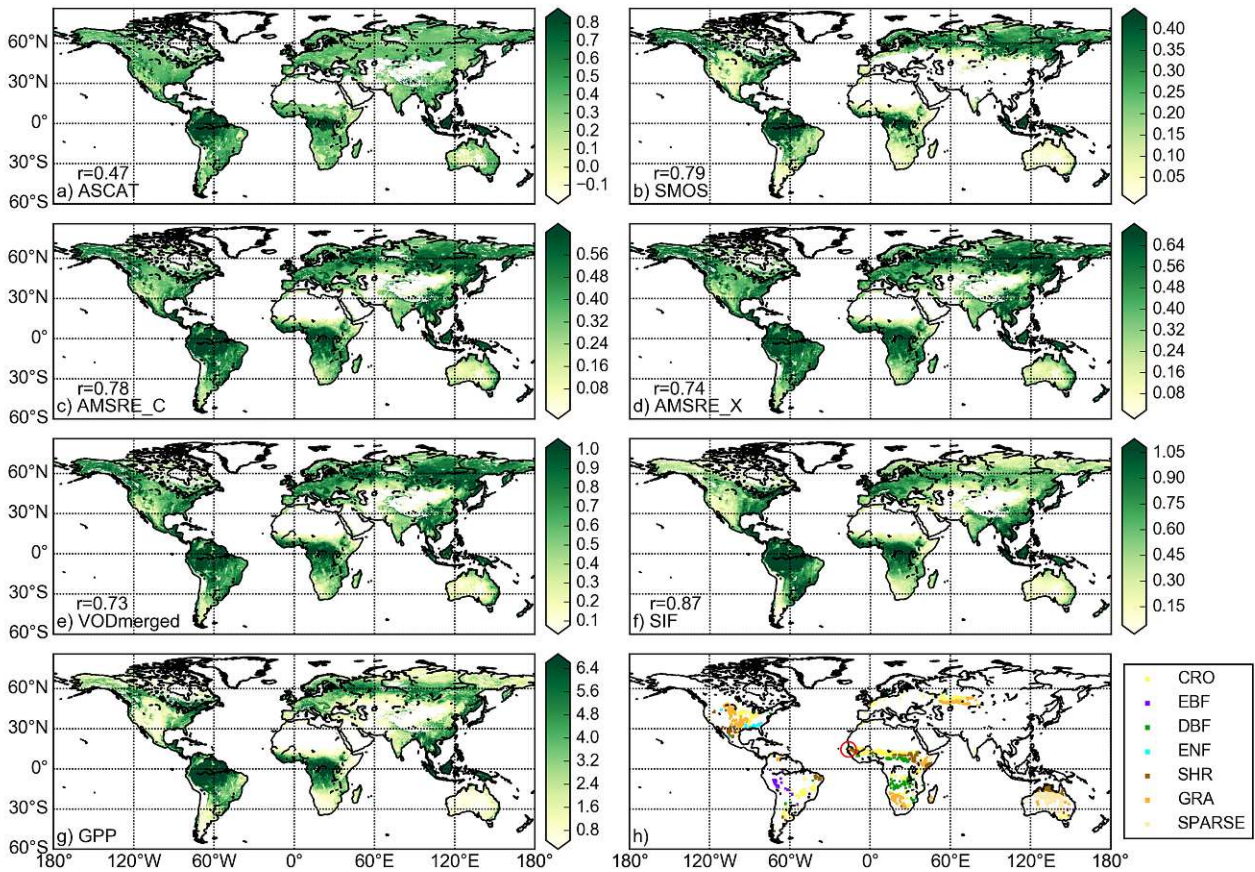
Figure 2.1: (a-g) Temporal median value of VOD data sets (a-e), SIF (f) and GPP (g). VOD is dimensionless, GPP is in $gCm^{-2}d^{-1}$ and SIF in $mWm^{-2}nm^{-1}sr^{-1}$. For visualization purposes, each data set is scaled between the 5th and the 95th percentile. (a-f) r denotes the spatial Spearman rank correlation between maps of temporal medians of GPP and VOD or SIF. All coefficients are highly significant (p<0.001). (h) Map of CCI land cover grid cells with a dominant land cover over 75% that correspond to the analyzed grid cells in Figure 2.4. The center of the red circle marks the location of the grid cell shown in Figure 2.8. Note that the size of the grid cells is enhanced for clearer visibility.

correlations are observed. For ASCAT, negative correlations are found in Central America, South America, Africa and Southeast Asia. The passive VOD data sets show negative correlations mainly in South America (in particular in the Amazon) and Southeast Asia. Although the results for different passive VOD data sets are similar in most areas, deviations from this behavior are found for SMOS and the merged VOD. For SMOS, negative correlations in central Africa coincide with those for ASCAT. For the merged VOD, predominantly positive correlations with GPP are observed in the Amazon, which contrasts with the negative values found for the other passive VOD data sets and may be related to differences in the algorithm version. Compared to the VOD data sets, the correlation between GPP and SIF (Figure 2.2f) is positive everywhere and on average much stronger. Nevertheless, also regions with no significant correlations (p>0.05) occur, which are mainly located in the tropics and in Australia. In the tropics, both GPP and SIF exhibit low variability, while the opposite, i.e. high variability for both data sets, is found in Australia (Figure 2.A.2).

Correlations between the anomalies of VOD and GPP (Figure 2.3a-e) also exhibit predominantly positive correlations. On average, the correlations are lower in magnitude than for the original time series but also show a lower number of negative values. Regions with relatively high correlations for the anomalies coincide with regions of high temporal agreement for the original time series, while some regions with negative correlations for the original time series result in no significant correlations
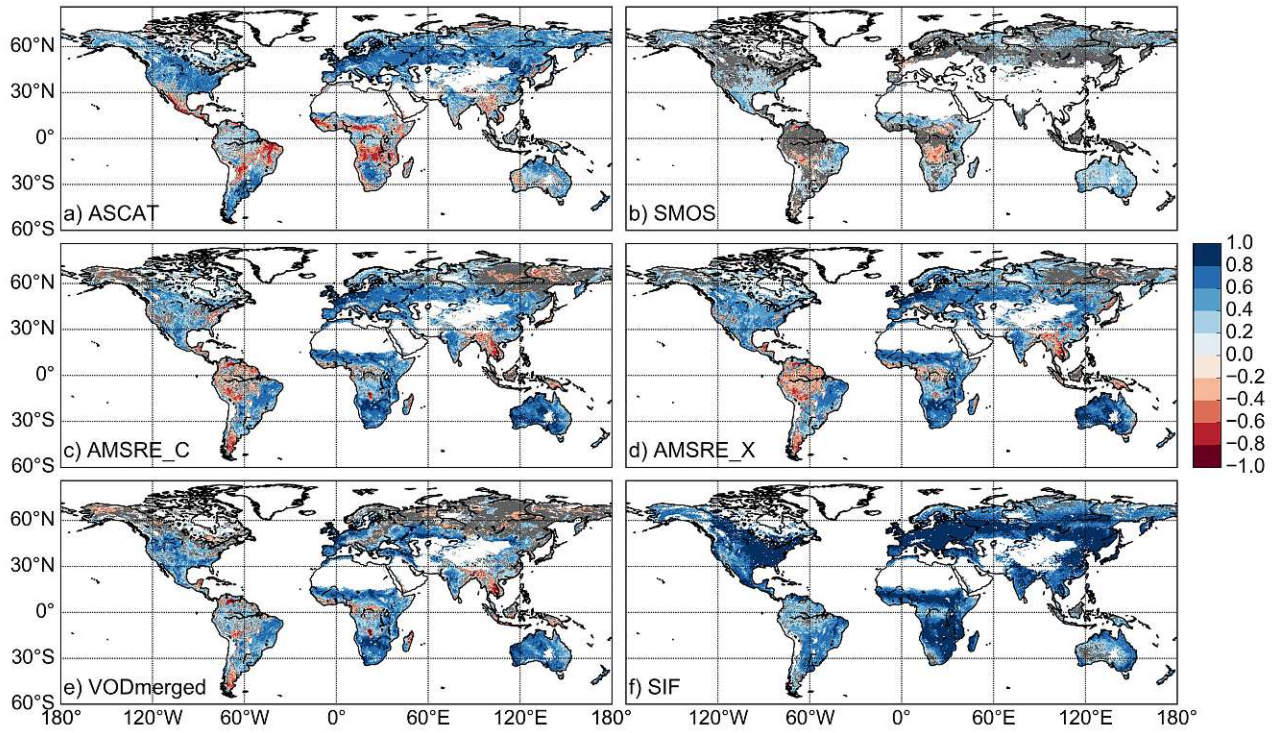
Figure 2.2: (a-e) Spearman rank correlation between GPP and VOD data sets at 0.25° and 8-daily resolution. Correlations that are not significant (p>0.05) are masked in grey. Corresponding correlations at 0.5° and monthly resolution are displayed in Figure 2.A.4. (f) Spearman rank correlation between GPP and SIF at 0.5° and monthly resolution.
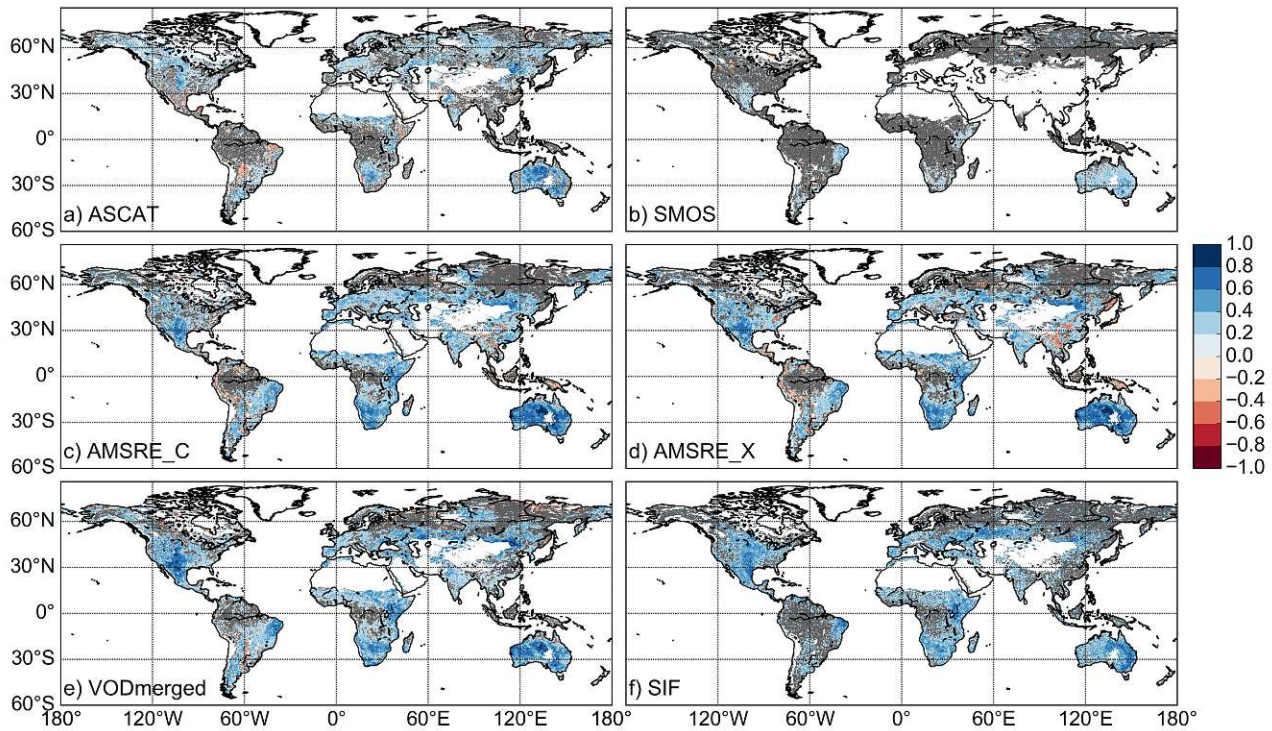
Figure 2.3: As Figure 2.2 but for the anomalies from the mean seasonal cycle. For a-e, the corresponding correlations at 0.5° and monthly resolution are shown in Figure 2.A.5.

for the anomalies. Highest correlation coefficients are observed in Australia. The correlations for the anomalies of GPP and SIF (Figure 2.3f) are of similar strength as the correlations between the anomalies of GPP and VOD.
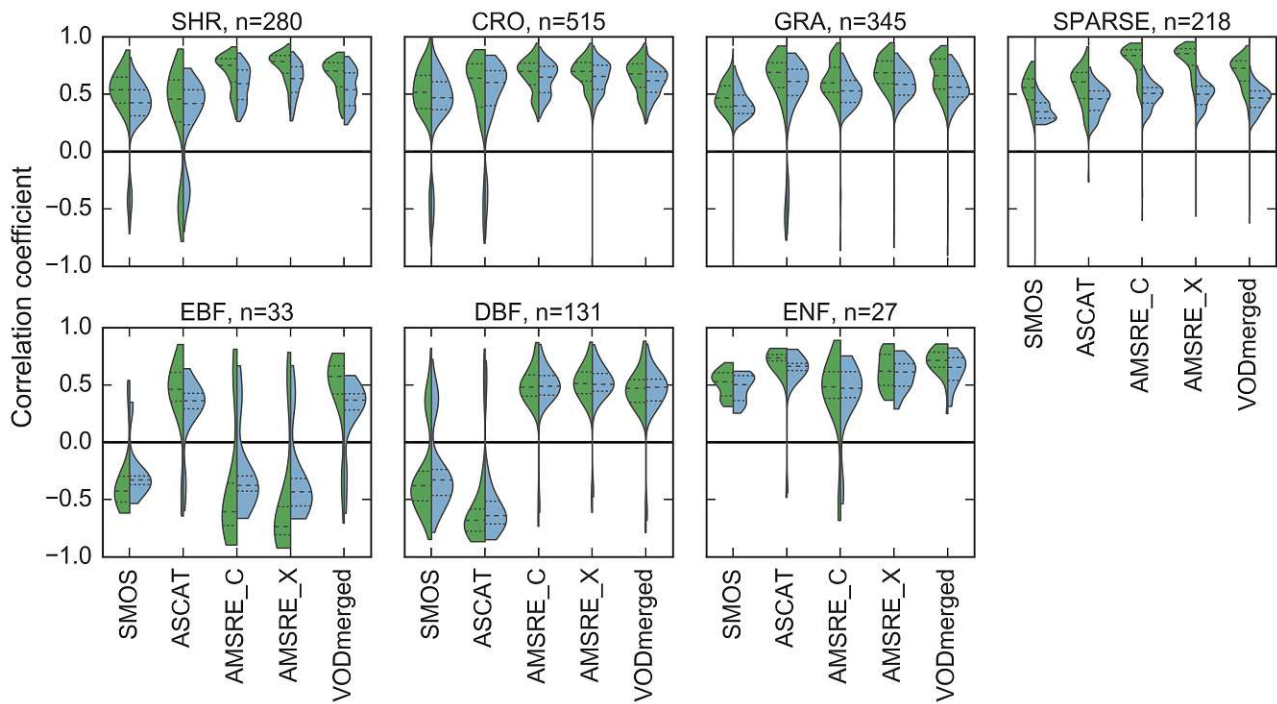
Figure 2.4: Violin plots of Spearman rank correlation between VOD and GPP (green) and between VOD and SIF (blue) at 0.5° and monthly resolution for grid cells with a dominant land cover fraction above 75%. Results are grouped according to the CCI land cover classification and single frequency data sets are ordered along increasing microwave frequency. The number of grid cells (n) is displayed above each graph. Horizontal lines within the violins indicate quartiles. Values that are not significant ($p > 0.05$) are excluded. For the description of the land cover abbreviations see Table 2.2, for the spatial distribution of grid cells see Figure 2.1h. Note that DNF is not displayed since the analysis did not result in significant correlations for this land cover type.

2.4.2   Temporal agreement with respect to SIF

The direct comparison of correlations between VOD and either GPP or SIF at homogeneous grid points (Figure 2.4) shows that the temporal agreement between VOD and SIF is similar to that found between VOD and GPP. In most cases, however, the median correlation coefficient is lower for the correlation between VOD and SIF than between VOD and GPP. This is especially pronounced for sparsely vegetated grid cells, which are mostly located in Australia (see Figure 2.1h).

In order to assess if VOD can provide additional information about GPP on top of that provided by SIF, VOD was correlated with the residuals of the GPP-SIF relationship (Figure 2.5). The spatial maps reveal mainly positive correlations with negative correlations in the same areas as for the original time series but show a larger number of not significant correlations. In those areas where correlations are significant, VOD can explain variations in GPP that are not expressed through SIF using linear regression.

2.4.3   Comparison of the three variables for relating VOD to GPP

For the comparison of the three variables with GPP, only grid cells that resulted in significant correlations for all three variables are shown in Figure 2.6. For shrub-, crop-, grassland and sparse vegetation, all three variables yielded consistent, mainly positive correlations. Median values are generally lowest for the correlation between SMOS and GPP and appear to increase with sensor frequency. In most cases, the original VOD time series result in higher median correlations with GPP than the changes
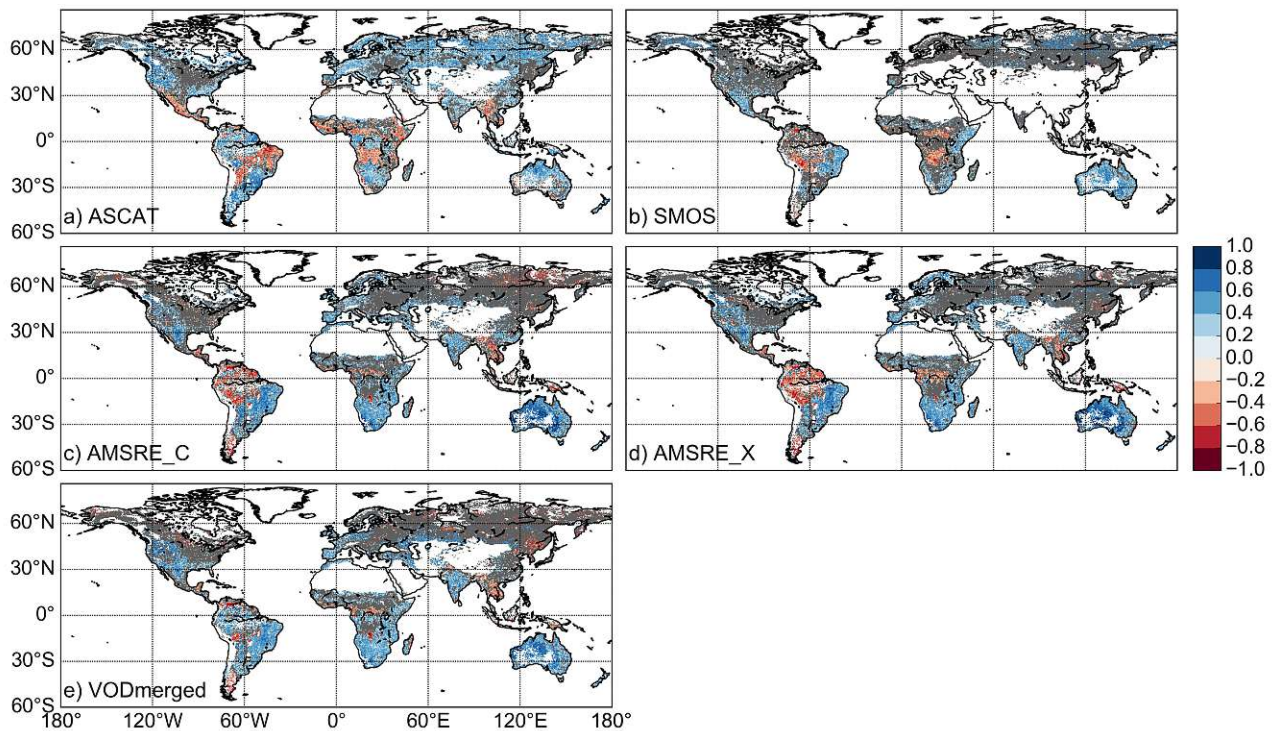
Figure 2.5: As Figure 2.2a-e but for the correlation between VOD and the residuals of the GPP-SIF relationship at 0.5° and monthly resolution.

in VOD. Highest median correlations are observed for shrubland for both frequencies of AMSR-E. Comparing the changes in VOD, results show that $\Delta VOD_{\geq 0}$ generally leads to higher correlations than ΔVOD.

For forests, results are not as consistent as for the sparsely to moderately vegetated areas. Nevertheless, forests also show on average a lower magnitude of correlation between SMOS and GPP than for the remaining VOD data sets. Similar as for the sparsely to moderately vegetated areas, evergreen needleleaf forests exhibit generally higher correlations for the original VOD time series than for ΔVOD and $\Delta VOD_{\geq 0}$. In contrast, deciduous forests mainly yield higher median correlations for ΔVOD and $\Delta VOD_{\geq 0}$ than for the original VOD time series. Evergreen broadleaf forests, which exhibit low signal variability (see Figure 2.A.2) and a high number of negative correlations, do not show a consistent pattern for the three variables. Comparing only the changes in VOD for all forests, median correlations tend to be higher for ΔVOD than for $\Delta VOD_{\geq 0}$ and thus show the opposite behavior as for the sparsely to moderately vegetated areas.

The spatial distributions of the correlations between GPP and the three VOD variables (Figures 2.2, 2.A.6 and 2.A.7) tend to complement each other. For grid points where the original VOD time series results in high correlations, ΔVOD and $\Delta VOD_{\geq 0}$ have lower correlations and vice versa. Since ΔVOD and $\Delta VOD_{\geq 0}$ both represent changes in VOD, their spatial correlation patterns with GPP are more similar compared to the correlation pattern between original VOD time series and GPP (Table 2.A.2).

The lag analysis (Figure 2.7) is based on the same grid cells as in Figure 2.6. On average, the original VOD time series follow the GPP signal: changes in GPP are reflected with some delay by subsequent changes of the VOD signal. Apart from the broadleaf forests, all land cover classes exhibit median lag values ranging between 0 and 50 days. For ASCAT in deciduous broadleaf forest, the half a year's lag corresponds to the strong negative correlations found before for the zero-lagged correlations
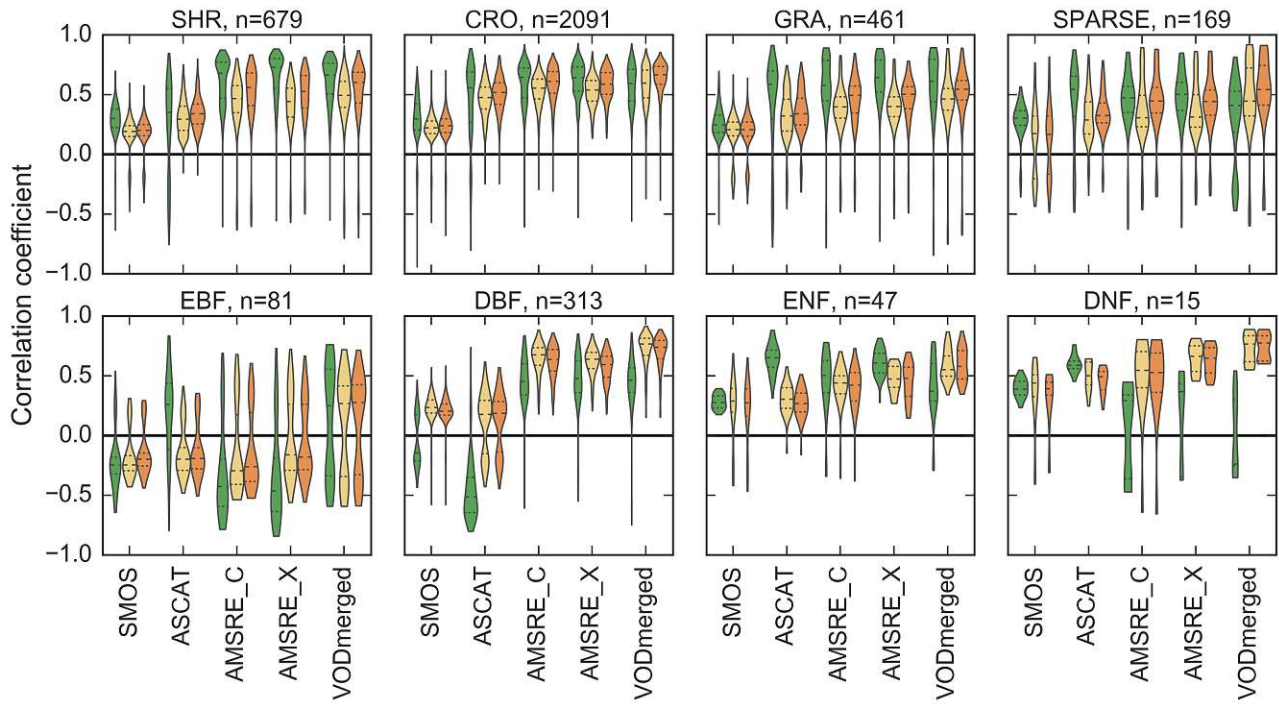
Figure 2.6: Violin plots of Spearman rank correlation between GPP and VOD (green), ΔVOD (yellow) or ΔVOD$_{\geq 0}$ (orange) at 0.25° and 8-daily resolution. Results are displayed for grid cells with a dominant land cover fraction above 75% and grouped according to land cover (Table 2.2). n is the number of grid cells. Horizontal lines within the violins indicate quartiles. Values that are not significant (p>0.05) are excluded. See Figure 2.A.3 for the spatial map of the analyzed grid cells.

(Figure 2.6). In contrast to the positive lag found for the original VOD time series, the lag values for ΔVOD and ΔVOD$_{\geq 0}$ are negative, which indicates that changes in VOD generally precede the GPP signal. In some cases, as for example in the deciduous broadleaf forest for AMSRE_C, AMSRE_X and the merged VOD, the absolute value of the median lag is smaller for ΔVOD and ΔVOD$_{\geq 0}$ than for the original VOD time series. In these cases, calculating the change in VOD leads to a closer temporal agreement with GPP, which corresponds to the higher correlation coefficients found for the zero-lagged correlations.

This shift from positive to negative lag values for the different variables is further illustrated in Figure 2.8 for a rainfed cropland-dominated grid cell. Comparing the data close to the seasonal peaks, the original VOD time series decrease slower than the GPP signal, resulting in a positive lag (Figure 2.8b). For ΔVOD, the signal rises earlier than for GPP, which yields a negative lag (Figure 2.8c). Apart from the opposite sign of the lag value, the scaled ΔVOD signal shows a different shape than the GPP signal. ΔVOD exhibits a high number of values around 0.5, which represent ΔVOD values close to zero and are a result of the relatively long period of small changes in VOD. In this case, considering only positive changes in VOD appears to result in a higher temporal matching with GPP (Figure 2.8d), which explains the higher correlations found for ΔVOD$_{\geq 0}$ compared to ΔVOD in sparsely to moderately vegetated areas (Figure 2.6). Despite the overall higher temporal agreement for ΔVOD$_{\geq 0}$ than for ΔVOD, the decline in GPP is better captured by ΔVOD.

The relationships between the three VOD variables and GPP can be further assessed with the corresponding scatter plots (Figures 2.8e-g). This relationship describes a seasonal hysteresis. Comparing all three variables, the shape of the mean seasonal cycle appears to be similar for the original VOD time series and ΔVOD as they both exhibit a pronounced linear part, while this feature is missing for
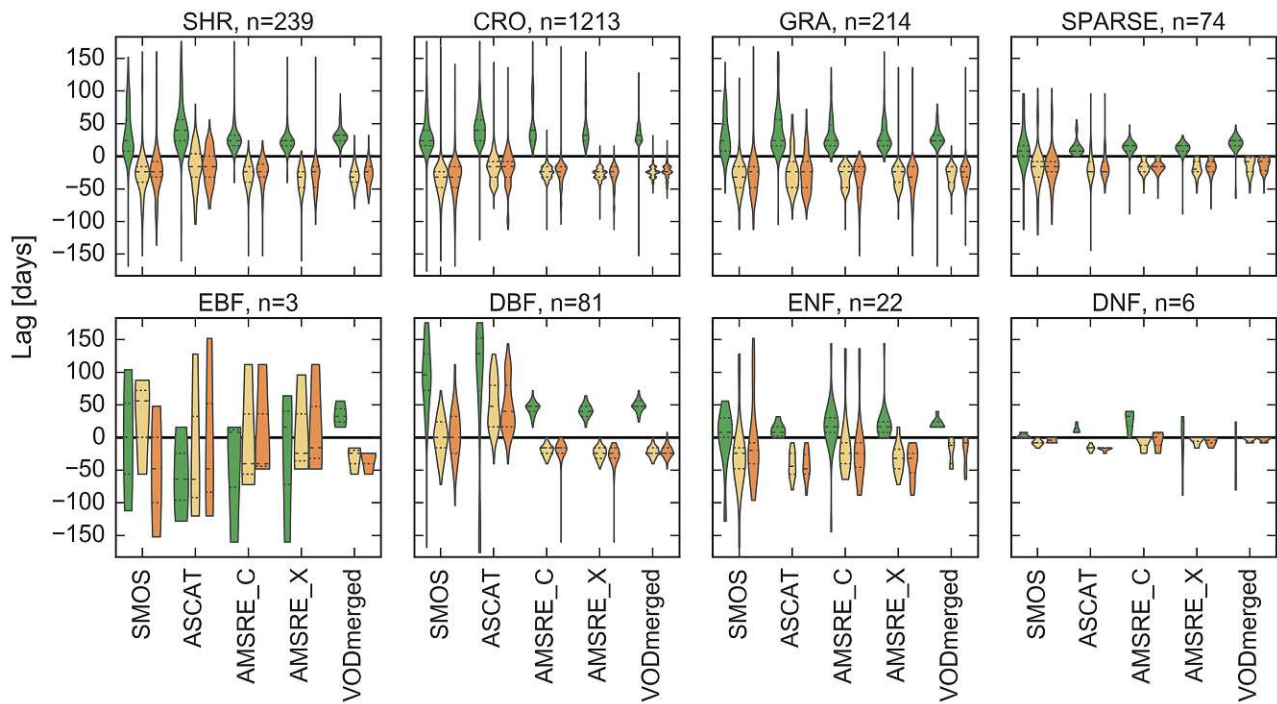
Figure 2.7: As Figure 2.6 but for the lag. Lag values are excluded if the lag is larger than half a year or the correlation of the lagged time series is not significant (p>0.05).

$\Delta VOD_{\geq 0}$. The linear part for the original VOD, however, corresponds to the GPP increase, while for ΔVOD the linear part relates to the GPP decrease.

2.5 Discussion

2.5.1 Temporal agreement between VOD, GPP and SIF

In this study, large parts of the world reveal positive correlations between VOD and GPP both for the original time series and for the anomalies from the mean seasonal cycle. In addition, correlations between VOD and the residuals of the linear GPP-SIF relationship demonstrate that VOD can explain variations in GPP that are not explained by SIF. These findings suggests that VOD provides useful information with regard to GPP.

Water limitation appears to foster the coupling between VOD and GPP as areas with particularly high correlations between VOD and GPP in this study seem to coincide with areas of low water availability (Miralles et al., 2016; Papagiannopoulou et al., 2017). In these areas, vegetation responds more rapidly to changes in water availability (De Keersmaecker et al., 2015), which in turn is reflected in a close association between VOD and GPP.

The most prominent example of low correlations in this study is found for evergreen broadleaf forests, which can be attributed to the low signal variability found in the tropics. This is in line with the generally low predictability of GPP in tropical forests (Tramontana et al., 2016) and can be linked to isohydricity, which describes the plant strategy of stomatal control in response to water stress (Konings and Gentine, 2017). Evergreen broadleaf forests are very isohydric, i.e. they try to minimize changes in leaf water potential by closing stomata (Fisher et al., 2006; Konings and Gentine, 2017). This closing of stomata may result in a decoupling of VWC and photosynthetic activity and hence cause a weaker relationship between VOD and GPP.
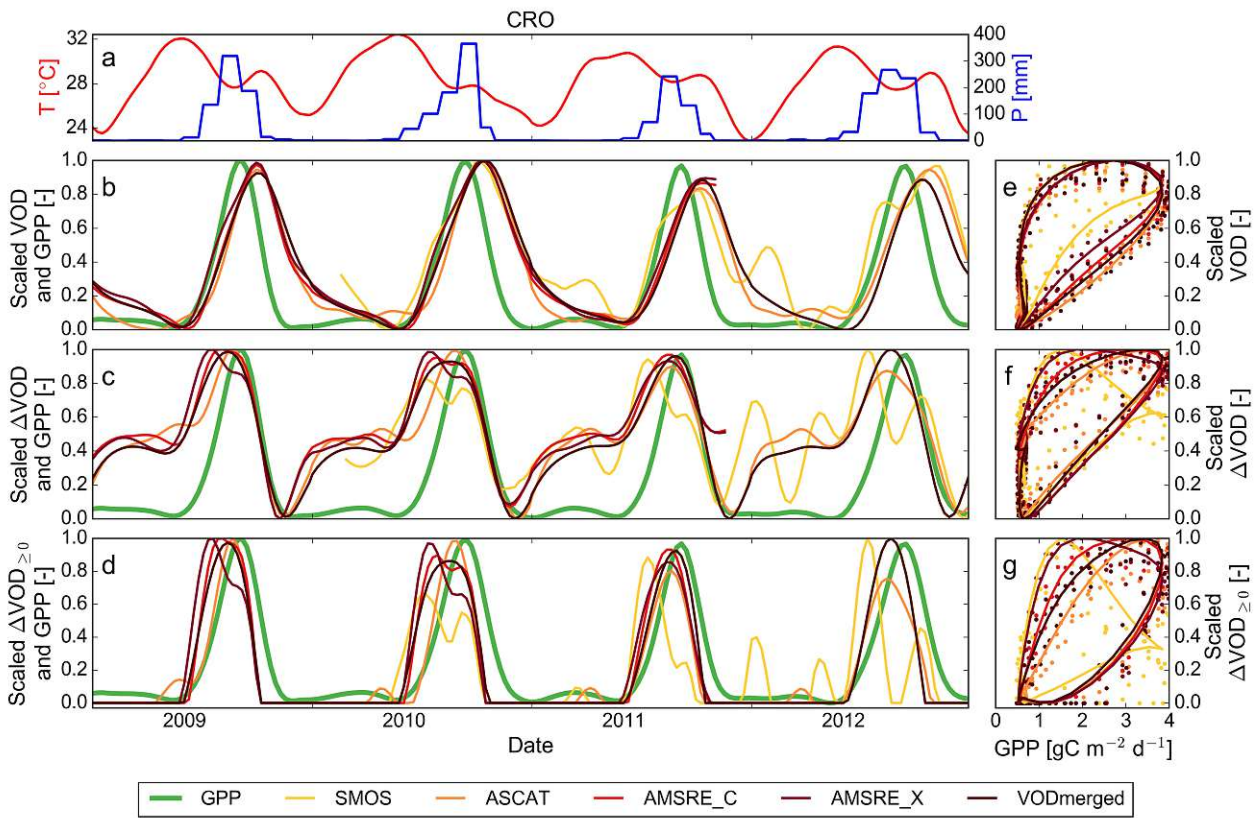
Figure 2.8: Time series (a-d) and scatter plots (e-g) at 8-daily resolution for a cropland-dominated grid cell in West Sahel, located at 16.125W 14.625N, for the period 2009-2012 (location is indicated in Figure 2.1f). (a) Skin temperature (T) and monthly sums of precipitation (P). (b-d) VOD (b), ΔVOD (c), or $\Delta VOD_{\geq 0}$ (d) together with GPP. Data are smoothed and scaled between their minimum and maximum for visualization purposes. Note that the unscaled ΔVOD includes negative values. (e-g) Scatter plots of scaled VOD variables against unscaled GPP for the same data as in (b-d).

2.5.2   Occurrence of negative correlations between VOD and GPP

Negative correlations between VOD and GPP can be attributed to land surface properties and vegetation phenology. For ASCAT, negative correlations can be explained with the contribution of dry soil to volume scattering (Vreugdenhil et al., 2016), which is often found for ASCAT backscatter in arid and semi-arid regions (Wagner et al., 2013b; De Jeu et al., 2008). Liu et al. (2016) showed for L-band backscatter that the scattering mechanism of the soil shifts from surface scattering under wet conditions to volume scattering under very dry conditions; below a certain soil moisture threshold, the backscatter increases again with decreasing soil moisture. Some grid cells showing negative correlations are found in the tropical dry forest biome, which regularly experience a pronounced dry season lasting up to six months (Olivares and Medina, 1992). Therefore, depending on the duration and severity of the seasonal dry period and on the soil properties, volume scattering of dry soil might lead to spurious signals in the VOD if soil volume scattering is not taken into account in the retrieval algorithm, as is the case for the ASCAT TU-Wien algorithm (Hahn et al., 2017).

In contrast to the active VOD, most negative correlations for passive VOD data can be linked to wetlands (Jones et al., 2011; Liu et al., 2011; Vreugdenhil et al., 2017). Jones et al. (2011) demonstrated that passive VOD data exhibit an inverse relationship with vegetation growth for areas that are seasonally inundated.

For evergreen broadleaf forest, negative correlations with GPP for SMOS, AMSRE_C, and AM-

SRE_X may partly relate to leaf phenology. Jones et al. (2014) reported asynchronous behavior between flux tower GPP estimates and AMSR-E C-band VOD for the Amazon forest, which may be linked to an inverse relationship between leaf age and photosynthetic capacity. New leaves, which flush during the dry season (Wright and Van Schaik, 1994; Huete et al., 2006), are photosynthetically more active than old leaves (Kitajima et al., 2002; Hutyra et al., 2007) but may also cause overall lower values of VOD.

Similarly, negative correlations found for SMOS in Africa may relate to the phenology in tropical dry forests. Early studies demonstrated that deciduous trees in dry forests minimize their water loss by leaf shedding, and that some trees also flower during the dry season or often leaf out at the end of the dry season (Olivares and Medina, 1992; Borchert, 1994a,b). In terms of the VOD signal, this means that trunks and branches still contain a relatively high amount of water during the dry season. Since L-band data is most sensitive to larger structures (Woodhouse, 2005), this asynchronous behavior of the stem water content may lead to the observed negative correlations between SMOS and GPP.

2.5.3 Effect of sensor frequency

The comparison of different sensor frequencies between 1 and 10 GHz (L-, C-, and X-band) showed that for sparsely to moderately vegetated areas median correlations increased with sensor frequency. In line with this result, Calvet et al. (2011) demonstrated for a dense wheat field that C- and X-band microwave observations obtained from a ground-based radiometer are more sensitive to VWC than L-band data. Since VWC is linearly related to VOD (Jackson and Schmugge, 1991; Woodhouse, 2005), this can explain the lower magnitude of the correlation coefficients between SMOS and GPP compared to the remaining VOD data sets. For forested regions, a similar behavior, with a low magnitude of the correlation for SMOS, was observed in this study. This suggests that C- and X-band microwave observations are better suited for relating VOD to GPP than L-band data.

2.5.4 Comparison of the three VOD variables in relation to GPP

Detailed knowledge about land cover is of decisive importance when assessing VOD in relation to GPP. Large differences exist for the three VOD variables between forested and non-forested regions. While ΔVOD shows a higher temporal agreement with GPP over forests, the original VOD time series yield higher correlations with GPP for sparsely to moderately vegetated areas.

According to the lag analysis, all three VOD variables generally did not yield a zero lag. The opposite signs for VOD compared to ΔVOD and ΔVOD$_{\geq 0}$ suggest that at the global scale neither the original VOD time series nor the changes in VOD alone can be used for relating VOD to GPP, but instead should be combined. The reason why both VOD and ΔVOD (or ΔVOD$_{\geq 0}$) are linked to GPP, i.e. the sum of NPP and autotrophic respiration, can be explained with the contribution of both biomass and growth-related terms to GPP.

NPP relates to the sum of above- and belowground NPP as well as losses through volatile organic compounds (VOC), herbivory and root exudates (Clark et al., 2001a,b; Gower et al., 2001; Girardin et al., 2010). Assuming that belowground NPP is a fraction of ANPP (Clark et al., 2001a), these two terms relate to changes in biomass and, hence, to ΔVOD. The magnitude of the VOC flux was estimated to be small compared to NPP or GPP (Guenther et al., 1995; Kesselmeier et al., 2002), and losses through herbivory between consecutive observations and root exudates are difficult to quantify.

Autotrophic respiration can be expressed as the sum of maintenance and growth respiration; while

maintenance respiration is proportional to living biomass, growth respiration is a function of the change in biomass (Ryan, 1990; Lavigne et al., 1996). Hence, VOD and ΔVOD can be related to maintenance and growth respiration, respectively. This suggests that GPP may be expressed as a combination of VOD and ΔVOD.

The relationship between VOD, ΔVOD or ΔVOD$_{\geq 0}$ and GPP may also vary throughout the season leading to hysteresis as shown in this study for a cropland-dominated grid cell. Similarly, but for the relationship between LAI and GPP, Gitelson et al. (2014) emphasized the importance of seasonal hysteresis. In the current study, the hysteresis was also present for ΔVOD, which indicates that this behavior is not merely a result of using a state (VOD) rather than a flux variable (ΔVOD). The presence of a seasonal hysteresis also explains here the on average lower correlations found for GPP vs VOD compared to GPP vs SIF, since such a hysteresis decreases the strength of the linear relationship. Combining the original VOD time series and the change in VOD thus might reduce the strength of the seasonal hysteresis and thereby improve the temporal agreement with GPP.

2.6   Conclusions

The global analysis of VOD from different frequencies (L-, C- and X-band) in relation to GPP indicates that microwave VOD, which provides complementary information to optical data, has the potential to serve as explanatory variable for estimating GPP. Although some negative correlations occurred in dry and wet areas for active and passive VOD, respectively, VOD and changes in VOD (ΔVOD or ΔVOD$_{\geq 0}$) generally demonstrated a high temporal agreement with GPP, especially for C- and X-band data. The mainly non-overlapping distributions of negative correlations for active and passive observations indicate that active and passive VOD data should be used jointly. Land cover based differences in lag and correlation coefficient further suggest to combine original VOD time series with changes in VOD for relating VOD to GPP. In addition, seasonal hysteresis was observed for the relationship between VOD variables and GPP, which demonstrates that this relationship may vary both in space and in time. This underpins the need to further investigate the spatio-temporal relationship between VOD and GPP in order to make full use of microwave satellite vegetation data for regional to global ecosystem analyses and vegetation monitoring.

2.7   Acknowledgements

Appendix

2.A Supplement

Table 2.A.1: CCI land cover abbreviations for classes that are shown in Figure 2.A.1 in addition to the classes presented in Table 2.2. These classes are excluded from the analysis.

Abbreviation	CCI land cover class
CRO_irr	Cropland, irrigated or post-flooding
MOSAIC_cro	Mosaic cropland (>50%) / natural vegetation (tree, shrub, herbaceous cover) (<50%)
MOSAIC_nat	Mosaic natural vegetation (tree, shrub, herbaceous cover) (>50%) / cropland (<50%)
MF	Tree cover, mixed leaf type (broadleaved and needleleaved)
MOSAIC_tree_shrub	Mosaic tree and shrub (>50%) / herbaceous cover (<50%)
MOSAIC_herb	Mosaic herbaceous cover (>50%) / tree and shrub(<50%)
LM	Lichens and mosses

Table 2.A.2: Spatial similarity between maps of temporal correlations for Figure 2.2 (GPP-VOD), Figure 2.A.6 (GPP-ΔVOD) and Figure 2.A.7 (GPP-ΔVOD$_{\geq 0}$). Spatial similarity was determined using Spearman rank correlation. All coefficients are highly significant (p<0.001).

	SMOS	ASCAT	AMSRE_C	AMSRE_X	VODmerged
(GPP-VOD) vs (GPP-ΔVOD)	0.22	0.20	0.05	0.03	-0.27
(GPP-VOD) vs (GPP-ΔVOD$_{\geq 0}$)	0.25	0.21	0.09	0.08	-0.23
(GPP-ΔVOD) vs (GPP-ΔVOD$_{\geq 0}$)	0.96	0.93	0.93	0.91	0.96
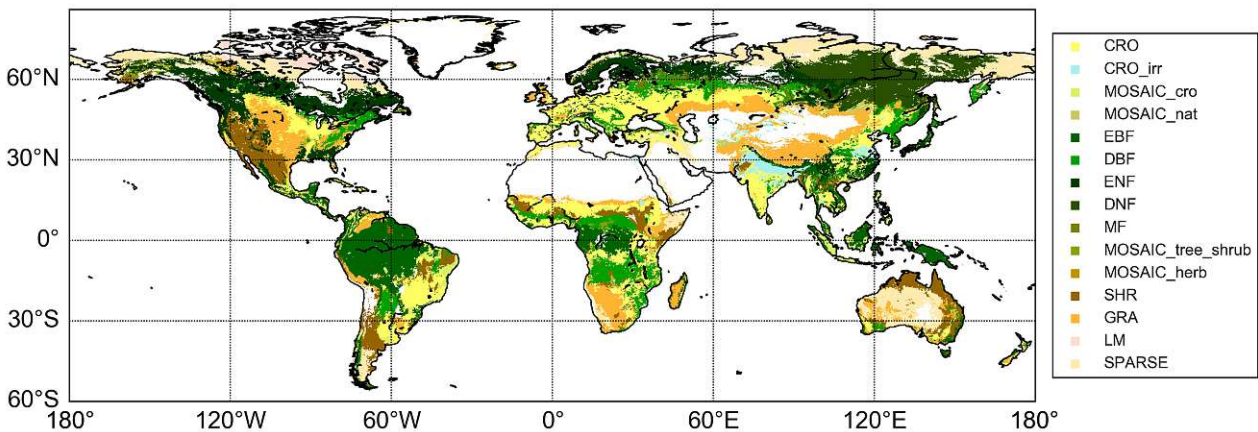
Figure 2.A.1: Map of CCI land cover. For the land cover abbreviations see Tables 2.2 and 2.A.1. Note that the color code is different from that in Figures 2.1h and 2.A.3.
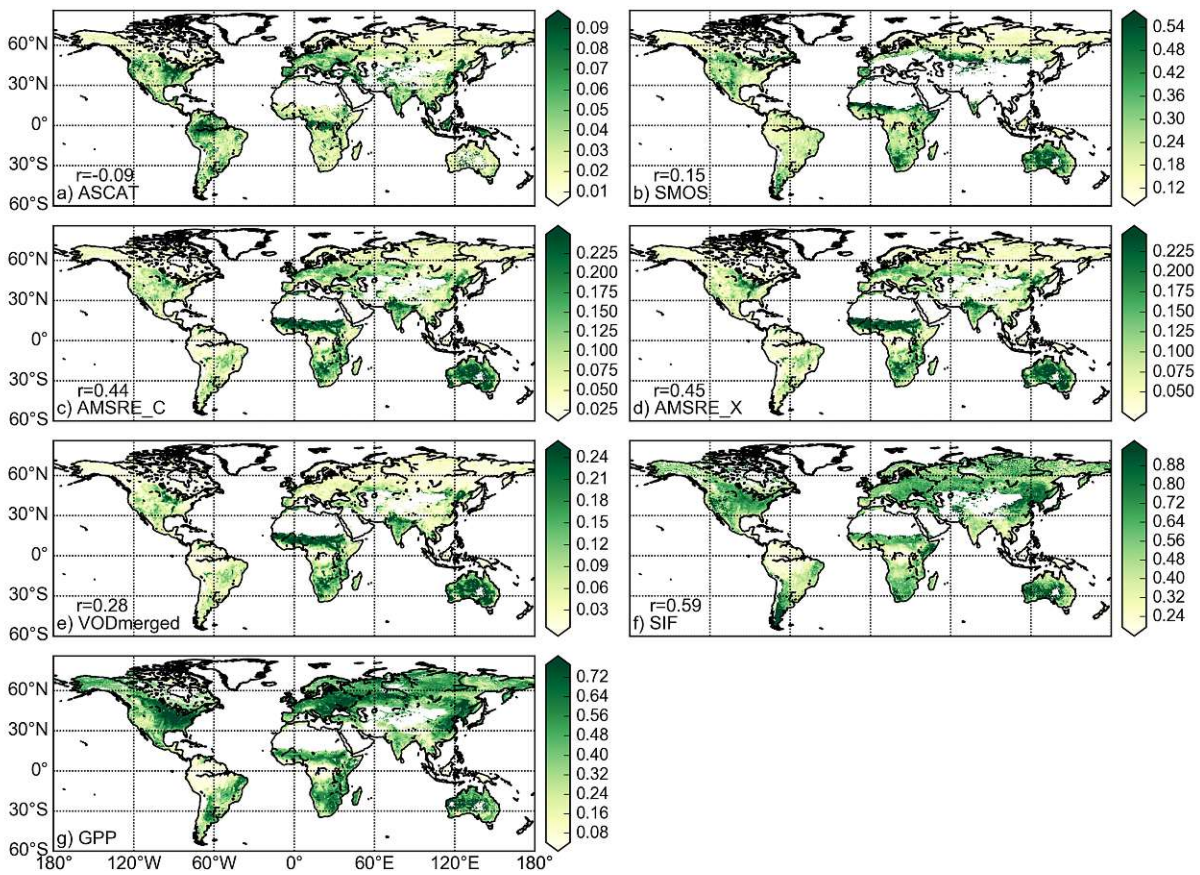
Figure 2.A.2: (a-g) Coefficient of quartile variation for VOD data sets (a-e), SIF (f) and GPP (g). Data are scaled between the 5th and the 95th percentile. (a-f) r indicates the spatial Spearman rank correlation between maps of GPP and VOD or SIF. All coefficients are highly significant (p<0.001).
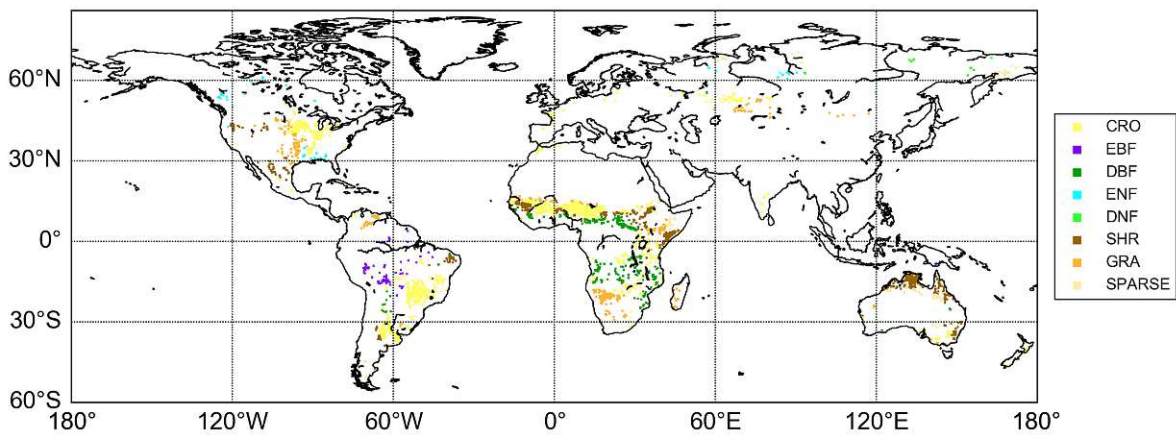
Figure 2.A.3: Map of CCI land cover for grid cells with a dominant land cover over 75% that are shown in Figure 2.6. Note that grid cells are enhanced for visualization purposes.
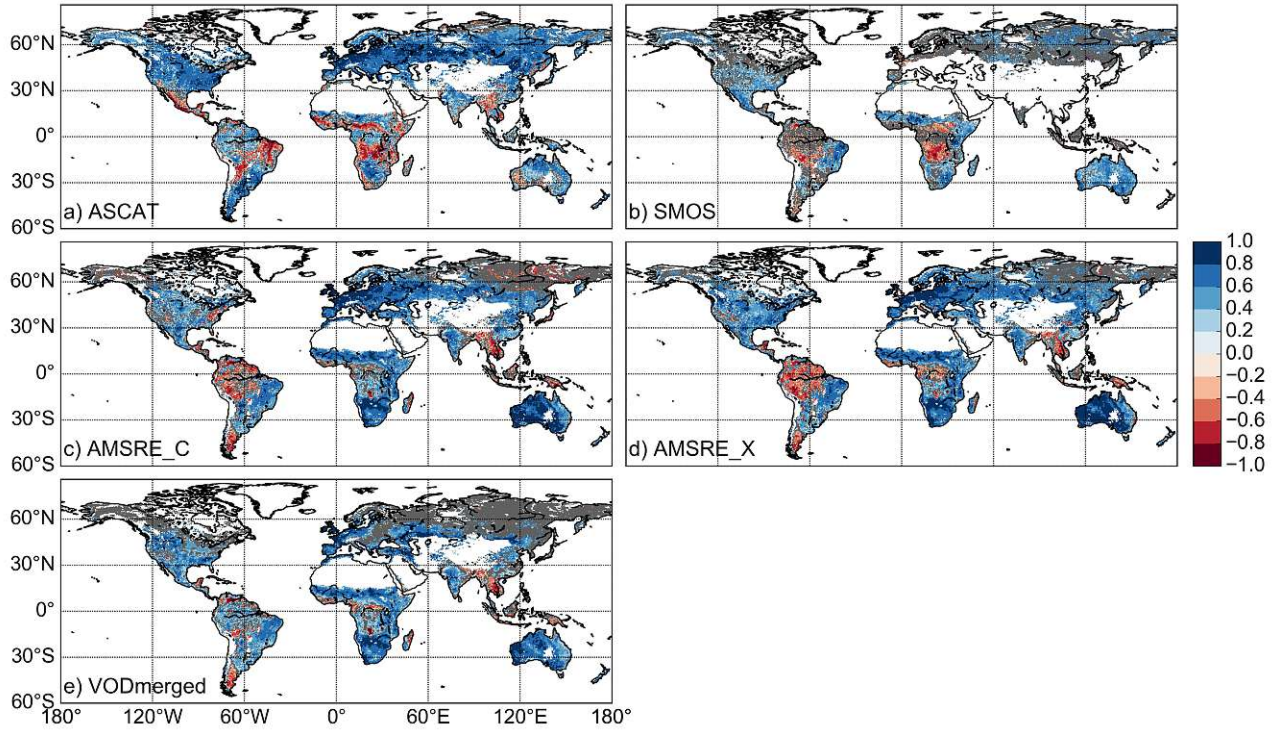
Figure 2.A.4: (a-e) Spearman rank correlation between GPP and VOD data sets at 0.5° and monthly resolution. Not significant correlations (p>0.05) are masked in grey.
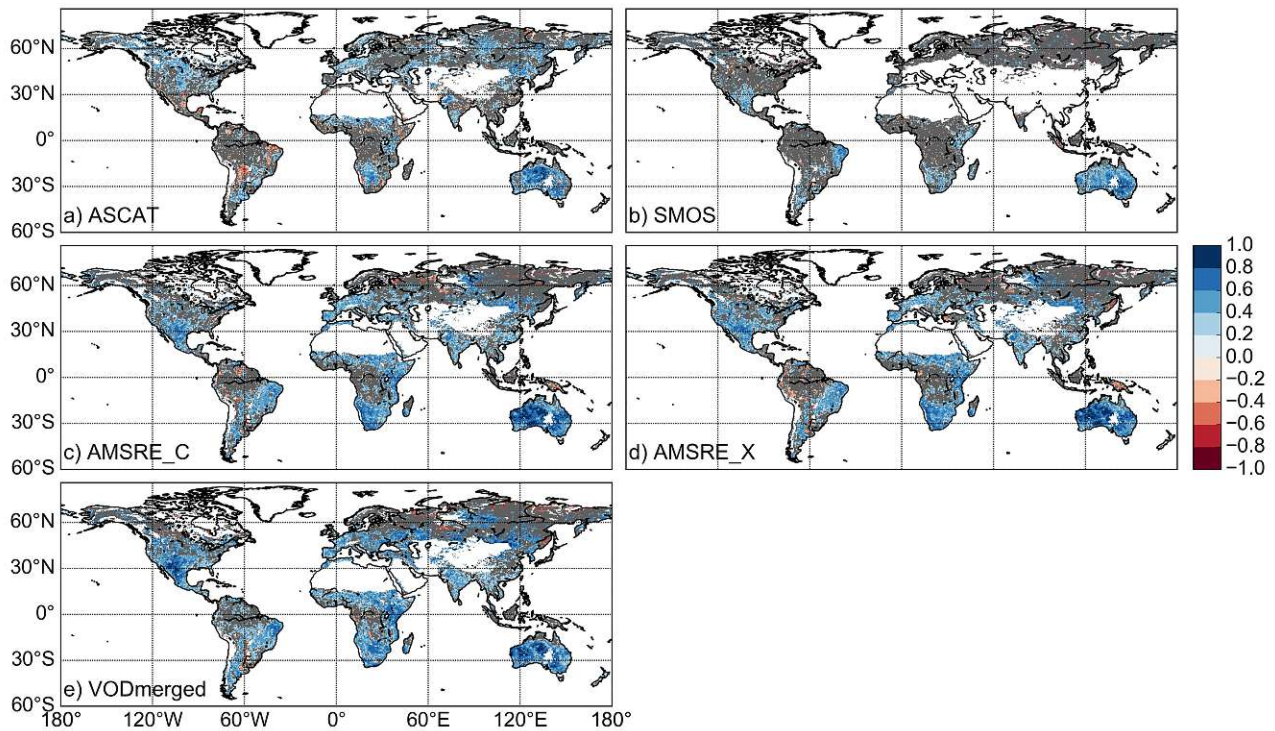
Figure 2.A.5: As Figure 2.A.4 but for the correlation between the anomalies of GPP and VOD data sets.

27
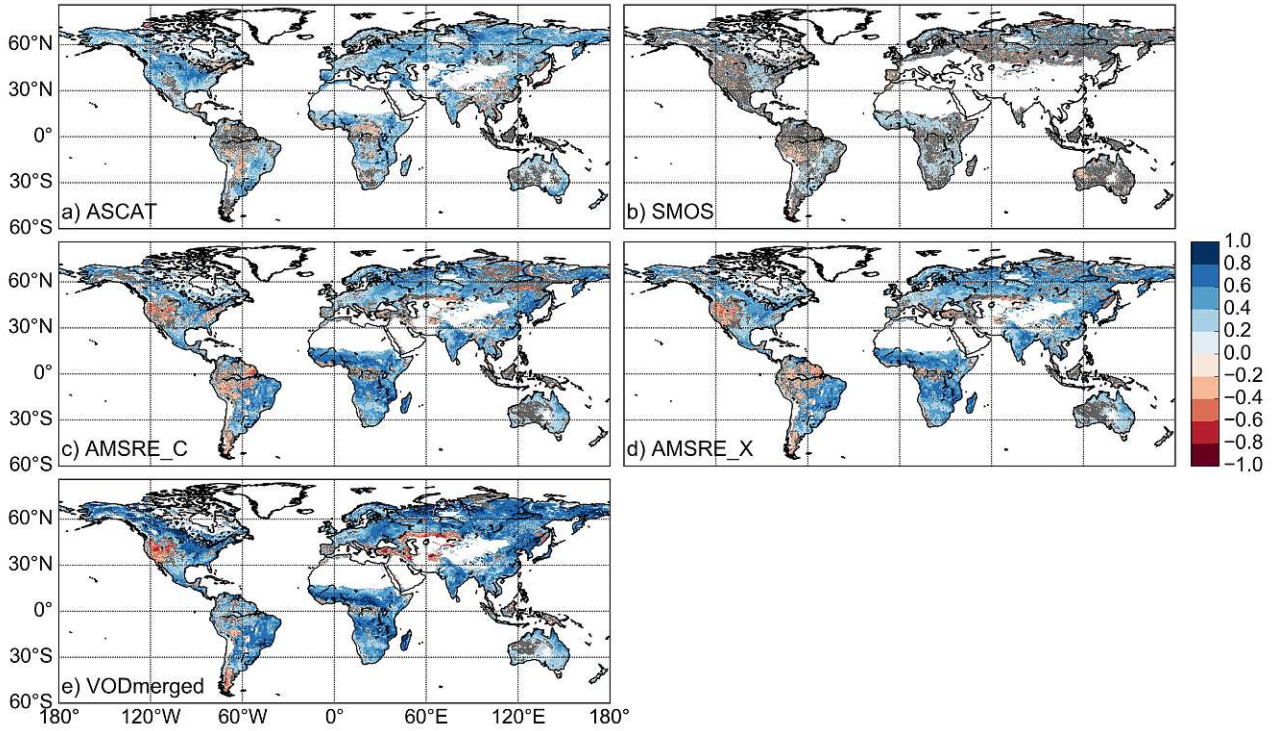
Figure 2.A.6: (a-e) Spearman rank correlation between GPP and ΔVOD data sets at 0.25° and 8-daily resolution. Not significant correlations (p>0.05) are masked in grey.
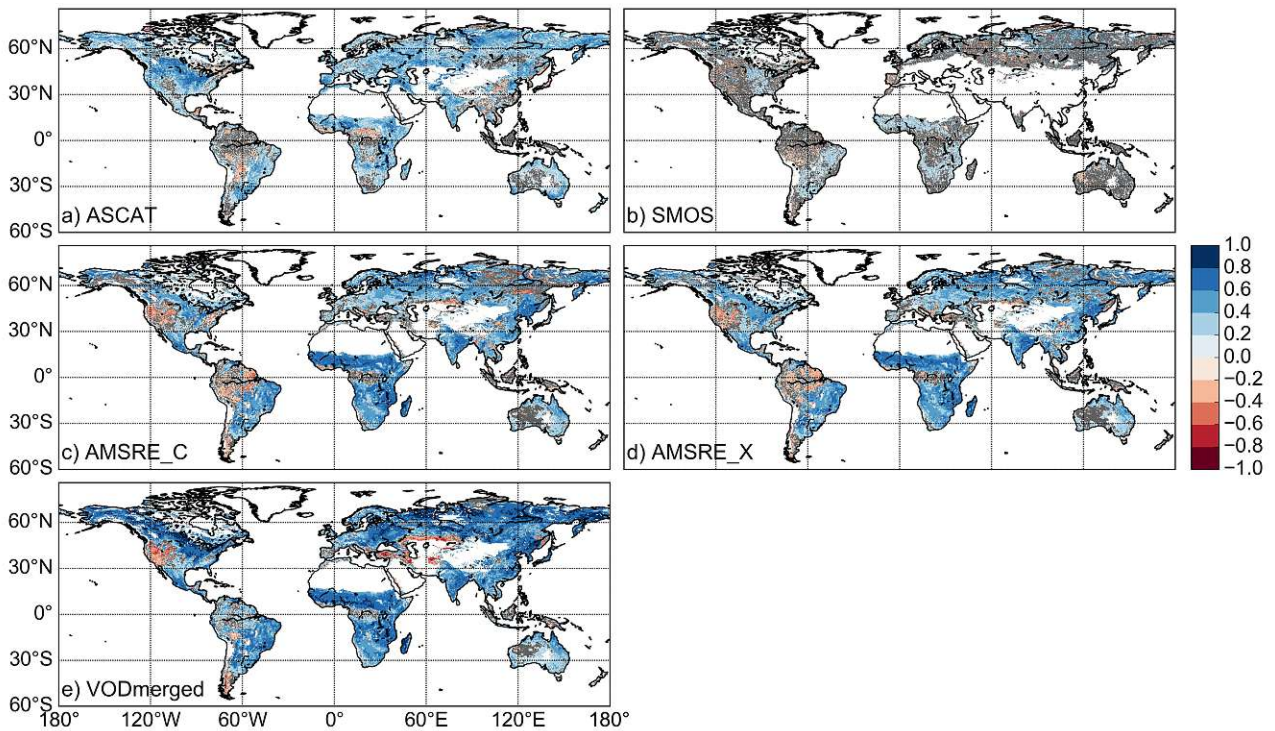
Figure 2.A.7: As Figure 2.A.6 but for the correlation between GPP and $\Delta VOD_{\geq 0}$ data sets.

Chapter 3

A carbon sink-driven approach to estimate gross primary production from microwave satellite observations

3.1 Abstract

Global estimation of Gross Primary Production (GPP) – the uptake of atmospheric carbon dioxide by plants through photosynthesis - is commonly based on optical satellite remote sensing data. This presents a source-driven approach since it uses the amount of absorbed light, the main driver of photosynthesis, as a proxy for GPP. Vegetation Optical Depth (VOD) estimates obtained from microwave sensors provide an alternative and independent data source to estimate GPP on a global scale, which may complement existing GPP products. Recent studies have shown that VOD is related to above-ground biomass, and that both VOD and temporal changes in VOD relate to GPP. In this study, we build upon this concept and propose a model for estimating GPP from VOD. Since the model is driven by vegetation biomass, as observed through VOD, it presents a carbon sink-driven approach to quantify GPP and, therefore, is conceptually different from common source-driven approaches. The model developed in this study uses single frequencies from active or passive microwave VOD retrievals from C-, X- and Ku-band (Advanced Scatterometer (ASCAT) and Advanced Microwave Scanning Radiometer for Earth Observation (AMSR-E)) to estimate GPP at the global scale. We assessed the ability for temporal and spatial extrapolation of the model using global GPP from FLUXCOM and in situ GPP from FLUXNET. We further performed upscaling of in situ GPP based on different VOD data sets and compared these estimates with the FLUXCOM and MODerate-resolution Imaging Spectroradiometer (MODIS) GPP products. Our results show that the model developed for individual grid cells using VOD and change in VOD as input performs well in predicting temporal patterns in GPP for all VOD data sets. For spatial extrapolation of the model, however, additional input variables are needed to represent the spatial variability of the VOD-GPP relationship due to differences in vegetation type. As additional input variable, we included the grid cell median VOD (as a proxy for vegetation cover), which increased the model performance during cross validation. Mean annual GPP obtained for AMSR-E X-band data tends to overestimate mean annual GPP for FLUXCOM and MODIS but shows comparable latitudinal patterns. Overall, our findings demonstrate the potential of VOD for estimating GPP. The sink-driven approach provides additional information about GPP independent of optical data, which may contribute to our knowledge about the carbon source-sink

balance in different ecosystems.

3.2 Introduction

The uptake of the greenhouse gas carbon dioxide by vegetation during photosynthesis, i.e. Gross Primary Production (GPP), is a key ecosystem process. Estimation of GPP from satellite observations commonly uses optical data together with empirical or semi-empirical models (Gilabert et al., 2017; Running et al., 2004) or machine learning approaches (Beer et al., 2010; Jung et al., 2011; Tramontana et al., 2016; Yang et al., 2007). Biophysical properties obtained from optical remote sensing that are often used to estimate GPP include the fraction of Absorbed Photosynthetically Active Radiation (fA-PAR), Normalized Difference Vegetation Index (NDVI), or Leaf Area Index (LAI). These approaches rely on the light-use efficiency theory (Monteith, 1972) whereby GPP depends on the incoming Photosynthetically Active Radiation (PAR), the fraction of PAR that is absorbed, i.e. fAPAR, and the efficiency of converting light to assimilated carbon (Beer et al., 2010; Gilabert et al., 2017; Jung et al., 2011; Running et al., 2004; Tramontana et al., 2016; Yang et al., 2007). Another variable retrieved from optical data is Solar-Induced chlorophyll Fluorescence (SIF), which is a measure for photosynthetic activity (Frankenberg et al., 2011; Guan et al., 2016). SIF has received much attention in recent years, because of its linear relationship with GPP at canopy scale (Damm et al., 2015; Frankenberg et al., 2014; Guanter et al., 2014; Zhang et al., 2016b), especially at coarser temporal resolution like monthly sampling (Guanter et al., 2014). SIF has also been used for estimating GPP globally through the use of artificial neural networks (Alemohammad et al., 2017). Optical biophysical properties provide an estimate for the amount of carbon that is taken up by plants based on the absorption (fAPAR) or re-emission (SIF) of sunlight (source-driven). In recent years, however, it has been proposed that plant growth may be stronger limited by sink- rather than source-activity (Fatichi et al., 2014; Körner, 2015), and that considering sinks of fixed carbon can improve constrains in global vegetation models (Leuzinger et al., 2013).

Microwave Vegetation Optical Depth (VOD) is a measure of the attenuation of microwave radiation caused by vegetation (Woodhouse, 2005) and thus relates to the total vegetation water content (Jackson and Schmugge, 1991). VOD can be retrieved from different frequencies/wavelengths in the microwave region, which can provide information on different parts of the canopy. In theory, lower frequencies like L-band are more sensitive to large plant structures like stems and large branches, while higher frequencies like X-band are more closely related to small structures like leaves and twigs (Woodhouse, 2005). Microwave satellite observations at frequencies below 10 GHz are not affected by cloud cover (Woodhouse, 2005). Therefore, VOD can provide valuable information on the vegetation layer in addition to products derived from optical remote sensing data.

In recent years, studies have proposed to use VOD to estimate aboveground living biomass (Liu et al., 2011, 2015; Momen et al., 2017; Rodríguez-Fernández et al., 2018a; Tian et al., 2016). Biomass and/or temporal change in biomass, however, relate to Net Primary Production (NPP) (Clark et al., 2001a,b; Girardin et al., 2010; Gower et al., 2001; Lavigne and Ryan, 1997; Luyssaert et al., 2007) and to Autotrophic Respiration (R_a) (Lavigne and Ryan, 1997; Ryan, 1990), the sum of which constitutes GPP (e.g. Bonan, 2015; Odum, 1959). Due to this causal relationship between biomass and GPP, a relationship is expected between VOD and GPP. Teubner et al. (2018) showed that both the original VOD time series (VOD) and the temporal change in VOD (ΔVOD) are correlated to GPP and suggested that the combination of VOD and ΔVOD has the potential to provide complementary

information to GPP estimates from optical data.

In this study, we build upon the explorative work of Teubner et al. (2018) and develop a model to estimate GPP based on VOD using Generalized Additive Models (GAM; Hastie and Tibshirani, 1987). Complementary to source-driven approaches, we are proposing a model that is driven by vegetation biomass, as expressed through VOD, which thus presents a sink-driven approach that does not depend on PAR as model input. We assessed the performance of VOD observations from different sensors and multiple frequencies, since it is not clear which frequencies most closely relate to GPP. As input variables to the model, we use different VOD variables, i.e. VOD, ΔVOD and the temporal grid cell median VOD ($mdnVOD$). The latter serves as a proxy for land cover and thus aids the spatial extrapolation of the model to different vegetation types without requiring further ancillary data. Due to the complex relationship between VOD and GPP, we conducted a separate analysis based on SIF using similar experimental setups as for VOD. This additional analysis gives insight into differences in model performance between setups that are not caused by using VOD variables as input to the model. The aim of this study is 1) to assess the model's capability for temporal extrapolation, 2) to evaluate the model's performance in spatial extrapolation and determine the required model structure using model selection, and 3) to perform upscaling of in situ FLUXNET GPP and compare the upscaled VOD-based GPP estimates with global GPP estimates from FLUXCOM and the MODerate-resolution Imaging Spectroradiometer (MODIS).

3.3 Data sets

The analysis is based on the period from 2007 to 2015 and uses VOD data from C-, X- and Ku -band and various GPP data sets. The data sets have different temporal coverage, which is summarized for VOD and GPP data in Table 3.1. Global temporal median maps of the remotely sensed VOD and GPP data sets are displayed in Fig. 3.A.1. For FLUXNET data, a list of the sites and graphs illustrating the location and data coverage are given in Table 3.A.1 and Fig. 3.A.2.

Our analysis was carried out for different passive VOD frequencies from both the Advanced Microwave Scanning Radiometer for Earth Observation System (AMSR-E) and its successor the Advanced Microwave Scanning Radiometer 2 (AMSR2). The overlap period between AMSR2 and in situ FLUXNET data, however, is considerably short (2 years and 5 months) and is further reduced by the lower number of FLUXNET sites in the later period, which potentially leads to less robust results in some parts of the analysis. For this reason and because AMSR-E and AMSR2 generally yielded similar results, the study focuses on results for AMSR-E. For results using AMSR2 frequencies, please see the supplement.

3.3.1 VOD data sets

ASCAT VOD

The Advanced Scatterometer (ASCAT) is an active microwave sensor measuring C-band (5.25 GHz) backscatter in vertical co-polarization and flies onboard the meteorological operational satellite A (MetOp-A). The retrieval of daily VOD at 12.5 km sampling is based on the TU-Wien change detection model developed by Wagner et al. (1999). VOD is derived using slope and curvature of the angular backscatter dependency, which describe the volume scattering caused by vegetation (Melzer, 2013; Vreugdenhil et al., 2016, 2017). The VOD retrieval uses observations from both ascending and

Table 3.1: Data set overview for VOD and GPP data sets. Acronyms – EVI: Enhanced Vegetation Index, fAPAR: fraction of Absorbed Photosynthetically Active Radiation, LAI: Leaf Area Index, MIR: MODIS band 7 - Middle Infrared Reflectance, NDVI: Normalized Difference Vegetation Index, NDWI: Normalized Difference Water Index, LPRM: Land Parameter Retrieval Model.

Variable name	Data set/ sensor	Period used	Frequency/ wavelength/ data input	Sampling	Type	Method/ algorithm	Reference/URL
ASCAT	ASCAT	1/2007 - 12/2015	5.25 GHz	Daily, 12.5 km	Active microwave	TU-Wien change detection	Melzer (2013); Vreugdenhil et al. (2016, 2017)
AMSRE_C, AMSRE_X, AMSRE_Ku	AMSR-E	1/2007 - 9/2011	6.9 GHz, 10.7 GHz, 18.7 GHz	Daily, 0.25°	Passive microwave	LPRMv06	van der Schalie et al. (2017)
AMSR2_C1, AMSR2_C2, AMSR2_X, AMSR2_Ku	AMSR2	7/2012 - 12/2015	6.9 GHz, 7.3 GHz, 10.7 GHz, 18.7 GHz	Daily, 0.25°	Passive microwave	LPRMv06	van der Schalie et al. (2017)
FLUXCOM GPP	FLUXCOM	1/2007 - 12/2015	MODIS EVI, LAI, MIR, NDVI, NDWI	8-daily, 10 km	Optical	Machine learning	Tramontana et al. (2016)
MODIS GPP	MOD17A2H v006	1/2007 - 12/2015	MODIS fAPAR	8-daily, 500 m	Optical	Semi-empirical model	Running et al. (2004); Running and Mu (2015); Zhao et al. (2005)
SIF	GOME2_F v26	1/2007 - 12/2015	740 nm	Monthly, 0.5°	Optical		Joiner et al. (2013); Joiner et al. (2014)
FLUXNET GPP	FLUXNET2015 Tier1	1/2007 - 12/2014	-	Daily	in situ	Eddy covariance	http://fluxnet.fluxdata.org/

descending mode (ascending/descending at 9:30 a.m./p.m. equatorial crossing).

AMSR-E VOD

AMSR-E is a passive microwave sensor measuring brightness temperature at different frequencies. VOD was retrieved using the Land Parameter Retrieval Model (LPRM) v06 (van der Schalie et al., 2017). LPRM is a radiative transfer model, which estimates VOD and soil moisture simultaneously with the use of an analytical solution based on the Microwave Polarization Difference Index (Meesters et al., 2005; Mo et al., 1982). We analyzed VOD from C- (6.9 GHz), X- (10.7 GHz) and Ku-band (18.7 GHz) obtained for descending mode (equatorial crossing at 1:30 a.m.), since the assumption in LPRM that soil and vegetation temperature are similar is best met during nighttime. Data are available at daily, 0.25° sampling.

AMSR2 VOD

AMSR2 measures brightness temperature both at the same frequencies as AMSR-E as well as at additional frequencies. VOD was retrieved analogously to AMSR-E using LPRM v06. In the analysis, we used VOD from C- (C1: 6.9 GHz, C2: 7.3 GHz), X- (10.7 GHz) and Ku-band (18.7 GHz) in descending mode (1:30 a.m. equatorial crossing) at daily, 0.25° sampling.

3.3.2 GPP data sets

FLUXCOM GPP

FLUXCOM is a global GPP product that is based on upscaling site-level eddy covariance estimates of GPP by using variables from optical satellites and different machine learning algorithms including tree-based methods, regression splines, neural networks and kernel methods (Tramontana et al., 2016). For comparability with satellite VOD data, we used the satellite-based version of FLUXCOM GPP. The data set represents the median of 18 ensemble members, which consist of 9 machine learning algorithms applied to both daytime and nighttime GPP estimates. Data are available at 8-daily, 10 km sampling.

MODIS GPP

MODIS GPP (Running et al., 2004; Zhao et al., 2005) is based on the light-use efficiency concept introduced by Monteith (1972) in which absorbed solar energy is related to plant productivity. MODIS GPP is provided by the land product MOD17; the algorithm uses fAPAR derived from optical data for calculating the absorbed PAR (Running et al., 1999, 2000). Several versions of MOD17, differing in spatial and temporal resolution, are available. We used the MOD17A2H v006 GPP, which has 8-daily, 500 m sampling.

GOME-F SIF

SIF observations at 740 nm (GOME-F v26) are obtained from measurements of the Global Ozone Monitoring Experiment-2 (GOME-2) sensor flying onboard MetOp-A (Joiner et al., 2013, 2014, 2016). The retrieval algorithm of SIF proposed by Joiner et al. (2013) utilizes the filling-in of Fraunhofer lines caused by the plants chlorophyll fluorescence. Data are available at monthly, 0.5° sampling.

FLUXNET2015 GPP

FLUXNET2015[1] provides a compilation of in situ flux observations spread around the world. The stations measure water, heat and carbon fluxes by means of the eddy covariance method (Baldocchi, 2003). The carbon dioxide flux, i.e. net ecosystem exchange, is further partitioned into ecosystem respiration and GPP using the daytime (Lasslop et al., 2010) or nighttime (Reichstein et al., 2005) partitioning method. For our analysis, we used GPP estimates from the publicly available Tier 1 data set that were obtained with the daytime partitioning method with a variable friction velocity threshold.

3.3.3   Meteorological data sets

Precipitation

We used daily, 1° precipitation estimates from the Global Precipitation Climatology Project (GPCP) 1DD version 1.2 to aid the interpretation of the time series plot. Precipitation is estimated using a combination of satellite observations and gauge measurements (Huffman et al., 2001). The satellite data include microwave observations of frequencies above 10 GHz and infrared radiation.

Temperature and snow depth

Frozen conditions and snow cover lead to erroneous VOD retrievals. For this reason, we masked VOD observations using skin temperature and snow depth from ERA-Interim. ERA-Interim is a global atmospheric reanalysis produced by the European Centre for Medium-Range Weather Forecasts which incorporates a 4-dimensional variational analysis (Dee et al., 2011). Data are available at 0.7° horizontal sampling at the equator for the period from 1979 onwards.

Aridity Index

Since water availability is a main driver for plant growth, we analyzed results along a gradient of aridity in order to determine whether VOD-based GPP estimates perform differently in different climatic regions. The aridity index is typically calculated as the ratio of the long-term averages of potential evaporation and precipitation (Good et al., 2017; Greve et al., 2014). For computing this index, we used long-term averages of potential evaporation from the Global Land Evaporation Amsterdam Model (GLEAM; Miralles et al., 2011) v3.a (Martens et al., 2017) and precipitation from the Multi-Source Weighted-Ensemble Precipitation (MSWEP; Beck et al., 2017) v1.1 for the period 1980 to 2017. Both data sets are available at 0.25° sampling.

3.4   Theoretical model for estimating GPP based on VOD

For describing the relationship between VOD and GPP, we consider the following equation which relates GPP to NPP and R_a (e.g. Bonan, 2015; Odum, 1959):

$$GPP = R_a + NPP \tag{3.1}$$

R_a represents the portion of the assimilates that is used by plants for their metabolism. R_a can be further separated into growth and maintenance respiration, which are proportional to the change in

---

[1]Fluxnet2015 data set (accessed June 9, 2016): `http://fluxnet.fluxdata.org//data/fluxnet2015-dataset/`

biomass ($\frac{dB}{dt}$) and biomass (B), respectively (Lavigne and Ryan, 1997; Ryan, 1990):

$$R_a = a_0 \ \frac{dB}{dt} + b_0 \ B \tag{3.2}$$

R_a generally depends on temperature and is often modelled by assuming an exponential increase of R_a with temperature (Atkin and Tjoelker, 2003; Atkin et al., 2005; Smith and Dukes, 2013; Tjoelker et al., 2001; Vanderwel et al., 2015; Wythers et al., 2013). Consequently, the coefficients a_0 and b_0 in equation (3.2) are functions of temperature, although this temperature sensitivity is mainly attributed to the maintenance term of R_a (Ryan, 1990). Modelling the relationship between R_a and temperature, however, is not straight forward. Acclimation and adaptation of plants to changes in temperature further modulate the temperature sensitivity of R_a (Atkin and Tjoelker, 2003; Gifford, 2003; Smith and Dukes, 2013; Vanderwel et al., 2015), although these two processes are acting on different time scales (Smith and Dukes, 2013). Therefore, representation of R_a in models presents a complex task (Atkin and Tjoelker, 2003; Atkin et al., 2005; Gifford, 2003; Ryan, 1991; Smith and Dukes, 2013; Vanderwel et al., 2015). For simplicity of our model, we assume that the coefficients a_0 and b_0 are independent of temperature and discuss the potential impact of this simplification in Section 3.7.5.

NPP is the remaining portion of the assimilates, i.e. the difference between GPP and R_a, and contains the following terms (Clark et al., 2001a,b; Girardin et al., 2010; Gower et al., 2001; Luyssaert et al., 2007):

$$\text{NPP} = \frac{dB}{dt} + \text{VOC} + \text{Herbivory} + \text{Root exudates} \tag{3.3}$$

VOC stands for volatile organic compounds and are organic molecules produced by plants that are released into the ambient air. VOC may play an important role in ecology and atmospheric chemistry but constitute only a small fraction of NPP (Guenther, 2002; Kesselmeier et al., 2002). Herbivory describes the loss of above- and belowground plant biomass through animals that are feeding on these plants. Root exudates are plant-produced compounds that are released into the ground to enhance nutrient uptake or feed mycorrhiza and can also be used as a defense mechanism (Bais et al., 2006; Bertin et al., 2003; Jones et al., 2009). All these terms are not directly reflected in VOD and are thus neglected in the current model description for relating VOD to GPP. Combining equations (3.1)-(3.3) and setting $a = 1 + a_0$ and $b = b_0$, we arrive at the following differential equation for GPP:

$$\text{GPP} = a \ \frac{dB}{dt} + b \ B \tag{3.4}$$

a and b represent coefficients for growth and maintenance related terms, respectively, analogous to the concept developed by Ryan (1990) for R_a, i.e. equation (3.2), but now extended for GPP.

The last step in the formulation of the relationship between VOD and GPP requires a description of the relationship between VOD and biomass. This relationship, or more specifically that between VOD and aboveground biomass (AGB), is not straightforward. Liu et al. (2015) proposed an empirical, non-linear function for converting VOD to AGB using a passive merged VOD data set. Similar to this concept, but without explicitly stating the relationship between AGB and VOD, we assume that AGB can be expressed as a function of VOD:

$$\text{AGB} = f(VOD) = \widetilde{VOD} \tag{3.5}$$

Assuming that above- and belowground terms in equation (4.2) are proportional, which allows to express B as a function of VOD, we arrive at the relationship between VOD and GPP, which can be described by the following differential equation:

$$\text{GPP} = a\, \frac{\widetilde{dVOD}}{dt} + b\, \widetilde{VOD} + c \tag{3.6}$$

c is a time-invariant offset, which is added from a mathematical point of view and does not necessarily reflect the neglected terms in equation (3.3) but rather aids the conversion of VOD to GPP if the offset is not already included in $f(VOD)$.

Equation (4.3) presents the theoretical concept in this study, which we aim to model for different VOD data sets through the use of GAM (Hastie and Tibshirani, 1987).

3.5 Methods

3.5.1 Generalized Additive Models

GAM is a regression approach which can utilize different link functions for fitting a limited set of predictor variables ($\mathbf{x}$) against the expected value of the response variable (y) (Hastie and Tibshirani, 1987). For calculating the conditional expected value ($\mathbb{E}[y \mid \mathbf{x}]$), the algorithm requires specification of the data distribution for the response variable. The approach allows non-linear and non-monotonic relationships between a response variable and predictor variables, which are represented by fitting smooth spline functions (f) for each predictor (Hastie and Tibshirani, 1987, 1990). As such, GAM does not require specification of the underlying relationship between predictor and response variable. Since we do not explicitly know the shape of the relationship between biomass and each VOD data set, GAM presents a suitable method in this study for estimating GPP based on VOD.

For the analysis, we used LinearGAM from the python package pygam (Servén et al., 2018), which uses the normal distribution together with the identity as link function. In this case, GAM with p input variables has the form (Hastie and Tibshirani, 1987):

$$\mathbb{E}[y \mid \mathbf{x}] = \alpha + \sum_{j=1}^{p} f_j(x_j) \tag{3.7}$$

We used LinearGAM with 25 splines of order 3, which allows variability in the shape of the fitted spline across the data range, together with a value of 200 for the smoothing parameter lambda, which provides strong smoothing to ensure generalizability.

We applied GAM by fitting different sets of input variables against global or in situ GPP estimates. To indicate which set of input variables was used for training GAM, we refer to the model as GPP() with a list of input variables in parenthesis. For example, GPP(VOD, ΔVOD) denotes a GAM setup that uses VOD and ΔVOD as input.

3.5.2 Experimental setups

Our analysis comprises three experiments. The first experiment assesses the model's performance in temporal extrapolation, while the second experiment evaluates the model's capability in spatial extrapolation using cross validation and model selection. These experiments allow to determine the

model's performance during periods or at locations it has not been trained on, which relates to the situation during the upscaling of in situ GPP assessed in the third experiment.

Testing temporal extrapolation

For testing the model's ability to reproduce the temporal dynamics of GPP, we trained GPP(VOD, ΔVOD) at each grid cell against the global GPP from FLUXCOM. The comparison with an existing global GPP product has the advantage of minimizing the impact of scale differences, which are often observed for in situ observations versus satellite data. It can thus demonstrate if the model can be used in general for estimating GPP. For the analysis, we split the data in time using the first two years of each data set for training the model (AMSR-E, ASCAT, SIF: 1/2007 to 12/2008; AMSR2: 7/2012 to 6/2014) and the remaining period for testing (AMSR-E: 1/2009 to 9/2011; ASCAT, SIF: 1/2009 to 12/2015, AMSR2: 7/2014 to 12/2015). To support global results, we repeated the analysis using in situ FLUXNET observations. For this setup, AMSR2 data are omitted since the overlap period with FLUXNET extends only through 2014.

In addition to the analysis of GPP(VOD, ΔVOD), we determined the added value of using the combination of VOD and ΔVOD compared to VOD or ΔVOD alone. The reason for treating VOD and ΔVOD separately against our proposed theory, was to exclude the possibility that either signal alone is able to match the GPP signal merely by applying a non-linear regression like GAM.

Testing spatial extrapolation using cross validation and model selection

Using leave-site-out cross validation with FLUXNET GPP as target variable, we assessed the model's ability for spatial extrapolation. For each site, GPP(VOD, ΔVOD) or GPP(SIF) was trained with data from all sites except the site under evaluation. The model was then applied to the data that was left out and compared against the target variable. As the data were split in space, the training and testing period each span the full overlap period with FLUXNET for each data set. Apart from the full signal, we also assessed the performance of anomalies of the resulting GPP estimates in order to evaluate the strength of the relationship in the absence of seasonality. Anomalies were calculated as differences to the mean seasonal cycle during the testing period for the VOD- or SIF-based GPP estimates (i.e., after model application) and FLUXNET GPP.

We further assessed if the additional use of the temporal grid cell median of each data set ($mdnVOD$ or $mdnSIF$) can improve the spatial extrapolation of the model, i.e. GPP(VOD, ΔVOD, $mdnVOD$) or GPP(SIF, $mdnSIF$). $mdnVOD$ is a static component for each data set, which varies with each grid cell and thus does not contribute to the temporal dynamic of the resulting estimate. $mdnVOD$ identifies areas of similar biomass and thus further relates to land cover, since grassland generally has a lower biomass than shrubland, which in turn has a lower biomass than a dense forest. In contrast, $mdnSIF$ identifies areas of similar photosynthetic activity and therefore reflects a different property than $mdnVOD$.

To assess whether an improvement in model performance can be attributed to a gain in information through the addition of the respective variable or is caused by an additional degree of freedom, we computed the Akaike Information Criterion (AIC; Akaike, 1974). For this analysis, we randomly split the station data into two data sets. We used one half of the stations for training and the remaining half for testing.

Upscaling

In the third experiment, we estimated GPP globally based on VOD using the best performing model setup as assessed during cross validation and model selection. The upscaling was performed similarly to cross validation with the difference that the model for each setup was trained against all available in situ FLUXNET GPP. After applying the model to the global VOD data sets, we evaluated the model's performance by comparing the VOD-based GPP estimates with global GPP estimates from FLUXCOM and MODIS. For the analysis of mean annual GPP, we additionally performed an uncertainty analysis to determine the influence of the choice of the stations on the GPP estimation. For this, we repeated the VOD-based upscaling ten times, each time reducing the number of stations by 10%. The excluded stations were randomly drawn without replacement. Therefore, each model run in the uncertainty analysis is based on data from 90% of the stations.

3.5.3 Data preparation

The analysis is based on two different resolutions: for the comparison between VOD, FLUXCOM and MODIS data, the common sampling is 8-daily, 0.25° while for the comparison with SIF, the common sampling is monthly, 0.5°. We aggregated data sets with a higher resolution using the average over 8 days or the average over the grid cell. For data sets with a lower spatial resolution like snow depth and temperature data, we performed nearest neighbor resampling.

VOD observations were masked when temperature was below 0°C and snow cover was present. The masking was also applied to GPP data sets for comparability. In addition to snow and temperature masking, VOD from passive sensors was masked for radio frequency interference using the accompanying flags, since it can also lead to erroneous retrievals of VOD (Li et al., 2004; Njoku et al., 2005).

We approximate the derivative of VOD at each grid cell ($\mathbf{x}_i$) with the change of the smoothed VOD signal between two consecutive VOD observations:

$$\Delta VOD(\mathbf{x}_i, t_j) = VOD(\mathbf{x}_i, t_j) - VOD(\mathbf{x}_i, t_{j-1}) \tag{3.8}$$

The smoothing was computed using a Savitzky-Golay filter (Savitzky and Golay, 1964) with a window size of 11 time steps for 8-daily data and 5 time steps for monthly data. The window size for each resolution was chosen after visual inspection of the smoothed time series at the location of the FLUXNET sites. Additionally, we performed a cross validation similar to the temporal extrapolation experiment for 8-daily AMSRE_X and for GPP(VOD, ΔVOD) but using different window sizes during the computation of ΔVOD (Figs. 3.A.3). Results for Spearman correlation and $RMSE$ confirmed that a window size of 11 time steps is a suitable choice presenting a trade-off between a preferably high median correlation, low median $RMSE$ and still relatively low window length.

During cross validation, we additionally assessed the performance of the GPP anomalies relative to the mean seasonal cycle. We calculated anomalies for sites with more than two years of data using the python package pytesmo (Paulik et al., 2015).

3.5.4 Statistical analysis

Prior to the analysis, we tested if grid cell data of the global data sets follow normal distribution using the D'Agostino and Pearson's test (D'Agostino, 1971; D'Agostino and Pearson, 1973). We found that

on average 75% of the grid cells differ from normal distribution. For this reason, we calculated the non-parametric Spearman rank correlation and used the temporal grid cell median instead of the mean in the analysis.

We evaluated model performance by calculating the Spearman rank correlation coefficient (r) and root mean square error ($RMSE$). For the leave-site-out cross validation, we additionally analyzed the index of agreement (IoA), which is a standardized measure for the model prediction error and is defined after Willmott (1981) as:

$$IoA = 1 - \frac{\sum_{i=1}^{n}(p_i\check{\ }o_i)^2}{\sum_{i=1}^{n}(\mid p_i\check{\ }\mathbf{\bar{o}}\mid + \mid o_i\check{\ }\mathbf{\bar{o}}\mid)^2} \quad \text{with } n = \text{number of observations} \tag{3.9}$$

where p represents the model output and o the in situ observations. The index ranges between 0 (worst agreement) and 1 (best agreement).

For model selection, we computed AIC using the python package RegscorePy[2]. AIC is a relative measure for the goodness of fit for different model setups while penalizing higher numbers of input variables (Akaike, 1974). The model setup with the lowest AIC is then considered as the optimal choice.

3.6 Results

3.6.1 Temporal extrapolation

The application of GAM for each grid cell is illustrated for a grid cell dominated by rainfed cropland in Fig. 3.1. In this example, GPP(VOD, ΔVOD) is able to capture the temporal dynamics of FLUXCOM GPP (Fig. 3.1a). In contrast, VOD shows a positive temporal lag with respect to GPP (Fig. 3.1b), while ΔVOD results in a negative lag with GPP. Making use of both VOD and ΔVOD, the model can largely compensate the observed lags for the individual signals of VOD and ΔVOD.

Applying the model per grid cell globally at 8-daily, 0.25° sampling, the resulting GPP estimates show high temporal agreement with FLUXCOM GPP (Fig. 3.2). Correlations are higher for passive VOD data sets ($0.69 \leq$ median $r \leq 0.72$) than for the active VOD data set (median r=0.61). For passive VOD data sets, correlations are especially high over Africa, parts of Australia and Europe. For the active VOD, high correlations are observed over Europe, North America and parts of South America. Consistent with the correlation results, $RMSE$ (Fig. 3.A.4) yields lower global median values for passive VOD data sets ($0.85 \leq$ median $RMSE \leq 0.88$ $gCm^{-2}d^{-1}$) than for the active VOD (median $RMSE$=0.99 $gCm^{-2}d^{-1}$). Comparing the different frequencies of the passive VOD data sets, Ku-band results in the lowest median $RMSE$ closely followed by X-band. Regions with lowest $RMSE$ are observed over Australia for all VOD data sets, while regions with highest $RMSE$ are found mainly in northern latitudes.

The correlations increase for all data sets when performing the analysis at monthly, 0.5° sampling (Table 3.A.2), yielding median r between 0.80 and 0.82 for passive VOD and 0.74 for the active VOD. When repeating the analysis using either VOD or ΔVOD alone as input, we found that GPP(VOD, ΔVOD) outperforms GPP(VOD) and GPP(ΔVOD) at both resolutions (Table 3.A.2) with an average difference in median r of about 0.1 and 0.2 for GPP(VOD) and GPP(ΔVOD), respectively. The different frequencies of AMSR-E generally yield similar results. However, X-band data consistently

---

[2]RegscorePy v1.0: `https://pypi.org/project/RegscorePy/`
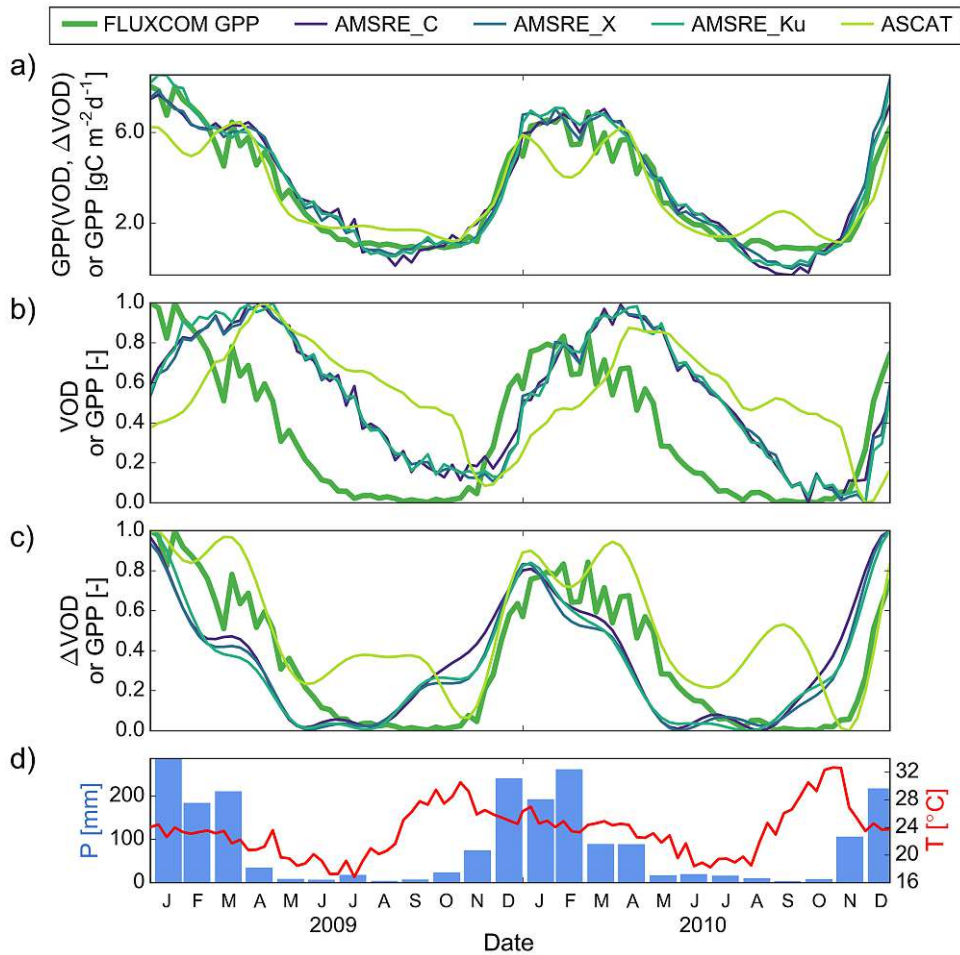
Figure 3.1: Time series plot for a grid cell dominated by rainfed cropland (35.125°E, 15.125°S) for different VOD data sets for the period 1/2009 to 12/2010: 8-daily FLUXCOM GPP and a) GPP(VOD, ΔVOD), b) VOD and c) ΔVOD. GPP(VOD, ΔVOD) was trained at this grid cell against FLUX-COM data for the period 1/2007 to 12/2008. Data in (b) and (c) are scaled between 0 and 1 to aid visual comparison of the temporal dynamics. (d) Monthly precipitation and 8-daily surface temperature.
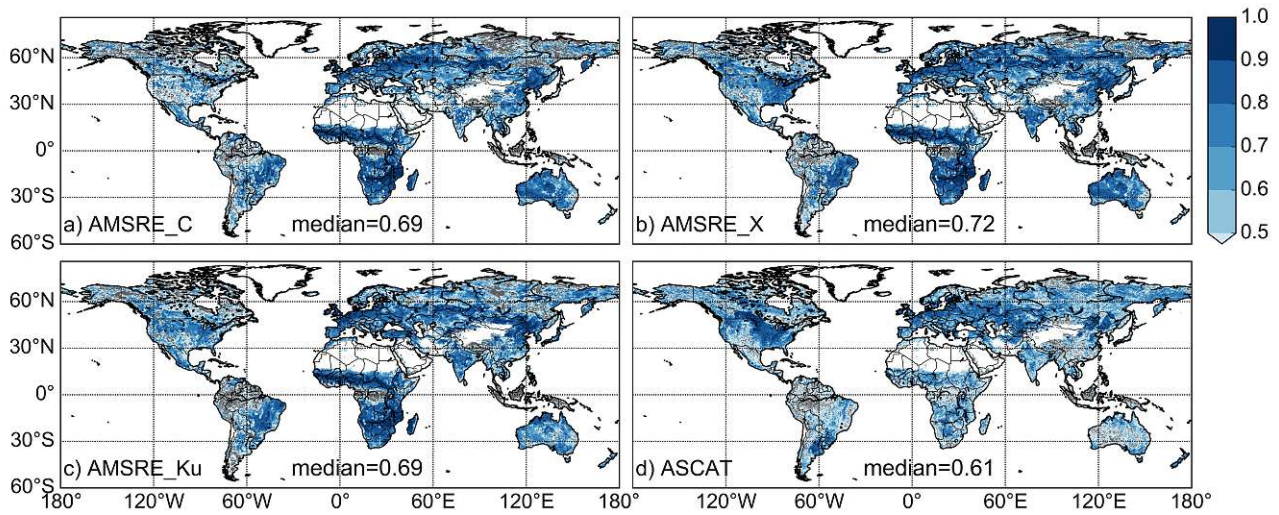
Figure 3.2: Spearman rank correlation (r) between FLUXCOM GPP and GPP(VOD, ΔVOD) for different VOD data sets for the testing period (AMSR-E: 1/2009 to 9/2011; ASCAT: 1/2009 to 12/2015). The analysis is based on data at 8-daily and 0.25° sampling. GPP(VOD, ΔVOD) is trained at each grid cell separately against FLUXCOM using data from the period 1/2007 to 12/2008. Correlations that are not significant (p>0.05) are masked in grey. The median values denote the median of significant correlations for each data set.

showed the highest correlation at both resolutions. This finding was also observed for AMSR2 frequencies (Table 3.A.2). Compared with correlations obtained for SIF (median r=0.73), GPP(VOD, ΔVOD) at monthly, 0.5° sampling shows comparable or slightly higher median correlations for active and passive VOD, respectively.

The added value of combing VOD and ΔVOD can be further confirmed using in situ FLUXNET GPP. Correlations for GPP(VOD, ΔVOD) are higher than for the individual signals, i.e. GPP(VOD) and GPP(ΔVOD) (Fig. 3.A.5) with an average increase in median r of about 0.1 and 0.3 for GPP(VOD) and GPP(ΔVOD), respectively. Comparing median correlations of the in situ analysis with those obtained in the global comparison, the median r for SIF yields almost the same value (0.73 obtained for global GPP compared to 0.72 for in situ GPP). For VOD data sets, however, median r for the in situ analysis is on average lower by 0.1 than for the global comparison.

These results, especially for the global comparison, demonstrate the model's capability in temporal extrapolation and support our theory of representing the relationship between VOD and GPP with a differential equation.

3.6.2 Spatial extrapolation

Using leave-site-out cross validation, we evaluated the performance in spatial extrapolation of the relationship between VOD and GPP. For the full signals (Fig. 3.3, 3.A.6 and 3.A.7), the performance for SIF is generally higher than for VOD data. Median values of IoA and r are comparable to or lower for VOD than for SIF, while median $RMSE$ is higher for VOD than for SIF in all cases. The addition of the temporal median as input to GAM does not appear to have the same effect for VOD and SIF. While the performance for VOD increases when adding $mdnVOD$, SIF does not appear to benefit from including $mdnSIF$ since the correlations do not differ markedly between GPP(SIF) and GPP(SIF, $mdnSIF$). For VOD, however, the increase in performance upon adding $mdnVOD$ indicates that the offset, which is already implicitly included in GAM, is not a globally constant value

but instead varies for each grid cell. The relationship between VOD and GPP thus is additionally modified by a static component of vegetation biomass within a grid cell as represented by $mdnVOD$. In contrast, the offset in the relationship between SIF and GPP presents a global value and does not vary with $mdnSIF$.

Results for the anomalies of the VOD- or SIF-based GPP estimates (Fig. 3.4, 3.A.8 and 3.A.9) reveal a slightly higher performance for VOD than for SIF. Median values of IoA and r are comparable or in some cases higher for VOD than for SIF, while median $RMSE$ is lower for VOD than for SIF in all cases. Including the temporal median does not affect the metrics except for IoA for VOD. In this case, the anomalies for GPP(VOD, ΔVOD, $mdnVOD$) result in slightly higher IoA values than for GPP(VOD, ΔVOD).

For the different AMSR-E frequencies, the cross validation results further reveal that X-band data result in higher performance than C- and Ku-band data in most cases, which is especially true for data at 8-daily, 0.25° sampling.

The two extrapolation experiments for the full signals further show that correlations for the spatial extrapolation (Fig. 3.3) are generally lower than for the temporal extrapolation (Fig. 3.A.5). Even when adding $mdnVOD$, median r during spatial extrapolation is on average lower by about 0.1 than during temporal extrapolation at both resolutions. Similarly, SIF also experiences a reduction in correlation during spatial extrapolation compared to temporal extrapolation. The difference in median r, however, is about 0.05 and thus smaller than for VOD. This indicates that the reduction in performance for VOD data is not alone caused by the model representation itself but is also strongly affected by scale differences between point measurements and the spatial coverage of the grid cell data.

Cross validation results for the full signals for AMSR2 (Fig. 3.A.10, 3.A.11 and 3.A.12) are generally similar to those obtained for AMSR-E. AMSR2 frequencies, however, show a slight decrease in performance for r and IoA and a slight increase in performance for $RMSE$ compared to AMSR-E frequencies (Fig. 3.A.12). Consistent with AMSR-E data, AMSR2 X-band often shows higher performance than the remaining frequencies.

The previous results suggest that the combination of all three input variables, i.e. VOD, ΔVOD and $mdnVOD$, can improve model performance. Results of AIC for the different model setups relative to AIC for GPP(VOD, ΔVOD, $mdnVOD$) in Fig. 3.5 further confirm this finding. For all VOD data sets at both resolutions, the combination of VOD and ΔVOD yields lower AIC values than for each input variable alone. When adding $mdnVOD$, AIC is further reduced in the majority of cases. Exceptions from this rule are found for AMSRE_C and AMSRE_X at 8-daily, 0.25° sampling, where the use of all three variables increases AIC. Since this finding is not consistent with results at monthly, 0.5° sampling for the same frequencies, we suspect that this might be an artifact of the choice of stations. We thus still suggest the use of all three variables for upscaling GPP based on VOD data. In case of SIF, the difference in AIC between GPP(SIF) and GPP(SIF, $mdnSIF$) is negligible. This confirms that, unlike for VOD, the relationship between SIF and GPP does not depend on the data set median.

3.6.3 Upscaling of in situ GPP

Based on the results for cross validation and model selection, we used GPP(VOD, ΔVOD, $mdnVOD$) for the global upscaling with VOD and GPP(SIF) for the upscaling with SIF for further analysis. We will put an emphasis on the output from X-band due to the overall better performance during the temporal and spatial extrapolation experiments.
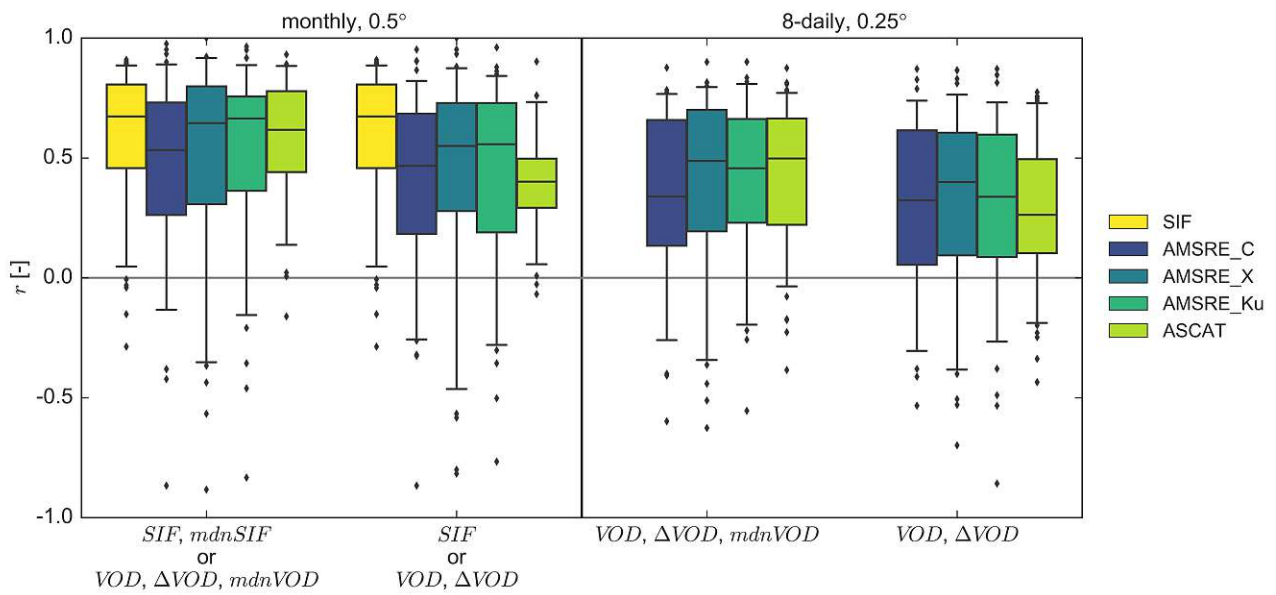
Figure 3.3: Leave-site-out cross validation for Spearman rank correlation (r) at monthly, 0.5° and 8-daily, 0.25° sampling. The analysis is based on the full signals of in situ FLUXNET GPP and GPP estimates based on VOD or SIF. Labels on the x-axis indicate which input variables are used for each model. Box plot whiskers extend to the 5th and 95th data percentile. Abbreviations – $mdnSIF$: temporal grid cell median SIF; ΔVOD: temporal change in VOD between two consecutive observations; and $mdnVOD$: temporal grid cell median VOD.
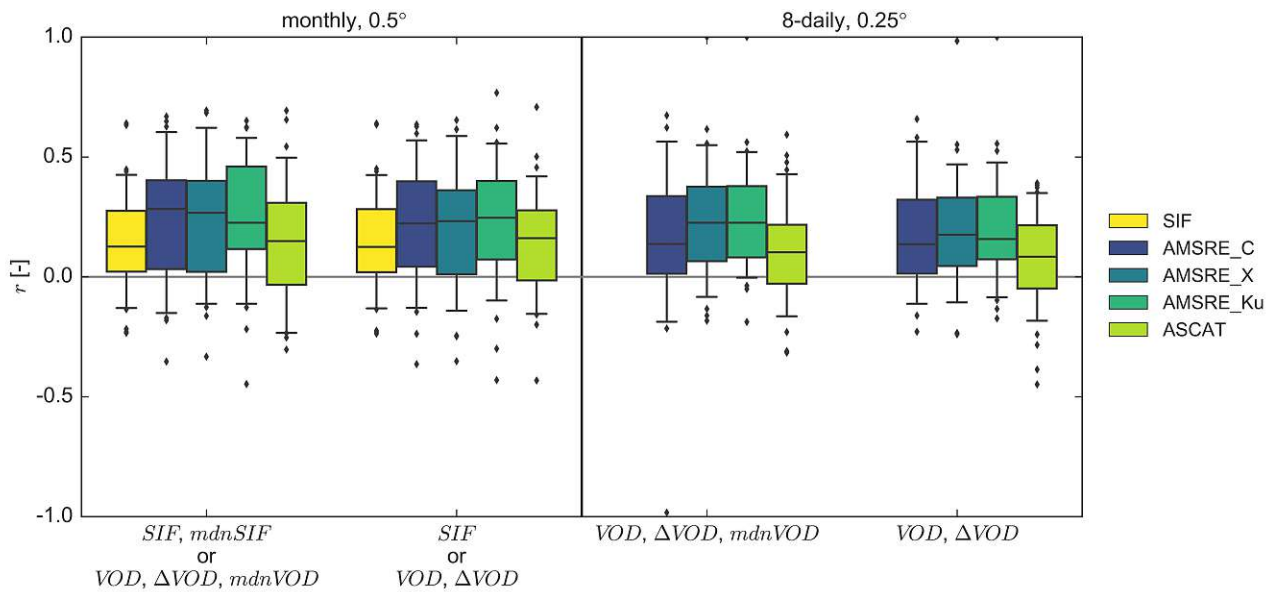
Figure 3.4: As Fig. 3.3 but for the anomalies of in situ FLUXNET GPP and GPP estimates based on VOD or SIF.
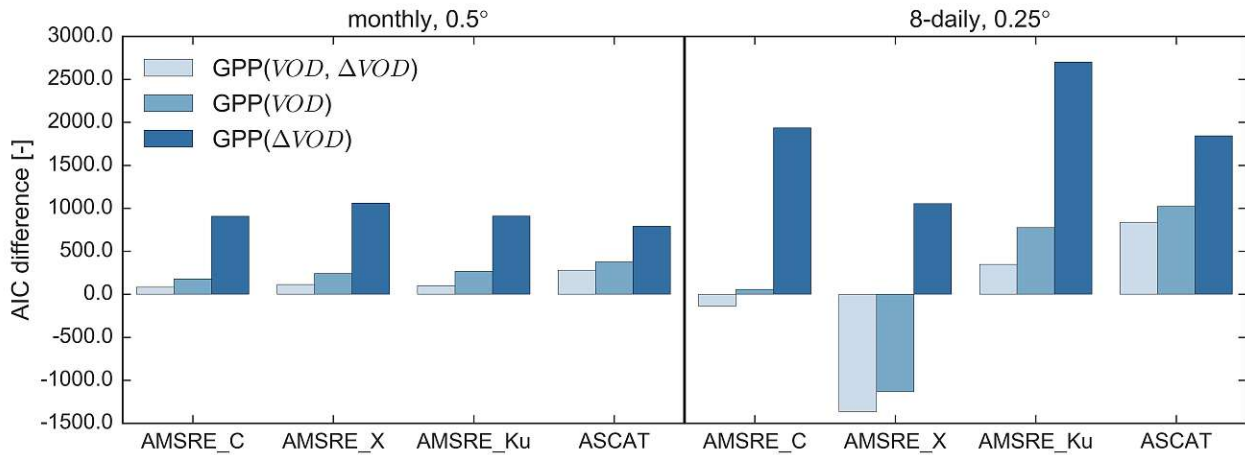
Figure 3.5: Difference in AIC between model setups with respect to AIC for GPP(VOD, ΔVOD, $mdnVOD$) for each VOD data set. For SIF, the AIC difference between GPP(SIF) and GPP(SIF, $mdnSIF$) is very low (1.67) compared with VOD data sets and therefore not displayed. The analysis is based on data at monthly, 0.5° or 8-daily, 0.25° sampling. Positive values indicate model improvement when using all three variables as input compared to models with a lower number of input variables.

Relationship between VOD and GPP

The partial dependence plots for GPP(VOD, ΔVOD, $mdnVOD$), which are examplified for AMSRE_X in Fig. 3.6, demonstrate the contribution of the three input variables to the model. For all VOD data sets, we observed that the functions for VOD and ΔVOD mainly increase, while the function for $mdnVOD$ decreases. The increase for ΔVOD is true for the region where the majority of data are located and the confidence interval is small. For AMSRE_X, this region ranges between -0.3 and 0.4 (Fig. 3.6e). The inverse relationship between VOD and $mdnVOD$ and the additive linking of variables in GAM suggest that $mdnVOD$ is subtracted from VOD.

Global correlation of upscaled GPP

Results for GPP(VOD, ΔVOD, $mdnVOD$) at 8-daily, 0.25° sampling show moderate temporal agreement with FLUXCOM and MODIS GPP (Fig. 3.7). Median r ranges between 0.54 and 0.62 for FLUXCOM and between 0.52 and 0.60 for MODIS. The correlations also include some negative values (Fig. 3.A.13). For significant correlations, the fraction of negative correlations lies between 5 to 9% for passive VOD and about 12% for active VOD. Highest median correlations are observed for X-band data, which is consistent with the results from temporal and spatial extrapolation. At monthly, 0.5° sampling, the global median r increases, ranging between 0.67 and 0.71 for FLUXCOM and between 0.66 and 0.70 for MODIS. For GPP(SIF), median r reaches 0.71 for FLUXCOM and 0.66 for MODIS.

Results for AMSR2 frequencies (Fig. 3.A.15) are generally similar to those obtained for AMSR-E, although AMSR2 frequencies yield slightly lower median correlations than AMSR-E frequencies.

Comparing correlations with FLUXCOM between the upscaling and the global temporal extrapolation (Section 3.6.1), median r for SIF is similar. For VOD, however, correlations for the upscaling are markedly lower than during temporal extrapolation, which is consistent with the reduction in model performance during cross validation.
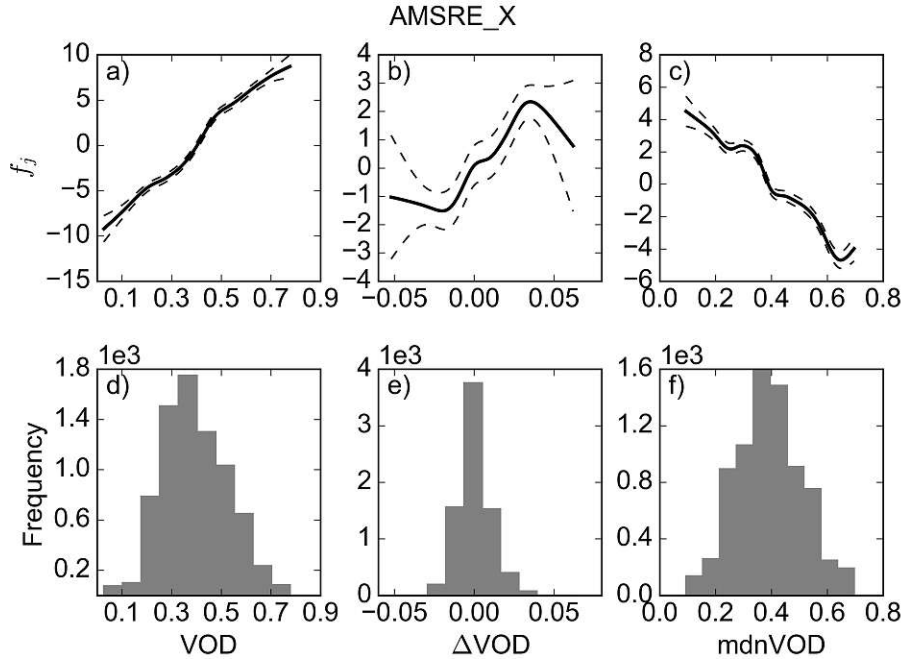
Figure 3.6: GAM Partial dependence plots for GPP(VOD, ΔVOD, $mdnVOD$) obtained during upscaling (a-c) and histogram of input variables (d-f) for AMSRE_X at 8-daily and 0.25° sampling. Dashed lines in (a-c) indicate the confidence intervals.
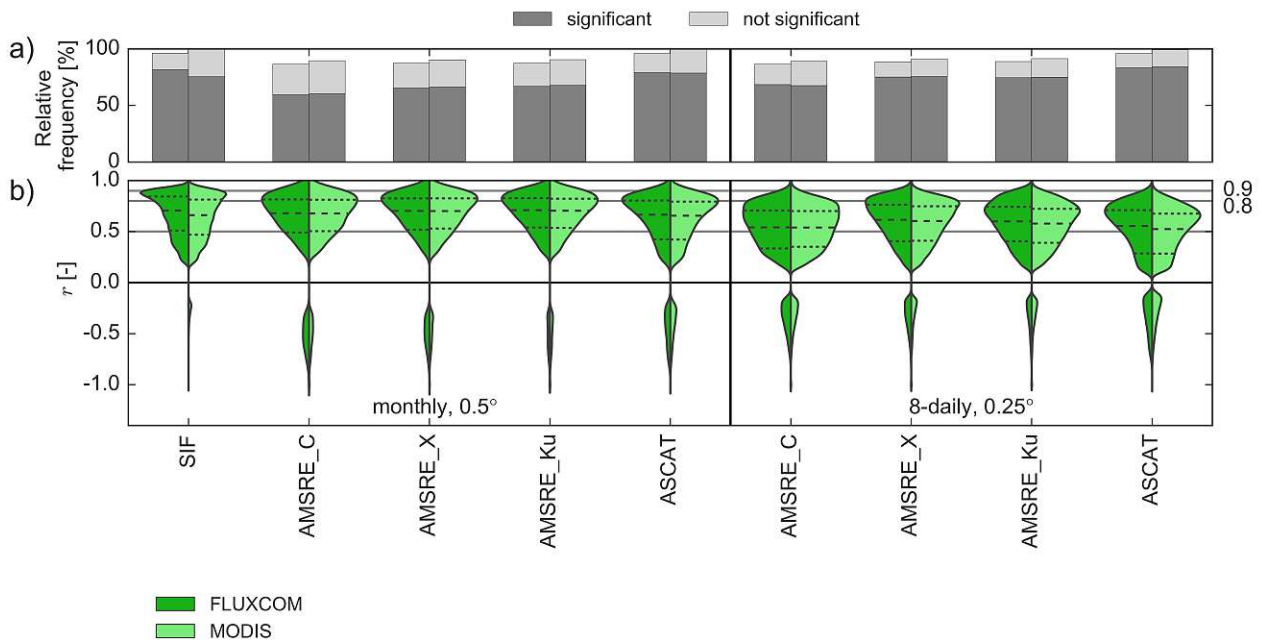
Figure 3.7: Spearman rank correlation (r) between GPP data sets (FLUXCOM, MODIS) and upscaling for GPP(VOD, ΔVOD, $mdnVOD$) or GPP(SIF). Data were trained against in situ GPP estimates (FLUXNET) at 8-daily, 0.25° or monthly, 0.5° sampling. a) Relative frequency of grid cells with significant and not significant correlations with respect to all possible land grid cells at each resolution. Areas that do not contain results relate to gaps obtained during masking for radio frequency interference or to not produced pixels in the original data products. b) Violin plot of significant correlations. Horizontal grey lines indicate correlation values of 0.5, 0.8 and 0.9. Dashed lines indicate the median (long dashes) and the 25th and 75th percentile (short dashes).

Comparison of annual GPP

In addition to assessing the temporal dynamics, we compared mean annual GPP for GPP(VOD, ΔVOD, $mdnVOD$) from AMSRE_X with mean annual GPP for FLUXCOM and MODIS. The analysis is based on data points where all three data sets are available. In general, GPP(VOD, ΔVOD, $mdnVOD$) shows the expected spatial pattern with highest values observed in tropical regions (Fig. 3.8a). Nevertheless, GPP(VOD, ΔVOD, $mdnVOD$) for AMSRE_X tends to overestimate annual GPP in many regions compared to FLUXCOM and MODIS (Fig. 3.8b-c). Closest agreement between AMSRE_X and FLUXCOM or MODIS is observed for tropical regions. Consistent with these results, we observed lowest differences between AMSRE_X and FLUXCOM or MODIS at low aridity (Fig. 3.9), which represents very humid regions like the tropics. Under mesic conditions, differences between products are slightly higher than for very dry or very humid regions.

The observed overestimation is also apparent in the zonal mean (Fig. 3.8d). GPP(VOD, ΔVOD, $mdnVOD$) consistently overestimates annual GPP from FLUXCOM and MODIS and is closest to FLUXCOM and MODIS near the equator. Despite the overestimation, GPP(VOD, ΔVOD, $mdnVOD$) shows similar latitudinal features as for FLUXCOM and MODIS. The uncertainty analysis of GPP(VOD, ΔVOD, $mdnVOD$) for AMSRE_X further demonstrates that the choice of stations for the upscaling has an effect on the GPP estimation (Fig. 3.8d). The range of the ten model runs is larger in the tropics and the southern hemisphere than in the northern hemisphere, which is caused by differences in station density in these regions. The map of the standard deviation for the ten model runs (Fig. 3.A.16) shows that differences between the model runs are most pronounced in the tropics, the Sahel, southern parts of Africa and large parts of Australia.

GPP(VOD, ΔVOD, $mdnVOD$) for AMSR2_X results in a higher agreement with FLUXCOM and MODIS than for AMSRE_X. In contrast to AMSRE_X, AMSR2 yields smaller differences in annual GPP with FLUXCOM and MODIS (Fig. 3.A.17a-c), which is in line with the smaller $RMSE$ observed for AMSR2 during cross validation. Annual GPP for AMSR2, however, also exhibits areas where FLUXCOM and MODIS are underestimated, which are located mainly in the Sahel and Australia. The latitudinal distribution of annual GPP (Fig. 3.A.17d) shows that AMSR2_X overall yields a closer agreement between with FLUXCOM or MODIS than for AMSRE_X. Similar as for AMSRE_X, AMSR2_X deviates less from FLUXCOM and MODIS in the tropics.

3.7 Discussion

3.7.1 Relationship between VOD and GPP

Our study presents a model for estimating GPP based on VOD, which describes the relationship between VOD and GPP through a differential equation. The model uses different VOD variables, i.e. VOD, ΔVOD, and $mdnVOD$, as input. The approach is based on the assumption that VOD provides an estimate for aboveground living biomass (Liu et al., 2011, 2015), which has been employed by multiple studies for detecting trends in biomass (Andela et al., 2013; Liu et al., 2013a,b, 2015; Van Marle et al., 2016). In support of this theory, Tian et al. (2016) have demonstrated the applicability of the biomass-VOD relationship in a dryland ecosystem.

The relationship between biomass and VOD, however, is rather complex. Since VOD presents a measure of vegetation water content (Jackson and Schmugge, 1991), it can also be considered as the product of biomass and relative water content (Momen et al., 2017), a quantity that is closely related
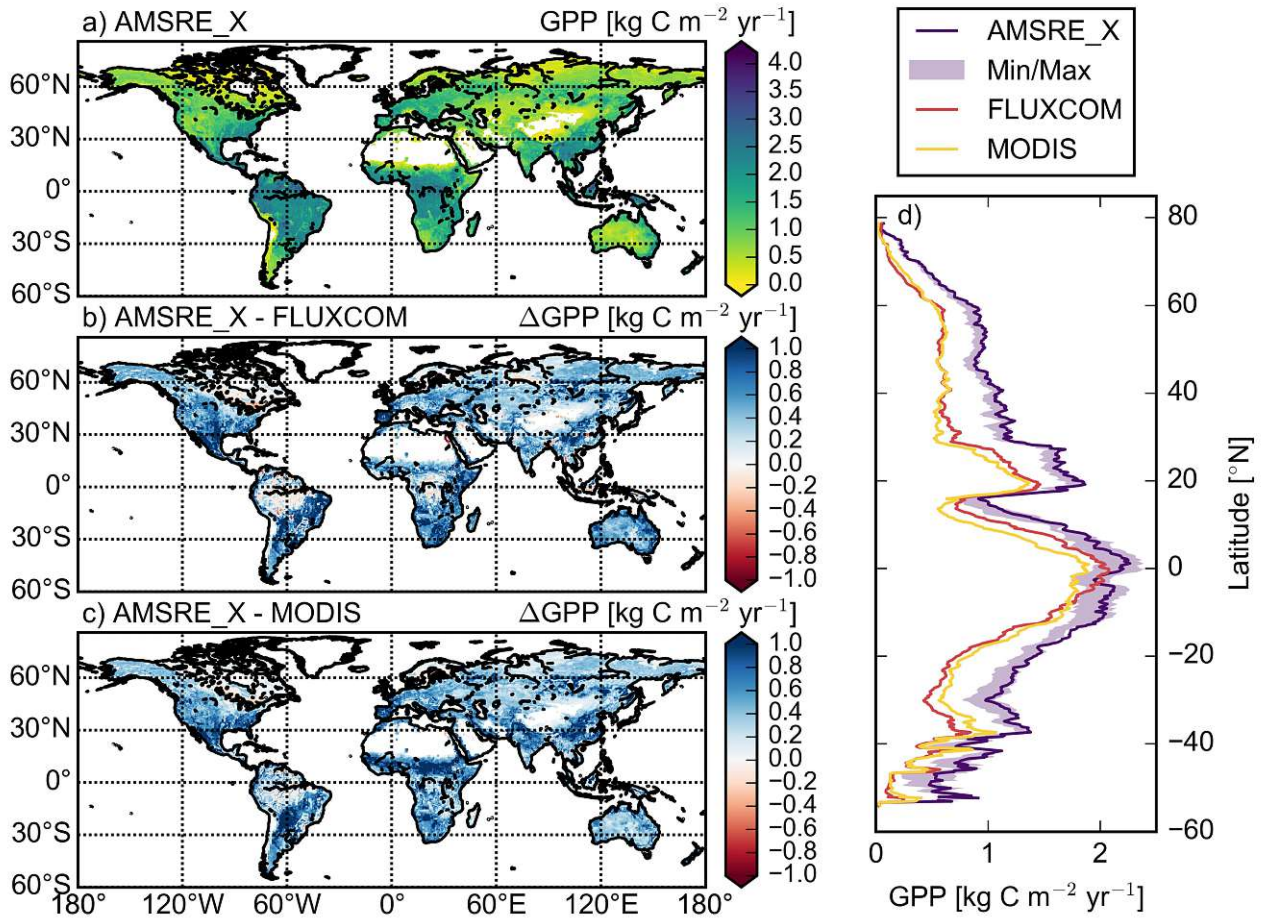
Figure 3.8: Mean annual GPP for the period 2007 to 2010: a) upscaling of GPP(VOD, ΔVOD, $mdnVOD$) for VOD AMSRE_X, b) difference in mean annual GPP between FLUXCOM and AM-SRE_X c) difference in mean annual GPP between MODIS and AMSRE_X. Values in (b) and (c) are displayed between -1 and 1. d) Zonal mean of mean annual GPP. Estimates for GPP(VOD, ΔVOD, $mdnVOD$) were produced using data at 8-daily, 0.25° sampling. The area denoted by Min/Max represents the minimum and maximum of the zonal means for the ten model runs obtained during the uncertainty analysis for GPP(VOD, ΔVOD, $mdnVOD$) with VOD AMSRE_X.
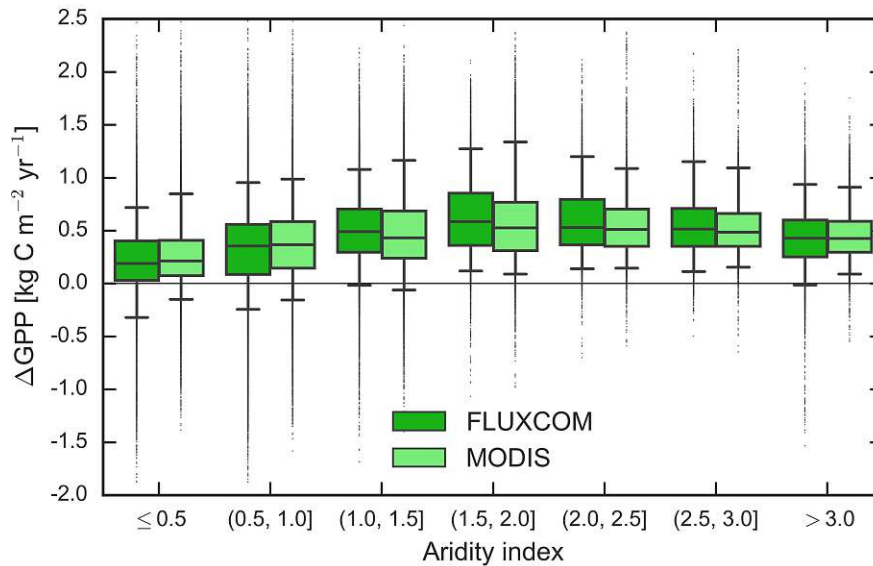
Figure 3.9: Differences in mean annual GPP between AMSRE_X and FLUXCOM or MODIS stratified along the aridity index. The analysis is based on the period 2007 to 2010 and uses 8-daily, 0.25° data. Mean annual GPP for AMSRE_X is computed using GPP(VOD, ΔVOD, $mdnVOD$). Box plot whiskers represent the 5th and 95th data percentile.

to the water potential of vegetation (Barnard et al., 2011; Brodribb and Holbrook, 2003; Momen et al., 2017). For this reason, VOD has also been used as a surrogate for fuel moisture in fire modelling (Forkel et al., 2017) or for leaf water potential and isohydricity of vegetation (Konings and Gentine, 2017; Konings et al., 2017a,b). The impact of the relative water content on the relationship between biomass and VOD, however, is not entirely clear. Using in situ estimates of leaf water potential, Momen et al. (2017) have shown that variations in VOD are largely driven by changes in leaf water potential or the interaction of leaf water potential and LAI rather than LAI alone. Nevertheless, studies connected leaf water potential to maximum stomatal conductivity (Klein, 2014; Running, 1976). Since stomatal conductivity controls photosynthesis by regulating the CO_2 uptake (e.g. Damour et al., 2010), this can provide an additional indication for the potential use of VOD to estimate GPP. Considering VOD as a proxy for leaf water potential, however, cannot explain the increase in temporal agreement when combining the original VOD signal and its derivative as observed in our study. Therefore, we propose that in our context VOD presents an estimate of the metabolically active biomass.

3.7.2 Impact of VOD frequency on the relationship with GPP

We observed that VOD data from X-band appear to be a suitable predictor for estimating GPP. This finding may be counter-intuitive since VOD from lower frequencies (i.e. longer wavelengths), such as L-band, rather than from higher frequencies was demonstrated to correlate closely with total aboveground vegetation biomass (Rodríguez-Fernández et al., 2018a). Total aboveground biomass, however, is a rather poor predictor of GPP due to the presence of large-size plant parts functioning as structural components that are less metabolically active (Litton et al., 2007). This is in accordance with observations of lower correlations between VOD and GPP for L-band than for C- or X-band VOD (Teubner et al., 2018). In contrast, the metabolically active plant parts, i.e. leaves and fine roots, present a suitable estimator for GPP (Litton et al., 2007). Since metabolically active cells contain water, the use of VOD in our model can present a suitable proxy for the aboveground metabolically

active parts, which in turn can be related to GPP. In addition to this, Litton et al. (2007) demonstrated that in forests the partitioning of carbon to leaves is a constant fraction of GPP. This implies that total GPP can be obtained by estimating the portion of GPP that goes into the leaf compartment. Those two concepts together with the theoretically stronger sensitivity of higher VOD frequencies to small vegetation parts, i.e. leaves and small structural components (Woodhouse, 2005), can explain why high frequency VOD rather than low frequency VOD is suited for retrieving GPP.

3.7.3 Extrapolation of VOD-GPP relationship

In both extrapolation experiments (temporal and spatial), we observed a lower agreement of VOD-based estimates with in situ GPP than with global GPP. In contrast, SIF only showed a slight reduction in performance during spatial extrapolation. This indicates that subpixel heterogeneity plays a more important role for the relationship between VOD and GPP than between SIF and GPP. From a mathematical point of view, the relationship between VOD and GPP strongly depends on the appropriate weighting of the two dynamic terms in the model, VOD and ΔVOD, in order to match the temporal dynamic of the reference GPP. Since variations in the weighting result in a temporal shifting of the VOD-based GPP estimate, weights that are not representative for the respective grid cell may decrease model performance. Therefore, scale differences potentially have a stronger impact on the upscaling of GPP with VOD than with SIF.

For the spatial extrapolation experiment, we further found that the offset in the VOD-GPP relationship varies between grid cells, unlike for the SIF-GPP relationship for which the offset is a global value. The reason for this may be linked to the contribution of structural components to VOD. VOD contains information both on woody and leaf parts (Tian et al., 2017). For estimating total GPP, however, the relevant aboveground information are mainly the leaves (Litton et al., 2007). Larger plant parts, which also contribute to the VOD signal, exhibit lower metabolic activity than leaves (Litton et al., 2007). Adding $mdnVOD$ as input to GAM thus seems to ensure that structural components within the grid cells are subtracted, thereby making the remainder more closely related to the leaves. When considering longer periods, the static $mdnVOD$ should thus be replaced with a metric that varies over time in order to reflect changes in land cover.

The extrapolation experiments overall indicated that further input variables may be needed to enhance the model's extrapolation capability. Including land cover information, which is commonly used in upscaling of in situ GPP (Chen et al., 2010; Jung et al., 2009; Tramontana et al., 2015, 2016), may help reduce the impact of scale differences. A second variable, which may improve extrapolation, is the fraction of C3, C4 and CAM plants within a grid cell. These plants employ different strategies for carbon uptake and, hence, have a different efficiency in photosynthesis (e.g. Bonan, 2015). In turn, this may alter the VOD-GPP relationship.

3.7.4 Performance of GPP upscaling

The VOD-based upscaling of GPP generally compared well with GPP from FLUXCOM and MODIS. Some areas exhibit inverse temporal dynamics with GPP. This, however, is not an issue of the model formulation but of the VOD observations itself. Microwave VOD observations can exhibit an inverse relationship to optical vegetation parameters in wet regions for passive VOD and in dry regions for active VOD (Jones et al., 2011; Liu et al., 2011; Vreugdenhil et al., 2017). Without explicitly accounting for this behavior, these patterns of negative correlations are propagated through to the VOD-based

GPP estimates.

Considering annual GPP, we observed a closer agreement with GPP from FLUXCOM and MODIS for X-band VOD from AMSR2 than from AMSR-E. On the one hand, this finding may be linked to differences between the sensors themselves. Du et al. (2017) reported that small differences between the performance for AMSR-E and AMSR2 exist. In line with this, we observed lower RMSE for AMSR2 than for AMSR-E during cross validation. On the other hand, the differences between AMSR-E and AMSR2 could also be caused by the different analysis periods. Considering that the temporal coverage of FLUXNET stations varies for AMSR-E and for AMSR2, this likely has the same effect as seen for the uncertainty analysis, because stations used for upscaling AMSR-E were not necessarily present in the period for AMSR2, and vice versa. The reason for these differences still requires further investigation.

Apart from methodological differences between the VOD-based GPP estimation and GPP from FLUXCOM or MODIS, further variations may arise from differences in the setup. FLUXCOM and MODIS GPP products both have a higher spatial resolution than VOD data, which potentially reduces the impact of scale differences. The FLUXNET data set used for the upscaling in FLUXCOM also differs in the data period and incorporates a larger number of sites (Tramontana et al., 2016). As shown for the uncertainty analysis, the choice of FLUXNET stations has an impact on the VOD-based upscaling and, thus, likely contributes to observed differences between VOD-based GPP and FLUXCOM GPP. In addition, FLUXCOM and MODIS incorporate ancillary information on land cover (Running et al., 1999; Tramontana et al., 2016), which was already discussed in Section 3.7.3 as possibility for model improvement.

3.7.5 Impact of model simplifications

The framework neglects the temperature dependency of R_a, which is often represented as an exponential increase of R_a with temperature (Wythers et al., 2013; Vanderwel et al., 2015; Tjoelker et al., 2001; Smith and Dukes, 2013; Atkin et al., 2005; Atkin and Tjoelker, 2003). Not accounting for this effect thus may explain the observed overestimation of the VOD-based GPP estimates. The comparison of estimates from AMSR-E and AMSR2, however, showed a closer agreement with FLUXCOM and MODIS for AMSR2 than for AMSR-E even without including temperature in the model. This indicates that, in addition to the temperature dependency of R_a, other effects play an important role, which need to be considered for a more robust estimation of GPP based on VOD. These parameters likely include the choice of training data as demonstrated by the variability in mean annual GPP during the uncertainty analysis.

Another simplification is that our model assumes similar temporal dynamics of above- and belowground biomass, which allows expressing biomass as function of VOD. The ratio of above- and belowground growth, however, may vary between years in response to environmental stresses like droughts, as shown by Doughty et al. (2015a) for forest plots in the Amazon basin. Depending on the strength of this effect, mismatches in above- and belowground dynamics can potentially lead to differences between the VOD-based upscaling of GPP and GPP retrieved from optical data.

In general, differences and temporal shifts between GPP derived from microwave and optical data can point towards additional terms of carbon loss or storage that were not considered in the simplified model formulation. A study conducted by Würth et al. (2005) demonstrated for a semi-deciduous tropical forest how seasonal variations in the concentration of non-structural carbohydrates can support temporal shifts between carbon assimilation and vegetation growth. Therefore, differences

between source- and sink-driven GPP can potentially give further insight into large-scale patterns of
carbon partitioning or allocation.

3.8 Conclusion

We have proposed a model for estimating GPP globally based on single frequency microwave satellite
VOD. The approach uses VOD as proxy for aboveground living biomass and describes the relationship
between VOD and GPP through a differential equation, which connects VOD and its derivative. Using
temporal changes in consecutive VOD observations (ΔVOD) as approximation for the derivative, we
implemented the model using Generalized Additive Models. The proposed model is driven by VOD-
based observations of vegetation biomass, and thus presents a sink-driven approach. Our results show
that the model performs well in temporal extrapolation but requires further input variables like the
grid cell median VOD for spatial extrapolation of the VOD-GPP relationship. We have attributed
this behavior to varying proportions of structural components captured by the VOD signal, which
contribute less to the GPP estimation and may be reduced by including median VOD. Our approach
tends to overestimate GPP with respect to FLUXCOM and MODIS GPP, which is probably caused
by the lack of temperature dependency of autotrophic respiration in the current model formulation.
Overall, our results demonstrate the global applicability of the model and highlight the potential use
of microwave VOD for providing GPP estimates that are complementary to source-driven approaches
based on optical remote sensing data.

3.9 Acknowledgements

Appendix

3.A   Supplement

Figure 3.A.1: Temporal median maps for VOD (a-h), SIF (j) and GPP (i, k) data sets.

Table 3.A.1: Overview of FLUXNET sites in the FLUXNET2015 Tier 1 data set.

53

ID	FLUXNET-ID	Name	Lon [°E]	Lat [°N]	Period used
1	AR-SLu	San Luis	-66.46	-33.46	2009-2011
2	AR-Vir	Virasoro	-56.19	-28.24	2010-2012
3	AT-Neu	Neustift	11.32	47.12	2007-2012
4	AU-ASM	Alice Springs	133.25	-22.28	2010-2013
5	AU-Ade	Adelaide River	131.12	-13.08	2007-2009
6	AU-Cpr	Calperum	140.59	-34.00	2010-2013
7	AU-Cum	Cumberland Plains	150.72	-33.61	2012-2013
8	AU-DaP	Daly River Savanna	131.32	-14.06	2008-2013
9	AU-DaS	Daly River Cleared	131.39	-14.16	2008-2013
10	AU-Dry	Dry River	132.37	-15.26	2008-2013
11	AU-Emr	Emerald, Queensland, Australia	148.47	-23.86	2011-2013
12	AU-Fog	Fogg Dam	131.31	-12.55	2007-2008
13	AU-GWW	Great Western Woodlands, Western Australia, Australia	120.65	-30.19	2013-2014
14	AU-RDF	Red Dirt Melon Farm, Northern Territory	132.48	-14.56	2011-2013
15	AU-Rig	Riggs Creek	145.58	-36.65	2011-2013
16	AU-Rob	Robson Creek, Queensland, Australia	145.63	-17.12	2014-2014
17	AU-Tum	Tumbarumba	148.15	-35.66	2007-2013
18	AU-Whr	Whroo	145.03	-36.67	2011-2013
19	BE-Bra	Brasschaat	4.52	51.31	2007-2013
20	BE-Lon	Lonzee	4.75	50.55	2007-2014
21	BE-Vie	Vielsalm	6.00	50.31	2007-2014
22	CA-Qfo	Quebec - Eastern Boreal, Mature Black Spruce	-74.34	49.69	2007-2010
23	CH-Cha	Chamau	8.41	47.21	2007-2012
24	CH-Fru	Früebüel	8.54	47.12	2007-2012
25	CH-Oe1	Oensingen grassland	7.73	47.29	2007-2008
26	CN-Cng	Changling	123.51	44.59	2007-2010
27	CN-Du2	Duolun_grassland (D01)	116.28	42.05	2007-2008
28	CN-Sw2	Siziwang Grazed (SZWG)	111.90	41.79	2010-2012
29	CZ-BK1	Bily Kriz forest	18.54	49.50	2007-2008
30	DE-Akm	Anklam	13.68	53.87	2009-2014
31	DE-Gri	Grillenburg	13.51	50.95	2007-2014
32	DE-Hai	Hainich	10.45	51.08	2007-2012
33	DE-Kli	Klingenberg	13.52	50.89	2007-2014
34	DE-Lkb	Lackenberg	13.30	49.10	2009-2013
35	DE-Obe	Oberbärenburg	13.72	50.78	2008-2014
36	DE-RuS	Selhausen Juelich	6.45	50.87	2011-2014
37	DE-Spw	Spreewald	14.03	51.89	2010-2014
38	DE-Tha	Tharandt	13.57	50.96	2007-2014
39	DK-NuF	Nuuk Fen	-51.39	64.13	2008-2014
40	DK-Sor	Soroe	11.64	55.49	2007-2012
41	DK-ZaH	Zackenberg Heath	-20.55	74.47	2007-2008
42	ES-LgS	Laguna Seca	-2.97	37.10	2007-2009
43	ES-Ln2	Lanjaron-Salvage logging	-3.48	36.97	2009-2009
44	FI-Hyy	Hyytiala	24.30	61.85	2007-2014
45	FR-Gri	Grignon	1.95	48.84	2007-2013
46	FR-Pue	Puechabon	3.60	43.74	2007-2013
47	GF-Guy	Guyaflux (French Guiana)	-52.92	5.28	2007-2012
48	IT-CA1	Castel d'Asso 1	12.03	42.38	2011-2013
49	IT-CA2	Castel d'Asso 2	12.03	42.38	2011-2013

continued from previous page

ID	FLUXNET-ID	Name	Lon [°E]	Lat [°N]	Period used
50	IT-CA3	Castel d'Asso 3	12.02	42.38	2011-2013
51	IT-Cp2	Castelporziano 2	12.36	41.70	2012-2013
52	IT-Isp	Ispra ABC-IS	8.63	45.81	2013-2014
53	IT-Lav	Lavarone	11.28	45.96	2007-2012
54	IT-Noe	Arca di Noé - Le Prigionette	8.15	40.61	2007-2012
55	IT-Ren	Renon	11.43	46.59	2007-2013
56	IT-Ro1	Roccarespampani 1	11.93	42.41	2007-2008
57	IT-Ro2	Roccarespampani 2	11.92	42.39	2007-2012
58	IT-SR2	San Rossore 2	10.29	43.73	2013-2014
59	IT-SRo	San Rossore	10.28	43.73	2007-2012
60	IT-Tor	Torgnon	7.58	45.84	2008-2013
61	NL-Hor	Horstermeer	5.07	52.24	2007-2011
62	NL-Loo	Loobos	5.74	52.17	2007-2013
63	NO-Adv	Adventdalen	15.92	78.19	2012-2014
64	RU-Cok	Chokurdakh	147.49	70.83	2007-2013
65	RU-Fyo	Fyodorovskoye	32.92	56.46	2007-2013
66	SD-Dem	Demokeya	30.48	13.28	2007-2009
67	US-AR1	ARM USDA UNL OSU Woodward Switchgrass 1	-99.42	36.43	2009-2012
68	US-AR2	ARM USDA UNL OSU Woodward Switchgrass 2	-99.60	36.64	2009-2012
69	US-ARM	ARM Southern Great Plains site- Lamont	-97.49	36.61	2007-2012
70	US-Blo	Blodgett Forest	-120.63	38.90	2007-2007
71	US-Ha1	Harvard Forest EMS Tower (HFR1)	-72.17	42.54	2007-2012
72	US-Los	Lost Creek	-89.98	46.08	2007-2014
73	US-MMS	Morgan Monroe State Forest	-86.41	39.32	2007-2014
74	US-Me6	Metolius Young Pine Burn	-121.61	44.32	2010-2012
75	US-Myb	Mayberry Wetland	-121.77	38.05	2011-2014
76	US-Ne1	Mead - irrigated continuous maize site	-96.48	41.17	2007-2013
77	US-Ne2	Mead - irrigated maize-soybean rotation site	-96.47	41.16	2007-2013
78	US-Ne3	Mead - rainfed maize-soybean rotation site	-96.44	41.18	2007-2013
79	US-SRM	Santa Rita Mesquite	-110.87	31.82	2007-2014
80	US-Syv	Sylvania Wilderness Area	-89.35	46.24	2007-2014
81	US-Ton	Tonzi Ranch	-120.97	38.43	2007-2014
82	US-Tw3	Twitchell Alfalfa	-121.65	38.12	2013-2014
83	US-UMd	UMBS Disturbance	-84.70	45.56	2007-2014
84	US-Var	Vaira Ranch- Ione	-120.95	38.41	2007-2014
85	US-WCr	Willow Creek	-90.08	45.81	2010-2014
86	US-Whs	Walnut Gulch Lucky Hills Shrub	-110.05	31.74	2007-2014
87	US-Wkg	Walnut Gulch Kendall Grasslands	-109.94	31.74	2007-2014
88	ZA-Kru	Skukuza	31.50	-25.02	2007-2010
89	ZM-Mon	Mongu	23.25	-15.44	2007-2009
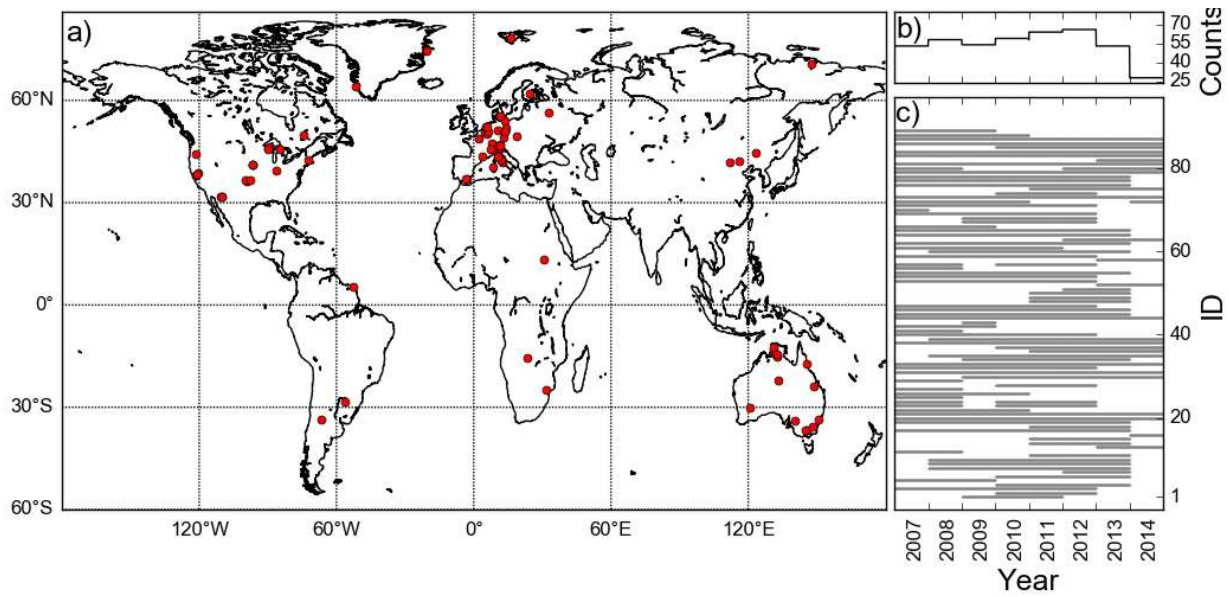
Figure 3.A.2: FLUXNET2015 Tier 1 data set: (a) location of FLUXNET sites, (b) sum of available observations per year and (c) temporal data coverage per site. The site IDs are shown in Table 3.A.1.

Table 3.A.2: Spearman rank correlation between FLUXCOM GPP and different GPP estimates developed per grid cell at 8-daily, 0.25° and monthly, 0.5° sampling. Models were trained against FLUXCOM using data from the years 2007 and 2008, and tested with data from the remaining period for each data set. Q25, Q50, and Q75 are the 25th, 50th and 75th percentile of significant correlations, respectively. sig (not_sig) stands for the fraction of significant (not significant) correlations with respect to all possible land grid cells at each resolution.

Data set	Model setup	monthly, 0.5°					8-daily, 0.25°				
		Q25	Q50	Q75	sig	not_sig	Q25	Q50	Q75	sig	not_sig
SIF	GPP(SIF)	0.54	0.73	0.85	0.77	0.20					
AMSRE_C	GPP(VOD, ΔVOD)	0.67	0.80	0.89	0.62	0.23	0.52	0.69	0.81	0.70	0.14
	GPP(VOD)	0.55	0.68	0.79	0.49	0.37	0.40	0.55	0.69	0.60	0.25
	GPP(ΔVOD)	0.54	0.67	0.79	0.51	0.35	0.37	0.51	0.63	0.61	0.23
AMSRE_X	GPP(VOD, ΔVOD)	0.69	0.82	0.90	0.67	0.20	0.55	0.72	0.83	0.76	0.12
	GPP(VOD)	0.56	0.69	0.79	0.55	0.32	0.41	0.56	0.70	0.68	0.20
	GPP(ΔVOD)	0.55	0.69	0.79	0.55	0.32	0.38	0.51	0.64	0.66	0.22
AMSRE_Ku	GPP(VOD, ΔVOD)	0.68	0.81	0.89	0.67	0.20	0.52	0.69	0.81	0.75	0.14
	GPP(VOD)	0.56	0.68	0.78	0.49	0.38	0.40	0.55	0.69	0.63	0.26
	GPP(ΔVOD)	0.55	0.68	0.79	0.59	0.29	0.37	0.49	0.61	0.66	0.23
AMSR2_C1	GPP(VOD, ΔVOD)	0.74	0.85	0.92	0.55	0.33	0.56	0.72	0.83	0.66	0.22
	GPP(VOD)	0.61	0.74	0.85	0.36	0.51	0.44	0.58	0.72	0.50	0.38
	GPP(ΔVOD)	0.64	0.78	0.88	0.43	0.44	0.43	0.58	0.71	0.57	0.31
AMSR2_C2	GPP(VOD, ΔVOD)	0.73	0.84	0.91	0.51	0.36	0.53	0.69	0.81	0.63	0.25
	GPP(VOD)	0.60	0.73	0.85	0.34	0.54	0.43	0.56	0.70	0.46	0.42
	GPP(ΔVOD)	0.63	0.76	0.88	0.41	0.47	0.42	0.56	0.70	0.55	0.33
AMSR2_X	GPP(VOD, ΔVOD)	0.76	0.86	0.93	0.59	0.30	0.57	0.73	0.84	0.71	0.19
	GPP(VOD)	0.63	0.75	0.86	0.40	0.49	0.46	0.59	0.72	0.55	0.35
	GPP(ΔVOD)	0.65	0.79	0.89	0.46	0.43	0.44	0.58	0.71	0.59	0.31
AMSR2_Ku	GPP(VOD, ΔVOD)	0.74	0.85	0.92	0.57	0.32	0.54	0.70	0.82	0.67	0.23
	GPP(VOD)	0.61	0.74	0.85	0.38	0.50	0.44	0.58	0.72	0.53	0.37
	GPP(ΔVOD)	0.63	0.76	0.87	0.43	0.45	0.41	0.54	0.67	0.55	0.35
ASCAT	GPP(VOD, ΔVOD)	0.57	0.74	0.84	0.82	0.13	0.42	0.61	0.74	0.85	0.11
	GPP(VOD)	0.48	0.64	0.76	0.74	0.22	0.34	0.52	0.67	0.80	0.16
	GPP(ΔVOD)	0.44	0.59	0.71	0.70	0.25	0.26	0.40	0.52	0.72	0.24

56
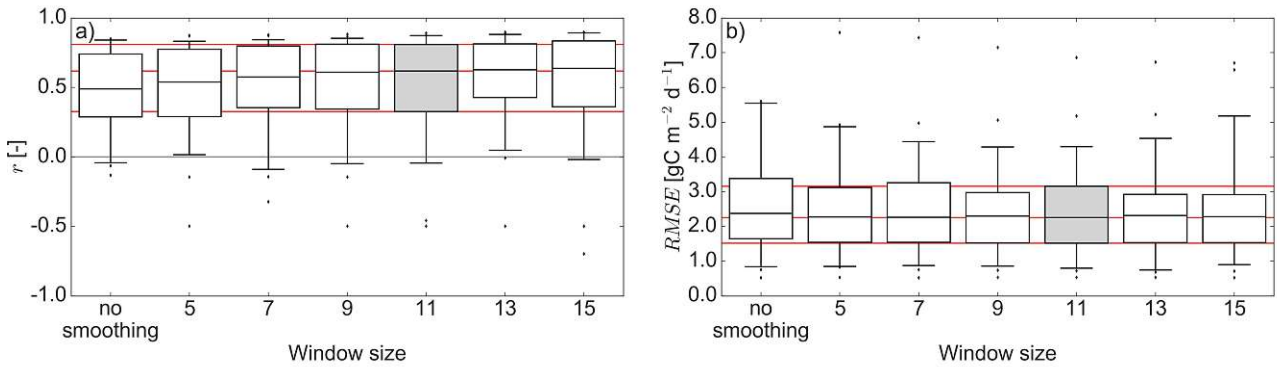
Figure 3.A.3: Analysis of window size: a) Spearman rank correlation (r) and b) root mean square error ($RMSE$) for AMSRE_X at 8-daily, 0.25° sampling using different window sizes between 5 to 15 time steps for the smoothing during the calculation of ΔVOD. The model setup is similar to the temporal extrapolation experiment and uses VOD and ΔVOD as input. Results for the window size 11 are highlighted in grey. For comparison, the 25th, 50th and 75th percentile of the box plot for the window size 11 are displayed as red lines.
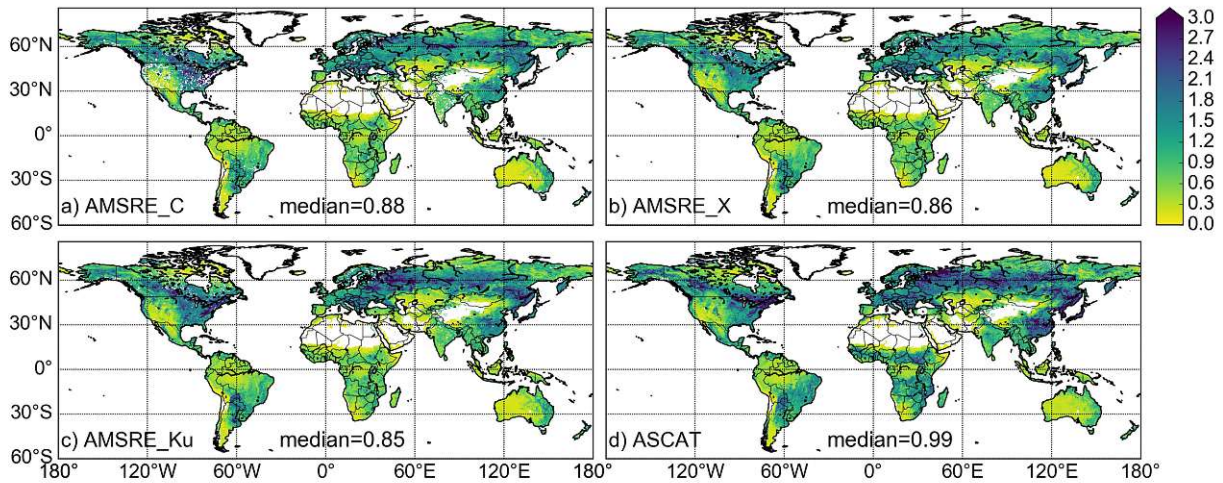
Figure 3.A.4: Root mean square error ($RMSE$, $gCm^{-2}d^{-1}$) between FLUXCOM GPP and GPP(VOD, ΔVOD) for different VOD data sets for the testing period (AMSR-E: 1/2009 to 9/2011; ASCAT: 1/2009 to 12/2015). The analysis is based on data at 8-daily, 0.25° sampling and uses data from the period 1/2007 and 12/2008 for training GPP(VOD, ΔVOD) against FLUXCOM at each grid cell separately. The median of $RMSE$ is displayed for each data set.
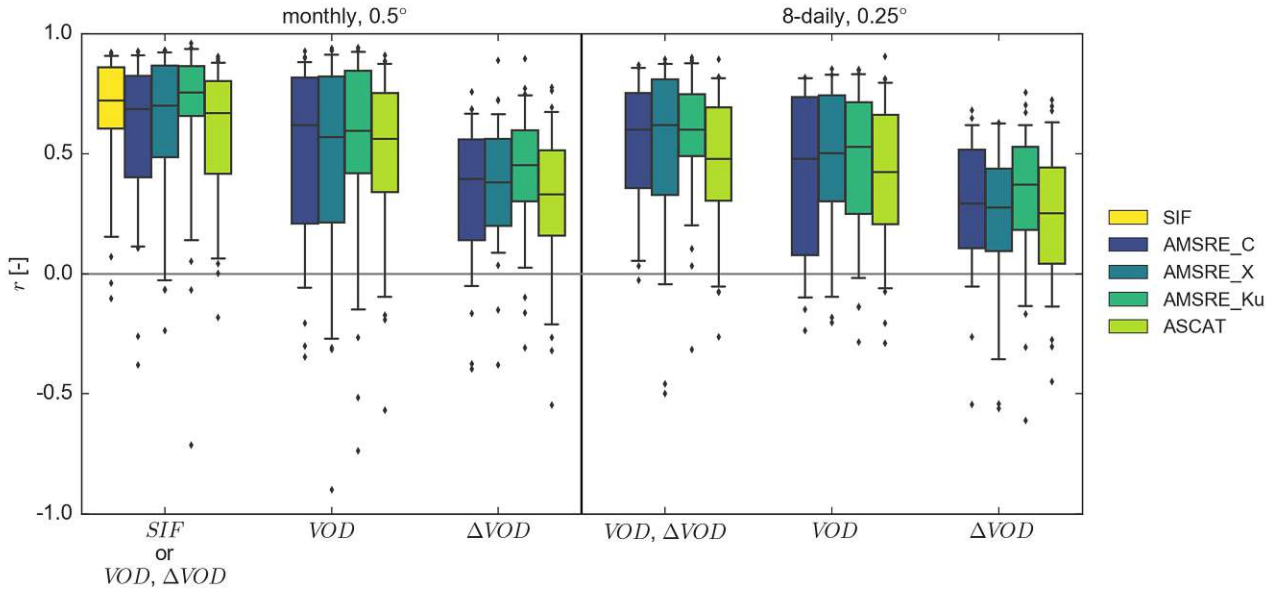
Figure 3.A.5: Site-specific evaluation of temporal extrapolation using Spearman rank correlation (r) between the full signal of in situ FLUXNET GPP and GPP estimates based on VOD or SIF. Models were trained using data from the years 2007 to 2008 and tested during the remaining period. Input variables are SIF, VOD, ΔVOD or the combination of VOD and ΔVOD as indicated on the x-axis. Box plot whiskers extend to the 5th and 95th data percentile.
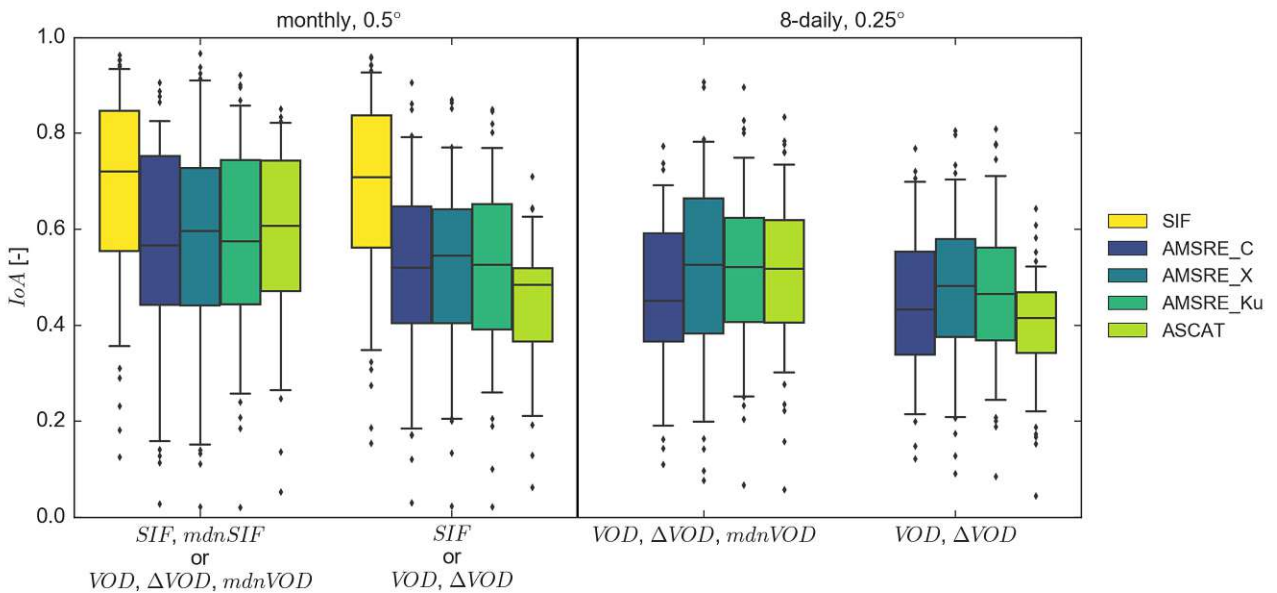
Figure 3.A.6: Leave-site-out cross validation for the index of agreement (IoA) at monthly, 0.5° and 8-daily, 0.25° sampling. The analysis is carried out for the full signals of in situ FLUXNET GPP and GPP estimates based on VOD or SIF. Labels on the x-axis indicate which input variables are used for each model. Box plot whiskers extend to the 5th and 95th data percentile. Abbreviations – $mdnSIF$: temporal grid cell median SIF; ΔVOD: temporal change in VOD between two consecutive observations; and $mdnVOD$: temporal grid cell median VOD.
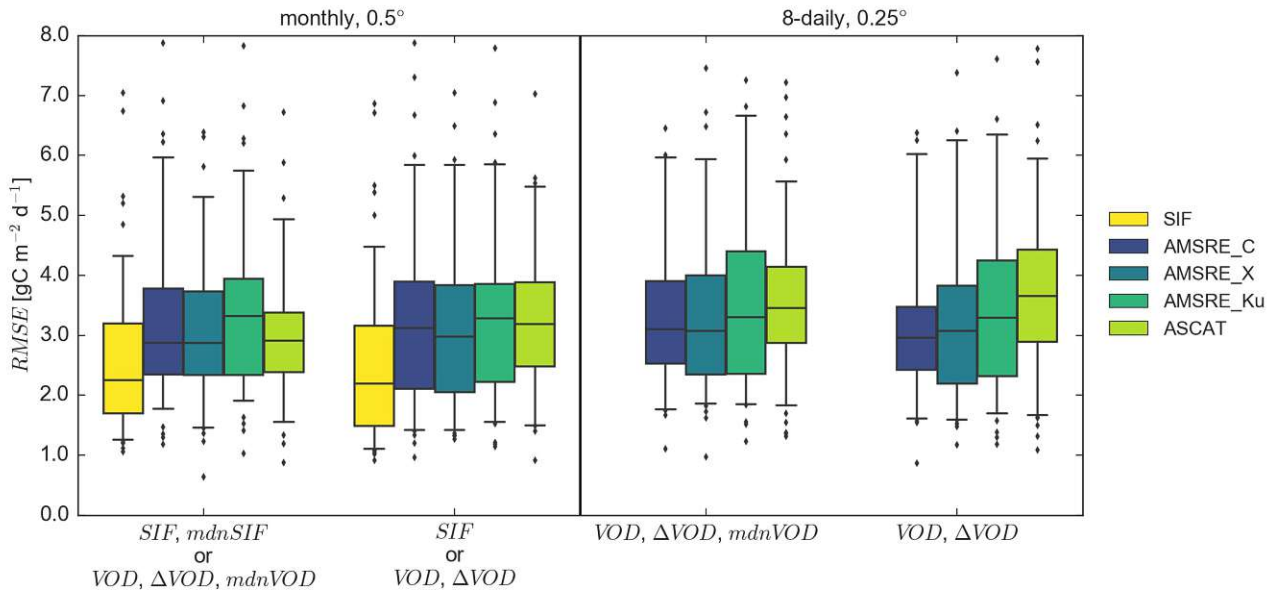
Figure 3.A.7: As Fig. 3.A.6 but for the root mean square error ($RMSE$).
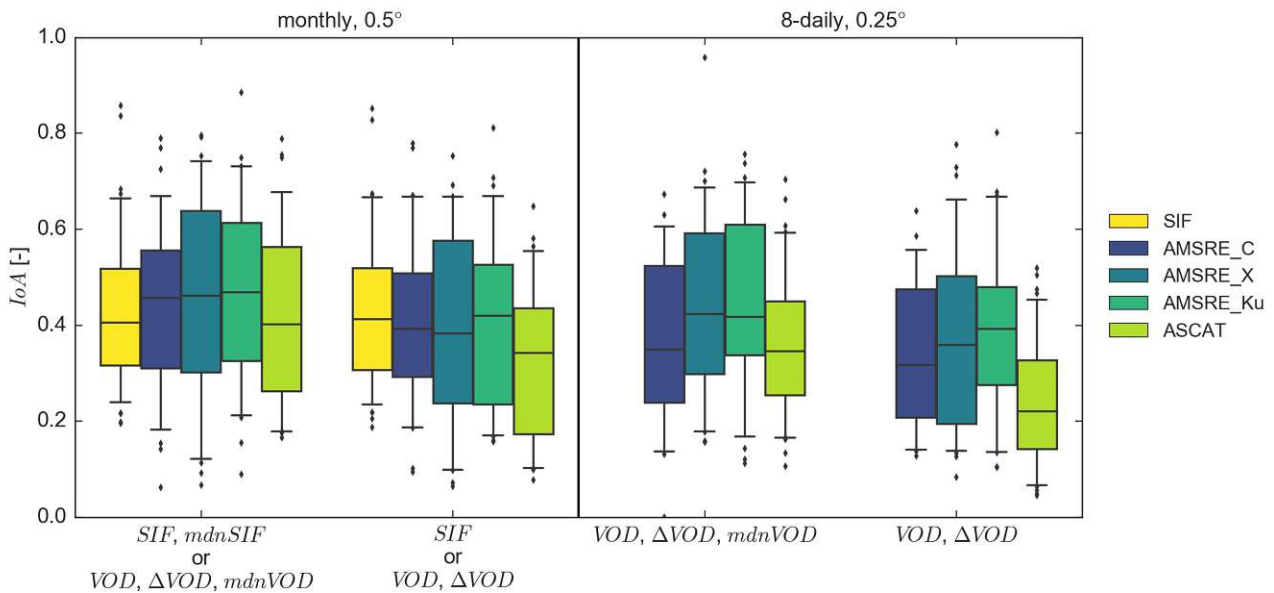
Figure 3.A.8: Leave-site-out cross validation for the index of agreement (IoA) at monthly, 0.5° and 8-daily, 0.25° sampling. The analysis is carried out for the anomalies of in situ FLUXNET GPP and GPP estimates based on VOD or SIF. Labels on the x-axis indicate which input variables are used for each model. Box plot whiskers extend to the 5th and 95th data percentile. Abbreviations as in Fig. 3.A.6.
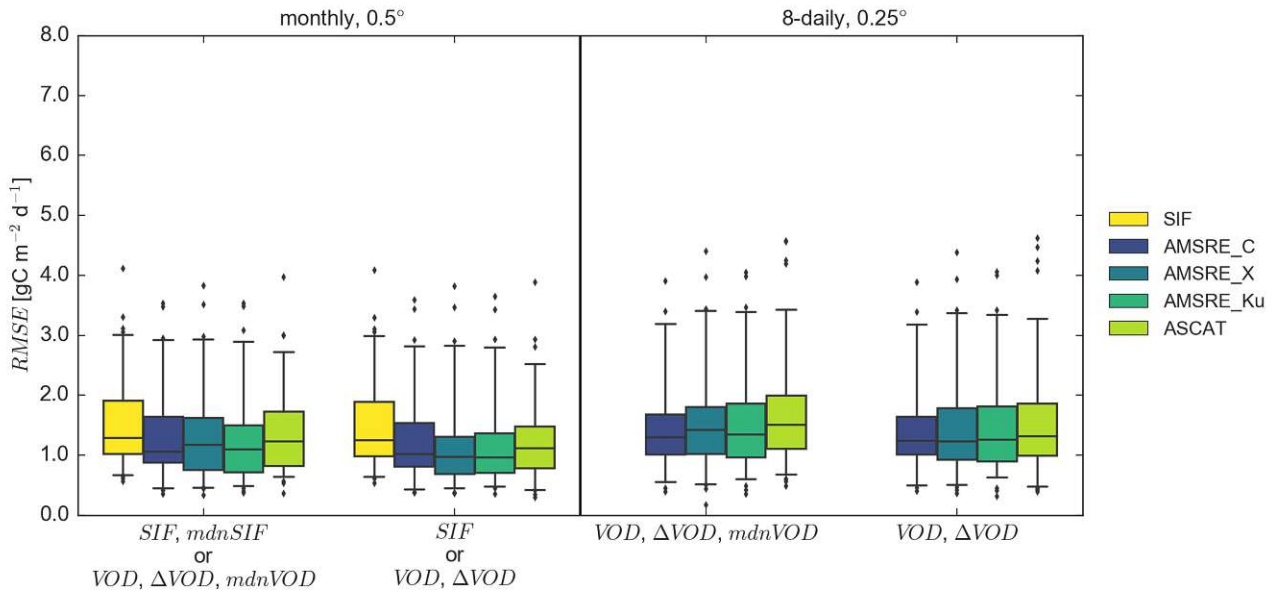
Figure 3.A.9: As Fig. 3.A.8 but for the root mean square error ($RMSE$).
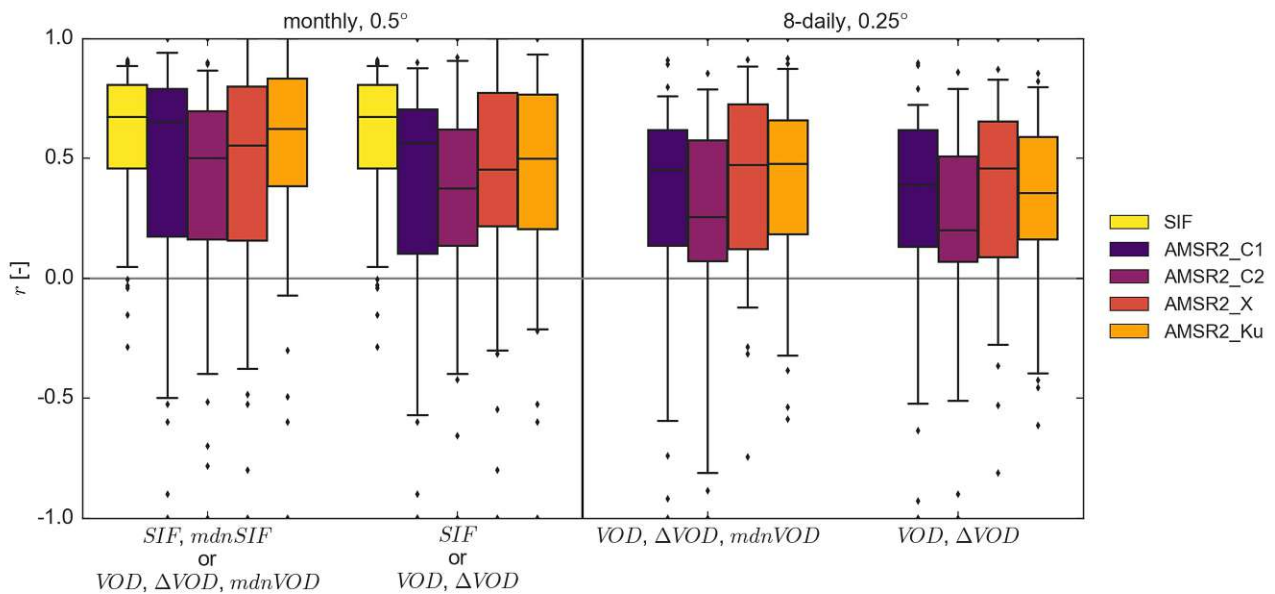
Figure 3.A.10: Leave-site-out cross validation for Spearman rank correlation (r). The analysis is performed for the full signals of in situ FLUXNET GPP and GPP estimates based on AMSR2 VOD or SIF. Labels on the x-axis indicate which input variables are used for each model. Box whiskers extend to the 5th and 95th data percentile. Abbreviations as in Fig. 3.A.6.
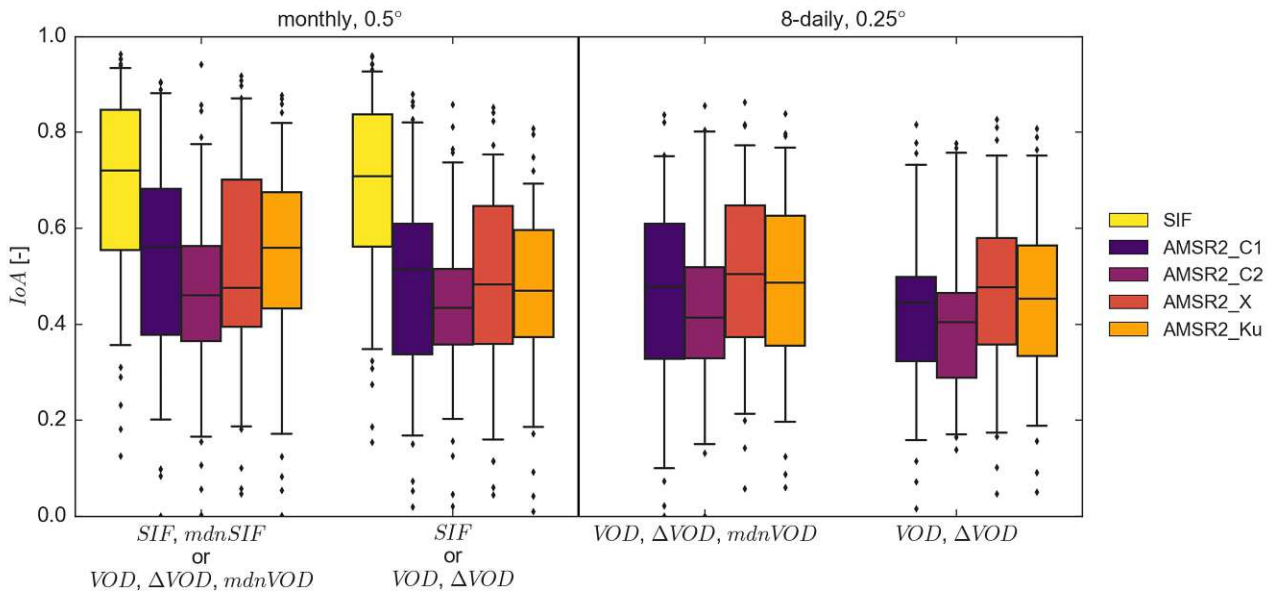
Figure 3.A.11: As Fig. 3.A.10 but for the index of agreement (IoA).
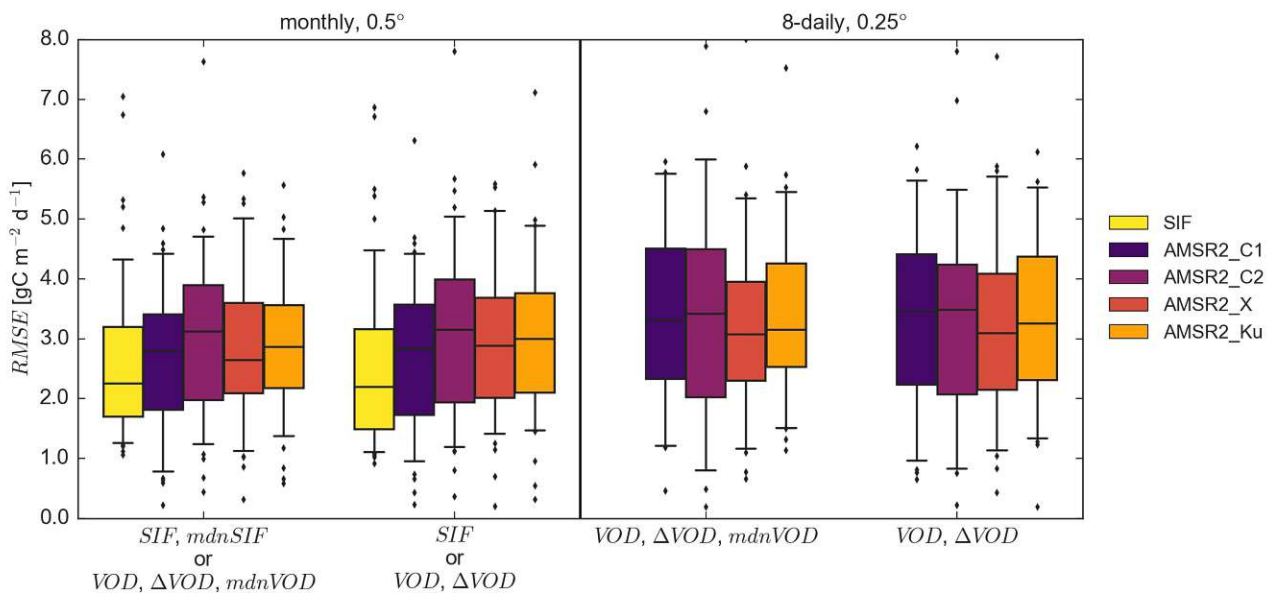
Figure 3.A.12: As Fig. 3.A.10 but for the root mean square error ($RMSE$).
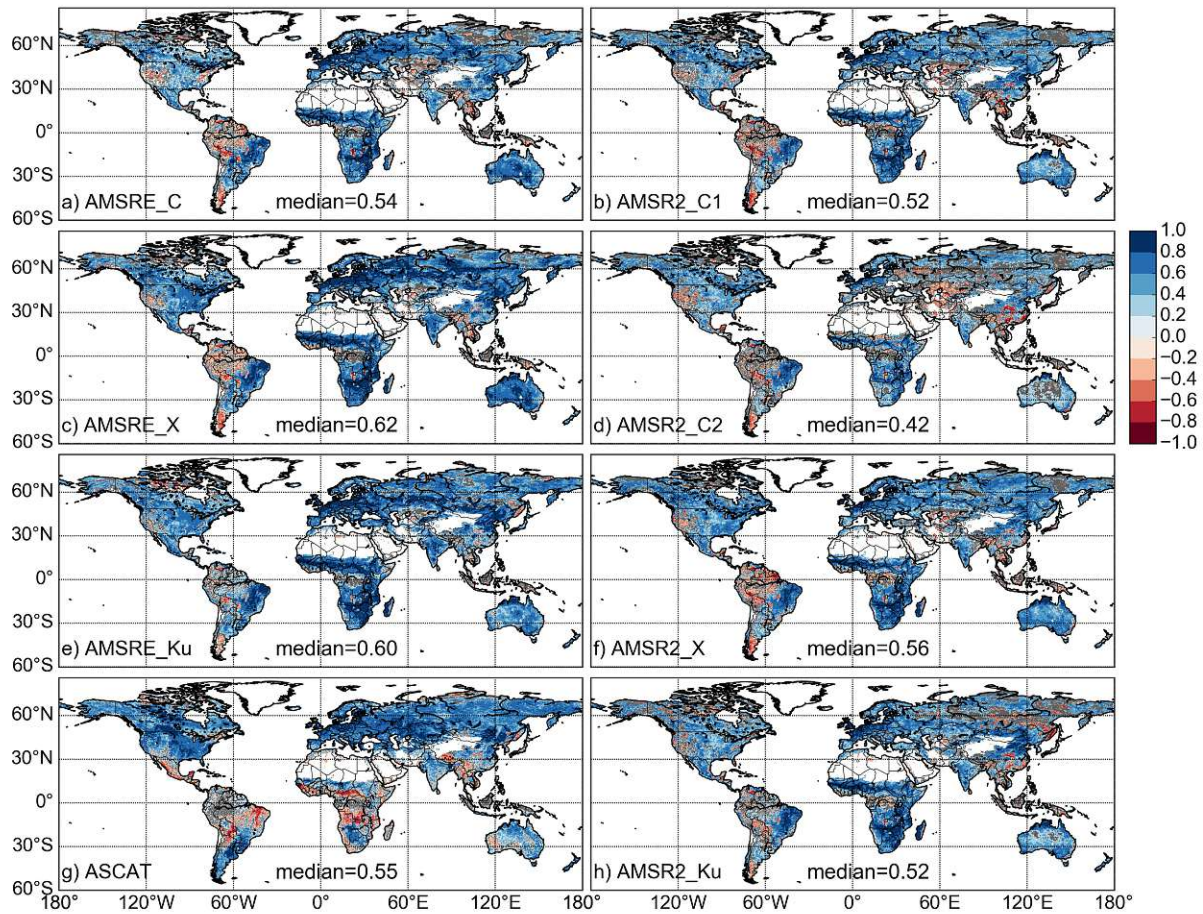
Figure 3.A.13: Spatial map of Spearman rank correlation between the upscaled GPP(VOD, ΔVOD, $mdnVOD$) and FLUXCOM GPP at 8-daily, 0.25° sampling. GPP(VOD, ΔVOD, $mdnVOD$) is trained against in situ FLUXNET GPP estimates. Correlations that are not significant are masked in grey. For each data set, the median of significant correlations is displayed.
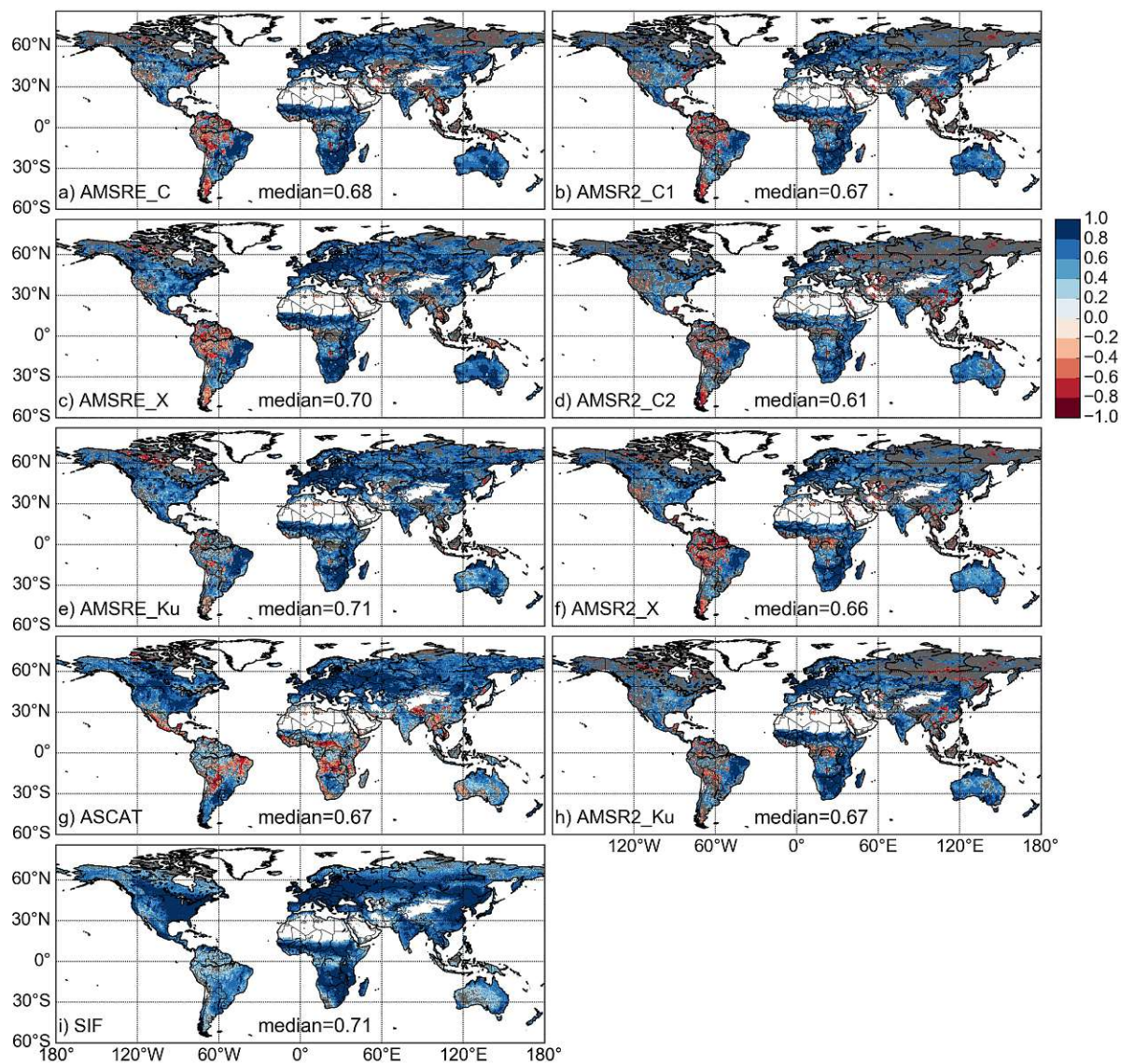
Figure 3.A.14: As Fig. 3.A.13 but for data at monthly, 0.5° sampling.
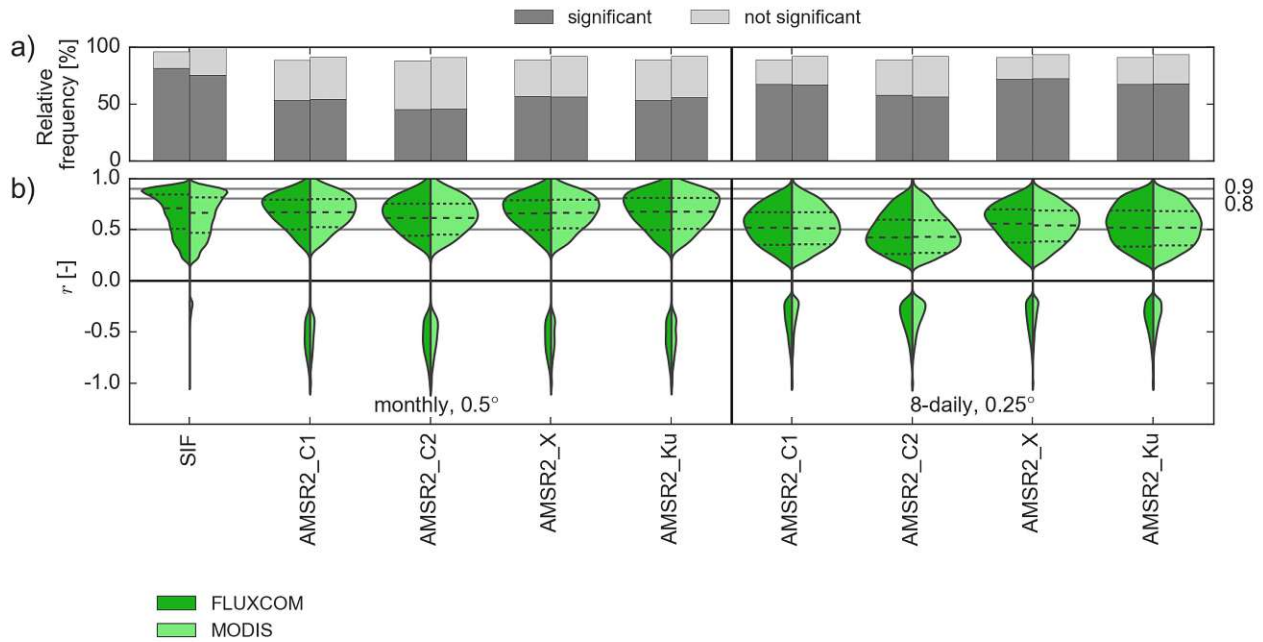
Figure 3.A.15: Spearman rank correlation (r) between GPP data sets (FLUXCOM, MODIS) and upscaling of GPP(VOD, ΔVOD, $mdnVOD$) for AMSR2 VOD data sets or GPP(SIF). Data were trained against in situ GPP estimates (FLUXNET) at 8-daily, 0.25° or monthly, 0.5° sampling. a) Relative frequency of grid cells with significant and not significant correlation with respect to all possible land grid cells at each resolution. Areas that do not contain results relate to gaps obtained during masking or to not produced pixels in the original data products. b) Violin plot of significant correlations. Horizontal grey lines indicate correlation values of 0.5, 0.8 and 0.9. Dashed lines denote the median (long dashes) and the 25th and 75th percentile (short dashes).
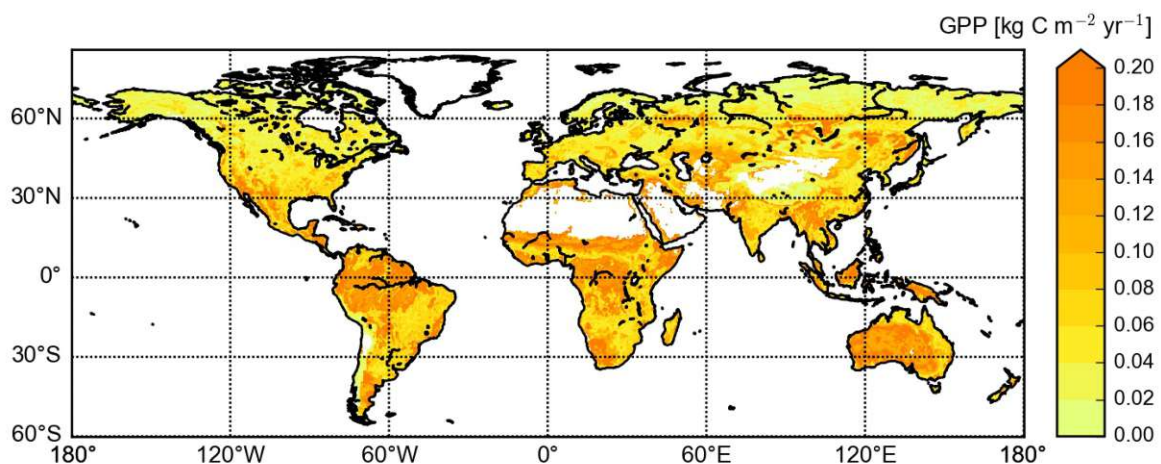
Figure 3.A.16: Standard deviation of mean annual GPP for ten model runs obtained during the uncertainty analysis of GPP(VOD, ΔVOD, $mdnVOD$) for VOD AMSRE_X. The models for each run were trained with data from 90% of the stations that were randomly drawn. The analysis is based on the period 2012 to 2015 and uses data at 8-daily, 0.25° sampling.
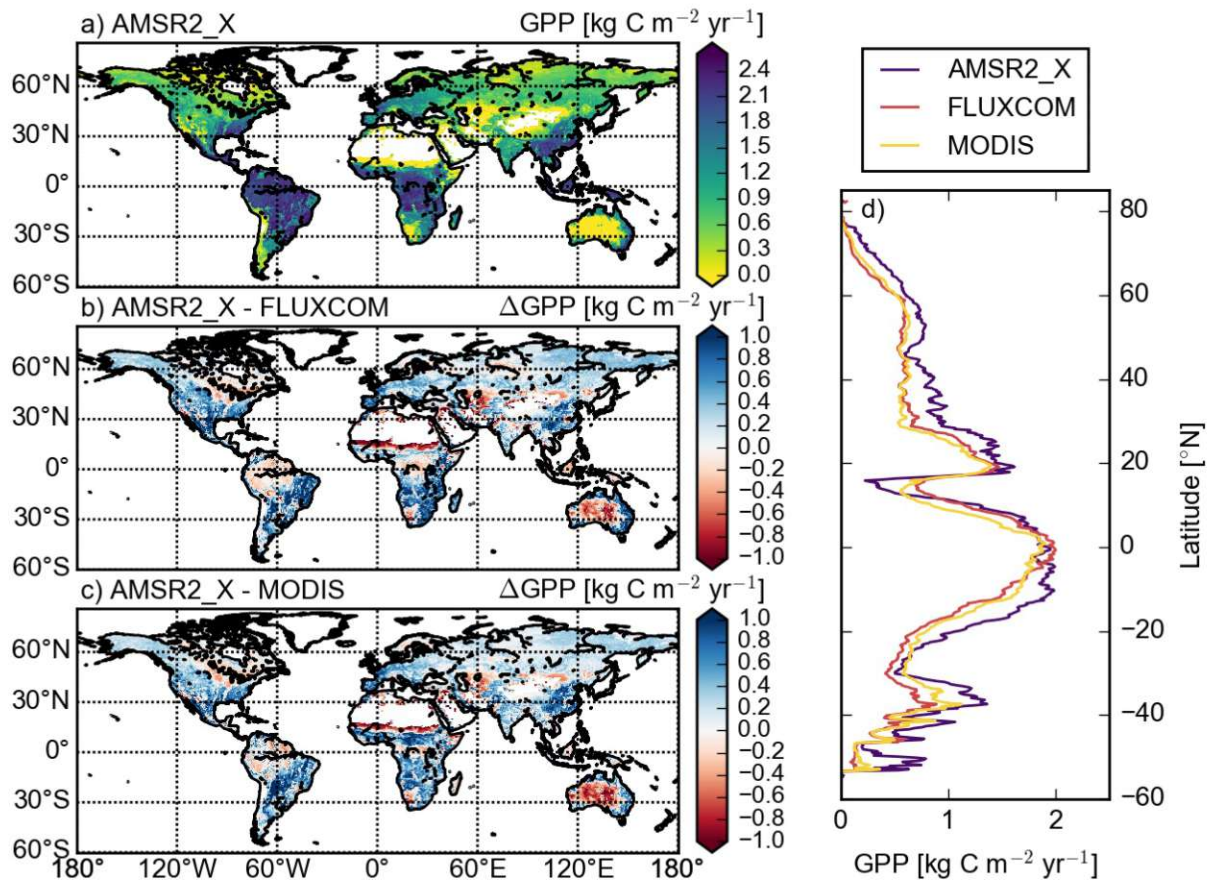
Figure 3.A.17: Mean annual GPP for the period 2012 to 2015: a) upscaling of GPP(VOD, ΔVOD, $mdnVOD$) for VOD AMSR2_X, b) difference in mean annual GPP between FLUXCOM and AMSR2_X c) difference in mean annual GPP between MODIS and AMSR2_X. Values in b) and c) are displayed between -1 and 1. d) Zonal mean of mean annual GPP. Estimates for GPP(VOD, ΔVOD, $mdnVOD$) were produced using data at 8-daily, 0.25° sampling.

Chapter 4

Impact of temperature and water availability on microwave-derived gross primary production

4.1 Abstract

Vegetation optical depth (VOD) from microwave satellite observations has received much attention in global vegetation studies in recent years due to its relationship to vegetation water content and biomass. We recently have shown that VOD is related to plant productivity, i.e. gross primary production (GPP). Based on this relationship between VOD and GPP we developed a theory-based machine learning model to estimate global patterns of GPP from passive microwave VOD retrievals. The VOD-GPP model generally showed good agreement with site observations and other global data sets in temporal dynamic but tended to overestimate annual GPP across all latitudes. We hypothesized that the reason for the overestimation is the missing effect of temperature on autotrophic respiration in the theory-based machine learning model. Here we aim to further assess and enhance the robustness of the VOD-GPP model by including the effect of temperature on autotrophic respiration within the machine learning approach and by assessing the interannual variability of the model results with respect to water availability. We used X-band VOD from the VOD Climate Archive (VODCA) data set for estimating GPP and used global state-of-the art GPP data sets from FLUXCOM and MODIS to assess residuals of the VOD-GPP model with respect to drought conditions as quantified by the Standardized Precipitation and Evaporation Index (SPEI).

Our results reveal an improvement in model performance for correlation when including the temperature dependency of autotrophic respiration (average correlation increase of 0.18). This improvement in temporal dynamic is larger for temperate and cold regions than for the tropics. For ubRMSE and bias, the results are regionally diverse and are compensated in the global average. Improvements are observed in temperate and cold regions while decreases in performance are obtained mainly in the tropics. The overall improvement when adding temperature was less than expected and thus may only partly explain previously observed differences between the global GPP datasets. On interannual time scales, estimates of the VOD-GPP model agree well with GPP from FLUXCOM and MODIS. We further find that the residuals between VOD-based GPP estimates and the other data sets do not significantly correlate with SPEI which demonstrates that the VOD-GPP model can capture responses of GPP to water availability even without including additional information on precipitation,

soil moisture or evapotranspiration. Exceptions from this rule were found in some regions: significant negative correlations between VOD-GPP residuals and SPEI were observed in the US corn belt, Argentina, Eastern Europe, Russia and China, while significant positive correlations were obtained in South America, Africa and Australia. In these regions, the significant correlations may indicate different plant strategies for dealing with variations in water availability.

Overall, our findings support the robustness of global microwave-derived estimates of gross primary production for large-scale studies on climate-vegetation interactions.

4.2 Introduction

Vegetation optical depth (VOD) from microwave satellite observations provides the opportunity for studying large-scale vegetation dynamics due to its sensitivity to the vegetation water content and above-ground biomass. Different studies have employed VOD for deriving various plant properties or vegetation characteristics that can be related to the plant's water content, including biomass estimation (Liu et al., 2015; Brandt et al., 2018; Rodríguez-Fernández et al., 2018b; Chaparro et al., 2019; Fan et al., 2019; Frappart et al., 2020; Wigneron et al., 2020; Li et al., 2021), crop yield (Chaparro et al., 2018), tree mortality (Rao et al., 2019; Sapes et al., 2019), analysis of burned area (Forkel et al., 2019), ecosystem-scale isohydricity (Konings and Gentine, 2017), plant water uptake during dry downs (Feldman et al., 2018) and plant water storage (Tian et al., 2018). VOD, or microwave satellite observations in general, are also analyzed for its potential in detecting the impact of drought (Song et al., 2019; Crocetti et al., 2020). Despite the sensitivity of VOD to vegetation water content, the relationship between VOD and GPP has not yet been analyzed with regard to how the relationship responds to varying conditions of dry- or wetness.

Recently, we have shown that VOD is related to plant productivity, i.e. gross primary production (GPP) (Teubner et al., 2018). Based on these findings, we developed a theory-guided machine learning model to estimate GPP from VOD (VOD-GPP model) and trained the model using eddy covariance estimates of GPP from the FLUXNET network (Teubner et al., 2019). The VOD-GPP model relies on estimating carbon sink terms, i.e. net primary production (NPP) and autotrophic respiration (Ra), based on VOD as a proxy for above-ground living biomass. The VOD-GPP model thus represents a carbon sink-driven approach. Since the VOD-GPP model uses biomass as main input, the estimation of GPP does not rely on input variables that are commonly used in source-driven approaches, e.g. absorption of photosynthetically active radiation as primary input term or vapor pressure deficit as controlling factor for stomatal conductance (Running et al., 2000; Turner et al., 2005; Goodrich et al., 2015; Zhang et al., 2016a, 2017). Although different studies are tackling the question of how much information on biomass is actually contained in the VOD signal (Momen et al., 2017; Vreugdenhil et al., 2018; Zhang et al., 2019), it might be worth noting that the water content can be seen as an important aspect in our model approach since it presents the living part of the vegetation and only living cells, which contain water, are able to respire. We have shown that the VOD-GPP model can well represent temporal dynamics of GPP but that it overestimates GPP especially in temperate and boreal regions (Teubner et al., 2019). We hypothesize that this overestimation may be caused by a missing representation of temperature dependency of autotrophic respiration in the VOD-GPP model.

Ra is the process through which chemical energy that was stored by building up carbohydrates during photosynthesis is gained by converting carbohydrates back into carbon dioxide. It is generally known that Ra is a temperature-dependent process (e.g., Atkin and Tjoelker, 2003). Modelling the

response of Ra to temperature, however, is complex due to the existence of thermal acclimation (Atkin
and Tjoelker, 2003). Ra is commonly represented through an exponential function with Q10 as base
which is multiplied with a basal respiration rate (e.g., Smith and Dukes, 2013). The base value Q10
describes how much Ra changes when temperature changes by 10°C (e.g., Atkin et al., 2008). Although
global models often use constant values for either one parameter or both parameters (Gifford, 2003;
Smith and Dukes, 2013), studies have shown that both basal respiration rate and Q10 may vary with
temperature (Tjoelker et al., 2001; Wythers et al., 2013). The implementation of such temperature
acclimation yields a functional representation that decreases again at higher temperatures and thus
takes into account that respiration may decrease outside an optimum temperature range (Smith and
Dukes, 2013).

Here we aim to assess the impact of the temperature dependency of Ra in the VOD-GPP model
and if it can improve model performance. Furthermore, we will test the plausibility of the model
by comparing the estimated interannual variability of GPP with independent state-of-the art global
data sets of GPP and by assessing model residuals with respect to variations in climatological water
availability as represented by the Standardized Precipitation and Evaporation Index (SPEI). Since
source- (GPP) and sink-terms (NPP + Ra) should theoretically be in balance, any differences between
the two approaches that are related to variations in water availability may give insight into different
plant strategies for dealing with dry or wet conditions and thus may be of interest for ecological or
plant-physiological studies at large-scale.

4.3   Data and methods

4.3.1   Choice of microwave frequency

The VOD-GPP model relies on biomass as input. Nevertheless, the choice of microwave frequency for
estimating GPP may look counterintuitive. On the one hand, VOD from low microwave frequencies
like L-band has been demonstrated to be better suited as proxy for mapping total above-ground
biomass than high frequency VOD, i.e. X-band VOD, as L-band VOD saturates less at high biomass
values (Chaparro et al., 2019; Frappart et al., 2020; Li et al., 2021). On the other hand, previous
analyses demonstrated that X-band VOD shows a closer agreement with GPP (Teubner et al., 2018,
2019; Kumar et al., 2020). In Figure 4.A.1 we further corroborated this observation by a correlation
analysis between in situ GPP and VOD from L- and X-band, respectively (for details about the single
sensor VOD datasets, see Teubner et al., 2018). Despite the high fraction (38%) of forest pixels used
for this computation, higher correlations were obtained for X-band than for L-band. An explanation
could be that whole plant biomass was found to be less suited for estimating GPP as opposed to
biomass of metabolically active plant parts like leaves and fine roots (Litton et al., 2007). Based on
these findings, we concluded that higher frequency VOD appears to be better suited for estimating
GPP and therefore we used X-band VOD in our analysis.

4.3.2   Data sets

We analyzed different GPP data sets derived from microwave and optical sensors as well as SPEI. As
input to the VOD-GPP model, we used X-band VOD data from the VOD Climate Archive (VODCA).
Since global coverage for VODCA X-band data starts in 2003 (Moesinger et al., 2020) and SPEI data
are available through 2015, we used the common period from 2003 to 2015 for our analysis. Temporal

median maps for the global GPP data sets are displayed in the supplement (Figure 4.A.2).

VODCA

VOD retrievals from single sensors often span only a certain period in time, which may hamper the analysis of longer periods. To overcome this problem, we used a merged single frequency VOD from the VOD Climate Archive (VODCA; Moesinger et al., 2020) as input to our model. VODCA (Moesinger et al., 2020) X-band (VODCAX) contains nighttime observations of passive VOD derived from TMI (10.7 GHz; variable overpass time), AMSR-E (10.7 GHz; descending 1:30 am), WindSat (10.7 GHz; descending 6:00 am) and AMSR2 (10.7 GHz; descending 1:30 am). The VOD input data are obtained from the Land Parameter Retrieval Model (LPRM; van der Schalie et al., 2017). The use of nighttime observations on the one hand meets the LPRM assumption of homogeneous temperature conditions (Owe et al., 2001) and on the other hand is better suited as proxy for plant water status than daytime observations. Due to diurnal differences in plant water status and the refilling during the night (El Hajj et al., 2019; Konings and Gentine, 2017), nighttime observations are closer to the predawn water potential which is commonly used as estimator for the daily vegetation water status (Konings and Gentine, 2017; Konings et al., 2019). During the processing of VODCAX, data are masked for radio frequency interference (RFI) (Moesinger et al., 2020) since RFI can introduce spurious retrievals (Li et al., 2004; Njoku et al., 2005). Data are available at daily resolution and 0.25° grid spacing.

Independent global GPP data sets

The MOD17A2H v006 product provides global estimates of GPP which are derived from surface reflectances (Running et al., 2004, 2015). The algorithm is based on the light-use efficiency concept by Monteith (1972) and uses the fraction of Photosynthetically Absorbed Radiation for deriving plant productivity (Running et al., 1999, 2000). Data are produced as 8-daily GPP estimates at 500 m resolution.

FLUXCOM presents an upscaling of GPP from eddy covariance measurements using an ensemble of machine learning approaches (Jung et al., 2020). The data set is available at 8-daily resolution and 10 km grid spacing. FLUXCOM estimates are produced in two setups: the FLUXCOM RS is based on remote sensing data as input to the machine learning models and the FLUXCOM RS+METEO uses meteorological data and only the mean seasonal cycle of remote sensing data (Jung et al., 2020). Since our approach is mainly based on remote sensing data, i.e. VOD observations, we used FLUXCOM RS in our analysis. The FLUXCOM algorithm uses the following MODIS variables as input: Enhanced Vegetation Index, Leaf Area Index, MODIS band 7 - Middle Infrared Reflectance, Normalized Difference Vegetation Index and Normalized Difference Water Index.

In situ GPP estimation from FLUXNET

The Fluxnet2015 data set (Pastorello et al., 2020) provides daily in situ estimates of carbon, water and heat fluxes, which are determined using the eddy covariance technique. GPP estimates are available for two flux partitioning methods, i.e. daytime and nighttime partitioning method. We used the mean of both partitioning methods, as suggested in (Pastorello et al., 2020), with variable friction velocity threshold (GPP_DT_VUT_REF, GPP_NT_VUT_REF) from the freely available station data set (Tier1 v1). Since data are available until 2014, we used data for the period from 2003 to 2014 as

training data for estimating GPP based on VOD. An overview of the FLUXNET sites is given in
Figure 4.A.3 and Table 4.A.1.

SPEI

For analyzing the impact of variations in water availability, we used SPEI from the SPEIbase (Beguería et al., 2017; Vicente-Serrano et al., 2010). The climatological water balance is calculated on
different time scales ranging from 1 up to 48 months. Since drought can act on different time scales,
we used SPEI at two different aggregations, 3- and 12-month, for investigating the response to dry
and wet conditions. The 3-month SPEI (SPEI03) represents short-term effects, while the 12-month
SPEI (SPEI12) relates to dry or wet conditions at annual time scale. Although SPEI cannot be used
to express actual water shortage for plants, it allows to indicate relative deviations from mean conditions. Because of the use of both precipitation and temperature, SPEI further enables the comparison
between different biomes (Vicente-Serrano et al., 2010). The SPEI data has monthly resolution and a
grid spacing of 0.5°.

ERA5-Land

ERA5-Land produced by the European Centre for Medium-Range Weather Forecasts (ECMWF) (C3S,
2019; Muñoz-Sabater, 2019) provides a reanalysis data set of meteorological parameters. ERA5 uses
a 4D variational data assimilation scheme and a Simplified Extended Kalman Filter (Hersbach et al.,
2020). We used skin temperature and snow data for masking VOD. In the VOD-GPP model, we
incorporated 2m air temperature ($T2M$) for representing the temperature dependency of autotrophic
respiration. $T2M$ was used in our analysis, since this parameter is most common for describing the
temperature dependency of autotrophic respiration for above-ground vegetation (e.g., Ryan et al.,
1997; Running et al., 2000; Ceschia et al., 2002; Drake et al., 2016). The data has hourly resolution
and 9 km spatial sampling.

4.3.3 Data processing

VODCAX data were masked for low temperature (skin temperature < 0°C) and snow cover (snow
depth > 0cm) and then aggregated to 8-daily estimates by computing the mean over 8 days to match
the temporal resolution of GPPmodis and GPPfluxcom. These 8-daily values were then used as input
to the VOD-GPP model and for further analysis throughout the study. GPPfluxcom and GPPmodis
were aggregated to 0.25° to match the spatial sampling of VODCAX. For the comparison with SPEI, 8-
daily GPP estimates were further resampled to monthly resolution while SPEI was spatially resampled
to 0.25° using the nearest neighbour method.

4.3.4 GPP estimation based on VOD

The approach of estimating GPP based on microwave radiation and the corresponding equations are
described in detail in Teubner et al. (2019). In short, the VOD-GPP model uses VOD as a proxy of
above-ground living biomass (Equation 4.1). It determines GPP by estimating sinks for carbohydrates,
i.e. the sum of NPP and Ra, which are represented through different VOD-derived variables: 1) time
series of the bulk VOD signal (VOD; 8-daily aggregated native VOD time series), 2) time series of the
temporal change in VOD (ΔVOD; $\Delta VOD_t = VOD_t - VOD_{t-1}$ computed from the smoothed 8-daily
aggregated VOD time series) and 3) the grid cell median of VOD ($mdnVOD$; calculated over the

entire VOD time series of the grid cell; used as a proxy for vegetation cover). While NPP is related to ΔVOD, Ra is related to both VOD and ΔVOD using the concept proposed by Ryan et al. (1997) of dividing Ra into maintenance and growth respiration (Equation 4.2). By assuming that belowground biomass terms are proportional to above-ground biomass (i.e. biomass B can be expressed through above ground biomass AGB) and by adding a static term c supporting the conversion in Equation 4.2, GPP can be represented through a differential equation with VOD as input (Equation 4.3).

$$\text{AGB} = f(VOD) = \widetilde{VOD} \tag{4.1}$$

$$\text{GPP} = \text{NPP} + \text{Ra} = \left(\frac{d\text{B}}{dt} + \text{loss terms} \right) + \left(a_0 \, \frac{d\text{B}}{dt} + b_0 \, \text{B} \right) \approx a \, \frac{d\text{B}}{dt} + b \, \text{B} \tag{4.2}$$

$$\text{GPP} = a \, \frac{\widetilde{dVOD}}{dt} + b \, \widetilde{VOD} + c \tag{4.3}$$

The formulation in GAM for this previous model, which uses only VOD variables as input (GP-Pvod; Equation 4.4), then reads:

$$\text{GPPvod} = s(VOD) + s(\Delta VOD) + s(mdnVOD) \tag{4.4}$$

where s denotes spline terms for representing the functions between each input variable and the response variable GPP in the 2-dimensional space.

For adding the temperature dependency of Ra, we are considering the two terms of Ra, i.e. maintenance and growth respiration. Since the temperature sensitivity mainly applies to the maintenance term (Ryan et al., 1997), we are only incorporating an interaction term with temperature for the maintenance part of the model formulation. Although all terms potentially may be dependent on temperature due to the general temperature dependency of enzymatic activity, the temperature dependency for modelling growth related sink terms (growth respiration and net primary production) may be of less importance. For the current model formulation (GPPvodtemp; Equation 4.5), we now introduced an interaction term between VOD and temperature:

$$\text{GPPvodtemp} = te(VOD, T2M) + s(\Delta VOD) + s(mdnVOD) \tag{4.5}$$

where te stands for a tensor term, which represents the interaction between VOD and temperature and spans a surface in the 3-dimensional space.

Consistent with our previous model, we used GAM as regression method for deriving GPP. The pyGAM (Servén and Brummitt, 2018) version 0.8.0 provides the possibility of adding an interaction term. An advantage of GAM is that the relationships between input variables and response variable are not required to be known beforehand, but instead can be estimated from the data itself (Hastie and Tibshirani, 1987). Since the relationship between VOD and GPP as well as its relationship with temperature is difficult to determine a priori, this method is well suited for our approach.

In GAM, a number of basis spline functions are fitted to the data and the resulting function is further smoothed to obtain the final response function (Servén and Brummitt, 2018). The degree of smoothing is determined by the smoothing factor, which yields strong smoothing for high values and low smoothing for low values. For the current models we used a smoothing factor of 2, which is lower than for the model in Teubner et al. (2019). This was done since the response function for the tensor term was too smooth using the default number of 10 splines for tensor terms and resulted

in unrealistically high GPP values at high VOD. For ΔVOD, the default number of 20 splines for spline terms were used, while for $mdnVOD$ we reduced the number of splines to 5 in order to obtain a smooth relationship.

4.3.5   Statistical analysis

For model comparison, we computed Pearson correlation, unbiased Root Mean Square Error (ubRMSE) and bias. For studying the error characteristics, ubRMSE was used instead of RMSE to exclude the impact of bias, which was observed during our analysis. In addition, cross validation was computed for the above metrics using the leave-site-out method, where the model performance is evaluated at each site by omitting the respective site data from model training and then using the left-out data for computing the statistics. The analysis was carried out for the full signal and the anomalies from the mean seasonal cycle.

In case of analyzing annual GPP anomalies as a measure for interannual variability and residuals of the VOD-GPP model, we based our analysis on standardized annual or 8-daily time series data (z-scores). This was done in order to analyze GPP data in the absence of systematic differences between the data sets. The standardization for the 8-daily or the annual data was applied to each grid cell time series by subtracting the mean and dividing by the standard deviation.

For generating the smoothed time series in the calculation of ΔVOD and for aiding visual comparison in time series plots, we applied a Savitzky-Golay filter with window size of 11 data points.

4.4   Results

4.4.1   Model representation of temperature dependency

We find that the sensitivity of VOD to GPP increases with temperature as shown by the partial dependency plots (Figure 4.1). For low temperatures, the sensitivity of the VOD-GPP-relationship is relatively low (Figure 4.1a). As temperature increases, the sensitivity also increases and further exhibits an optimum behavior. At high temperatures, however, the maxima of the curves are lower than for moderate temperatures. The partial dependency for $T2M$ (Figure 4.1d) shows an optimum behavior with a peak around 20°C, which slightly differs between the VOD values. The partial dependencies for ΔVOD and $mdnVOD$ (Figure 4.1b,c) are consistent with the previous model and yield an increasing relationship with GPP for ΔVOD in the middle part of the value range and a general decreasing relationship for $mdnVOD$.

In addition to identifying the underlying relationships, we can further assess the magnitude of the contribution to GPP for the input variables based on the data range in the partial dependency plots. The main contribution to GPP in the model comes from the interaction term between VOD and $T2M$ with a range of about 12 gC m^{-2} d^{-1}, which is followed by ΔVOD with a range of about 6 gC m^{-2} d^{-1} and $mdnVOD$ with a range of about 4 gC m^{-2} d^{-1}. The contribution of the maintenance part, as represented through the interaction term, thus, is higher than for ΔVOD which represents the sum of NPP and the growth term in Ra.

4.4.2   Evaluation at site-level

At FLUXNET in situ stations, global GPP datasets overall show similar results (Figure 4.2). GPPvod exhibits a slight accumulation of GPP values at around 4 g C m^{-2} d^{-1}, while the density for
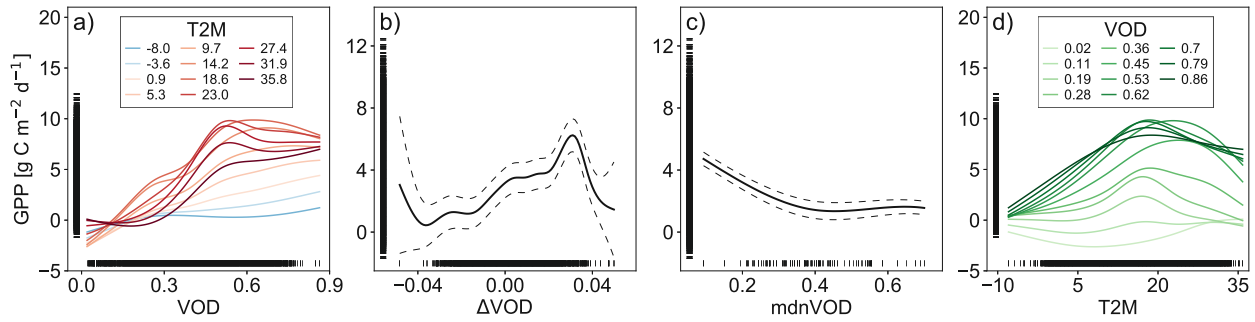
Figure 4.1: Partial dependency plot for GPPvodtemp for each input variable: (a) VOD, (b) ΔVOD, (c) $mdnVOD$ and (d) $T2M$. The model was trained with data from the period 2003-2014. Dashed lines in (b) and (c) denote the 95% confidence interval. The interaction between VOD and $T2M$ (a,d), which represents a surface in the 3-dimensional space, is displayed as projection on the 2D plane for each of the two input variables. For this, the parameter space was divided into 10 equally spaced bins between minimum and maximum of the respective variable. The bin edges are displayed as colored lines as indicated in the legend.
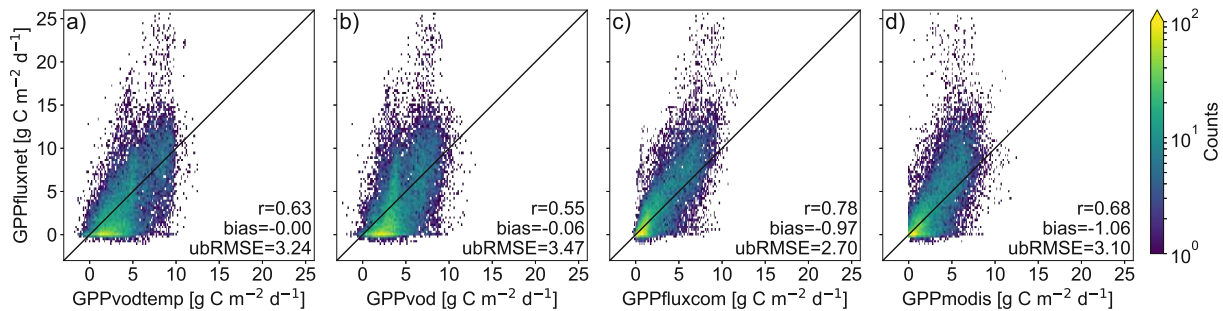
Figure 4.2: Scatter plots of 8-daily in situ GPPfluxnet versus global GPP data sets (a) GPPvodtemp, (b) GPPvod, (c) GPPfluxcom and (d) GPPmodis for the period 2003-2014.

GPPvodtemp is relatively smooth and comparable to GPPfluxcom and GPPmodis. Both GPPvod and GPPvodtemp show a relatively high number of non-zero GPP at around zero GPPfluxnet, which is less pronounced for GPPvodtemp than for GPPvod. Cross validation results in Table 4.A.2 further confirm a higher performance of GPPvodtemp compared to GPPvod. For the full signal as well as for the anomalies from the mean cycle, correlation, ubRMSE and bias generally yield higher performance for GPPvodtemp. The increase in performance is more pronounced for the full signal than for the anomalies. Despite an overall agreement of GPPvodtemp, GPPfluxcom and GPPmodis with in situ GPP, all three data sets exhibit an underestimation of GPP at high values of GPP compared with in situ GPPfluxnet. At annual time scale, the difference with GPPfluxnet at high GPP becomes much lower for GPPvodtemp compared to GPPfluxcom and GPPmodis (Figure 4.A.4), which indicates on the one hand that GPPvodtemp is able to match the in situ training data and on the other hand suggests that differences in GPP already exist between the training data set used in our study and the independent global GPP data sets, which may contribute to differences at global scale. The observed overestimation of GPP for GPPvodtemp at low in situ GPP can also be observed at annual time scale. This may be an explanation for the general tendency for overestimation of microwave-derived GPP estimates and appears not to be entirely related to the temperature sensitivity of Ra, since it is still present for GPPvodtemp.

4.4.3   Impact of adding temperature dependency at the global scale

Performance metrics for GPPvod and GPPvodtemp were assessed with respect to both GPPfluxcom and GPPmodis. Since the results for GPPfluxcom and GPPmodis are similar, we are only showing results for GPPfluxcom.

Correlations with GPPfluxcom (Figure 4.3a) reveal widespread strongly positive values with a global mean of 0.63. Some areas in the tropics and in the Australian desert exhibit an inverse temporal dynamic with GPPfluxcom. Compared with GPPvod, correlations increase in large parts of the world (Figure 4.3b) with a global average difference of 0.18. Regions that benefit most from adding temperature as input are temperate and cold regions, which could be expected since these regions per definition are strongly controlled by temperature. Tropics and subtropics, however, mainly show only minor changes in correlation coefficient with a few exceptions of decreasing correlations. Since the annual temperature amplitude in these regions is low, the model's sensitivity to temperature is also low, which makes the interaction term mainly controlled by VOD.

The global average for ubRMSE between GPPvodtemp and GPPfluxcom (Figure 4.3c) yields a value of 1.20. Consistent with the increase in performance for the correlation, areas in the temperate and cold region show an improvement in error, i.e. a decrease of ubRMSE compared to GPPvod (Figure 4.3d). Other regions, however, exhibit an increase in ubRMSE. The global average of the difference between results for GPPvodtemp and GPPvod is -0.05. Therefore, gains and losses in error are largely compensated at the global scale.

The bias between GPPvodtemp and GPPfluxcom (Figure 4.3c) is generally positive everywhere with a global average of 1.64. This finding is also evident from the higher range in the median maps for GPPvodtemp compared with GPPfluxcom and GPPmodis (Figure 4.A.2). Comparing the results for GPPvod and GPPvodtemp, the addition of temperature shows an increase in bias mainly in the tropics (Figure 4.3d), which is also evident for the difference of the median maps (Figure 4.A.2e). Despite this increase in the tropics, also regions with a reduction in bias exist, which are mainly found in temperate and cold regions. On the global scale, decreases and increases in bias compensate and yield an average difference of -0.05.

The latitudinal distribution of annual GPP (Figure 4.4a) further demonstrates that the addition of temperature yields a reduction of GPP mainly for regions outside -35°N and +60°N. The reduction in the zonal mean, however, is smaller than may have been expected probably due to compensating effects. For the region between +30°N and +60°N, where reductions in bias were observed on the global map, positive and negative values for the bias appear to compensate yielding no net reduction in the zonal mean. In the tropical region, the increase in bias for GPPvodtemp compared with GPPvod is again evident. When considering the latitudinal distribution of annual GPP relative to the latitudinal maximum, however, the distribution for GPPvodtemp is actually closer to the independent datasets than GPPvod (Figure 4.4b). This suggests that although the bias largely increases in the tropics, the relative distribution between tropics and temperate to boreal regions is better represented by the setup that includes temperature.

For a region in Europe (5 to 15°E and 46 to 51°N), where we generally did observe an increase in all three performance metrics, we find that for GPPvod mainly winter time estimates of GPP are too high compared to GPPfluxcom and GPPmodis (Figure 4.5). By adding temperature as input to the model, winter observations are markedly dampened and summer observations are only slightly increased. Nevertheless, even when including the temperature dependency, winter GPP estimates are still slightly higher for GPPvodtemp than for GPPfluxcom or GPPmodis. A similar behavior is
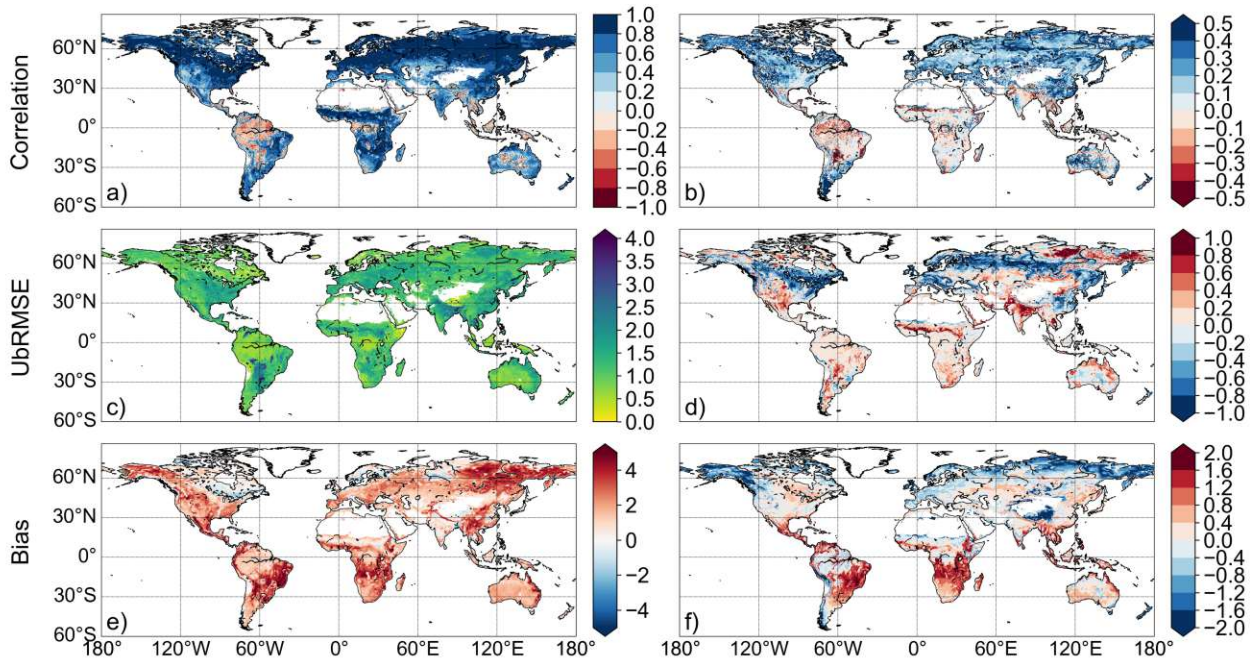
Figure 4.3: (a): Pearson correlation between GPPvodtemp and GPPfluxcom. (b): Difference between GPPvodtemp and GPPvod for Pearson correlation with GPPfluxcom. (c): ubRMSE between GPPvodtemp and GPPfluxcom. (d): Difference between GPPvodtemp and GPPvod for ubRMSE with GPPfluxcom. (e): Bias between GPPvodtemp and GPPfluxcom. (f): Difference between GPPvodtemp and GPPvod for the bias with GPPfluxcom. The unit for ubRMSE and bias is g C m^{-2} d^{-1}. Areas with non-significant correlations in (a) and (b) are marked in grey. The analysis is computed over the whole study period (2003-2015).

observed for other temperate regions (Figure 4.A.5).

In the remaining study, due to the observed bias (both at site-level and global scale), we are analyzing relative rather than absolute values for comparing interannual variability and the impact of water availability. In addition, we are focusing our further analysis on GPPvodtemp since this setup overall showed higher performance than GPPvod. Results for GPPvod are displayed in the supplement for comparison with GPPvodtemp.

4.4.4 Interannual variability and varying conditions of water availability

The latitudinal distribution of annual GPP anomalies reveals a general agreement between the GPP datasets (Figures 4.6 and 4.A.6). Although differences exist between all data sets, key features are observed among all data sets, such as the positive anomalies at -55°N in 2003, at -30°N in 2011 or at +75°N in 2012 and the negative anomalies at +75°N in 2003 and 2015 and at around -40° in 2009 and 2011. Despite the fact that these key features are found in all data sets, we also observe that the magnitude of the anomalies often differs between the data sets, which thus yields a generally relatively high variability between all data sets. In terms of the overall latitudinal pattern, it appears that GPPvodtemp is more similar to GPPmodis than to GPPfluxcom.

For the correlation of the residuals between standardized GPP (GPPvodtemp-GPPfluxcom or GPPvodtemp-GPPmodis) and SPEI, we find that large areas show no significant correlation with SPEI03 (Figure 4.7a,b). For the long-term climatological water balance, i.e. SPEI12 (Figure 4.7c,d), these areas with non-significant correlations further increase. In terms of model applicability, the non-significant correlations are the desired result. Given that correlations between GPPvodtemp and
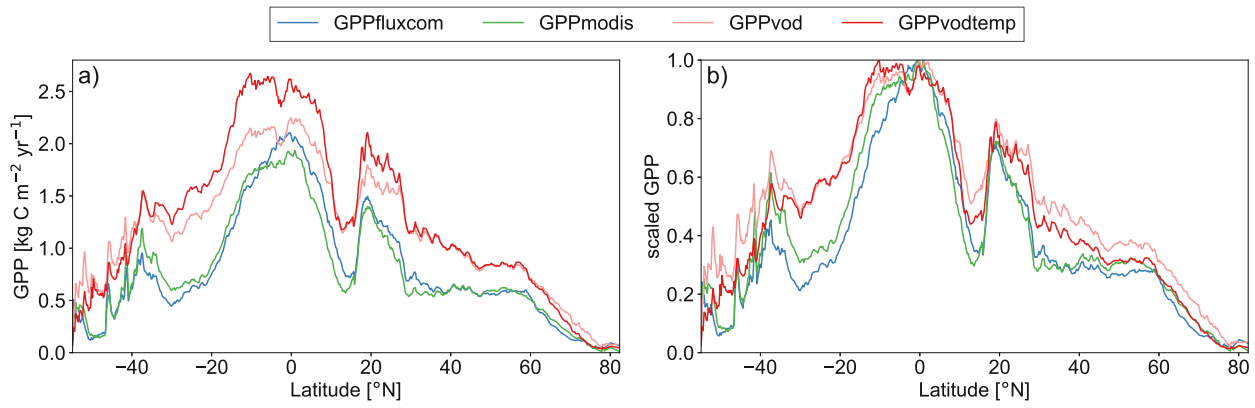
Figure 4.4: Zonal mean of annual GPP for GPPfluxcom, GPPmodis, GPPvodtemp and GPPvod for the study period 2003-2015. (a): Absolute latitudinal distribution. (b): Scaled latitudinal distribution. To obtain zonal means, data were averaged over all grid points of the same latitude. Scaled data were computed by dividing the latitudinal distribution by the maximum of the latitudinal distribution for each data set.
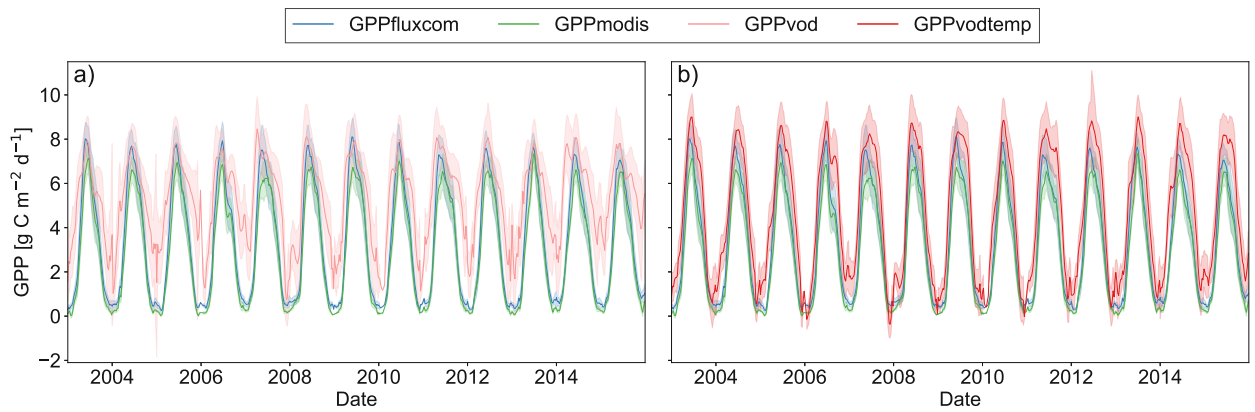
Figure 4.5: Time series plot of spatially aggregated GPP estimates for GPPfluxcom, GPPmodis and (a) GPPvod or (b) GPPvodtemp over the whole study period (2003-2015). Shaded areas indicate the standard deviation over the aggregated grid cells. The region is located in Europe, 5 to 15°E and 46 to 51°N, and was selected as an example where the correlation analysis between GPP residuals and SPEI largely yield no significant correlations. 8-daily data were smoothed to aid visual comparison.

GPPfluxcom or GPPmodis are high in these regions, this demonstrates that GPPvodtemp shows a similar behavior as GPPfluxcom or GPPmodis in response to variations in dry or wet conditions. This finding thus provides a strong indication that the VOD-GPP-relationship generally remains similar under varying conditions of water availability.

Apart from the widespread areas with non-significant correlation, some significant correlations, both positive and negative, occur at both time scales. Negative correlations indicate that during dry conditions GPPvodtemp is higher relative to the reference GPP than during wet conditions, while positive correlations mean that during dry conditions GPPvodtemp is lower relative to the reference GPP than during wet conditions. The spatial distribution of these significant correlations is largely consistent between GPPfluxcom and GPPmodis. For the short-term response to SPEI (Figure 4.7a,b), negative correlations are more frequent than positive correlations, indicating that the response to short-term drought events is often a reduction of source-driven GPP relative to sink-driven GPP. Negative correlations are mainly observed in the US corn belt, Argentina, Eastern Europe, Russia and China,
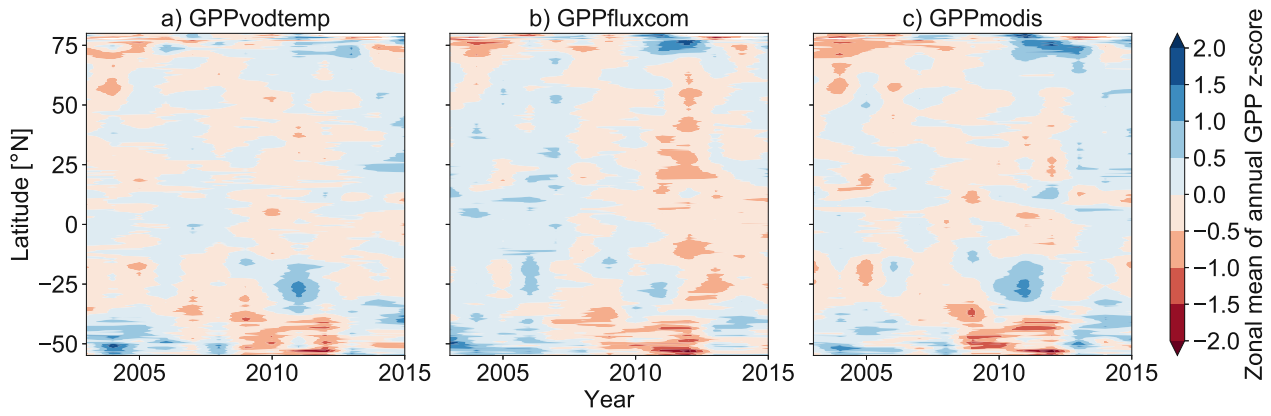
Figure 4.6: Hovmöller diagramm for zonal means of annual GPP anomalies (z-scores) for (a) GP-Pvodtemp, (b) GPPfluxcom and (c) GPPmodis over the study period. Zonal means were calculated by averaging data over all grid points of the same latitude.
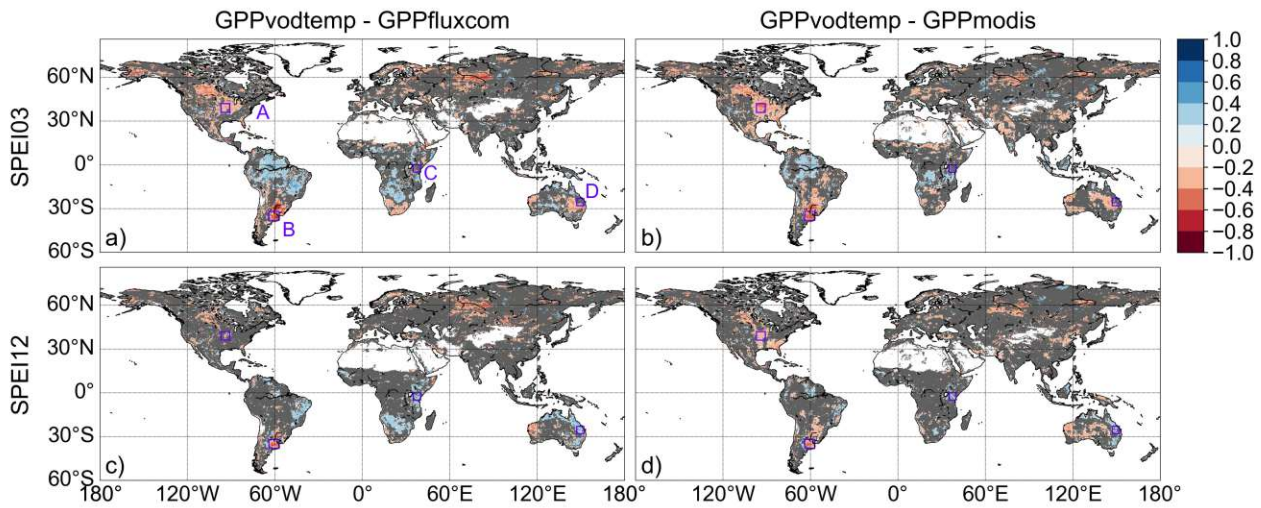
Figure 4.7: Correlation between residuals of standardized GPP (GPPvodtemp-GPPfluxcom and GPPvodtemp-GPPmodis) and SPEI. Non-significant correlations are indicated in grey. (a,c): GPPvodtemp-GPPfluxcom, (b,d): GPPvodtemp-GPPmodis, (a,b): SPEI03 (short-term response), (c,d): SPEI12 (long-term response). Regions A-D: US cornbelt (A), Argentina (B), Eastern Africa (C) and Eastern Australia (D). The analysis is based on the whole study period (2003-2015).

with the strongest negative correlations being in the US, Argentina and Russia. Positive correlations are obtained mainly over South America, Africa and Australia. For the long-term response to SPEI (Figure 4.7c,d), the number of positive correlations increase. Similar to the short-term response, positive correlations are mainly found over South America, Africa and Australia.

The analysis of GPPvod residuals reveals a similar result as for GPPvodtemp (Figure 4.A.7). For GPPvod, however, the number of grid cells with non-significant correlations in the four analyses is lower by about 2 to 4 % than for GPPvodtemp, while the global average correlation is nearly identical. The higher number of non-significant correlations for GPPvodtemp than for GPPvod is expected, because the addition of temperature accounts for some variation in the VOD-based GPP estimation.

For specific regions, which are indicated in Figure 4.7, we analyzed the time series of the standardized GPP (Figure 4.8) and the response to SPEI categories (Figure 4.A.8) in order to inspect under which situations negative or positive correlations with SPEI occur.

For the region in the US corn belt (Figure 4.8a), where we found moderately negative correlations with SPEI, all three GPP data sets show a reduction in summer GPP in 2006 and 2012. Compared with other years, however, the reduction of GPPvodtemp tends to be less than for GPPfluxcom and GPPmodis. This behavior can be verified by considering the residuals along the SPEI12 gradient (Figure 4.A.8a). During dry conditions, the residuals are higher than during wet conditions. Since higher residuals indicate that GPPvodtemp is higher relative to the reference data sets, this result confirms the findings for the time series.

In Argentina (Figure 4.8b), we observed strongly negative correlations for the analysis with SPEI. For this region, a pronounced dry condition is observed at the end of 2008 and beginning of 2009. In this period, GPPfluxcom and GPPmodis are reduced more strongly than GPPvodtemp. In the first following year, the GPPvodtemp peak is slightly lower than for GPPfluxcom and GPPmodis at the end of 2009. In the second following year, end of 2011, GPPvodtemp is similar as for GPPfluxcom and GPPmodis again. This result is further supported by the pronounced decrease of the residuals with SPEI12 in Figure 4.8b. In addition to the interannual variability, we also find that the spring peak is more pronounced in GPPfluxcom and GPPmodis than in GPPvodtemp, which might point towards a surplus of carbohydrates in spring that are incorporated for building up biomass later in the year or may be related to differences in land cover.

For the example in Africa (Figure 4.8c), where correlations with SPEI12 were positive, GPPvodtemp generally appears to be a bit higher relative to GPPfluxcom and GPPmodis at the end of each growing period. In face of dry conditions, however, GPPvodtemp shows a stronger reduction in GPP than GPPfluxcom and GPPmodis at the end of the growing season, as observed in 2006 and 2009. Despite some differences in the time series between GPPvodtemp and the reference data sets, the temporal dynamic is generally similar between the data sets. This indicates that the sink-driven GPP shows a slightly different response to changes in environmental conditions for this region, which then results in the observed positive correlations with SPEI. Considering the residuals along the SPEI12 gradient for this region, we find that the residuals increase with SPEI12 for all categories except for very wet conditions (Figure 4.A.8c).

The time series for Australia (Figure 4.8d) shows that GPPvodtemp is generally reduced during dry conditions and increases relative to GPPfluxcom and GPPmodis during wet conditions. The increase in GPPvodtemp relative to the reference data sets appears to be strongest for the period following one year after long-term dry conditions, i.e. in 2009, 2011 and 2012. Consistently, the residuals show a clear increase along the SPEI12 categories (Figure 4.A.8d).

4.5   Discussion

4.5.1   Impact of adding temperature as model input

The performance of the VOD-GPP model was shown to improve with the addition of an interaction term between VOD and temperature mainly in terms of temporal dynamic. Our results showed that the improvement in temporal dynamic was mainly observed for temperate and cold regions. Since the growing season in these regions is largely controlled by temperature, this indicates that the improvement may largely be a seasonal effect. When analyzing the temperature response of respiration across biomes, both spatial and temporal differences resulting from thermal acclimation need to be taken into account (Vanderwel et al., 2015). On the spatial scale, temperature sensitivity largely varies with mean annual temperature across biomes (Piao et al., 2010; Vanderwel et al., 2015).
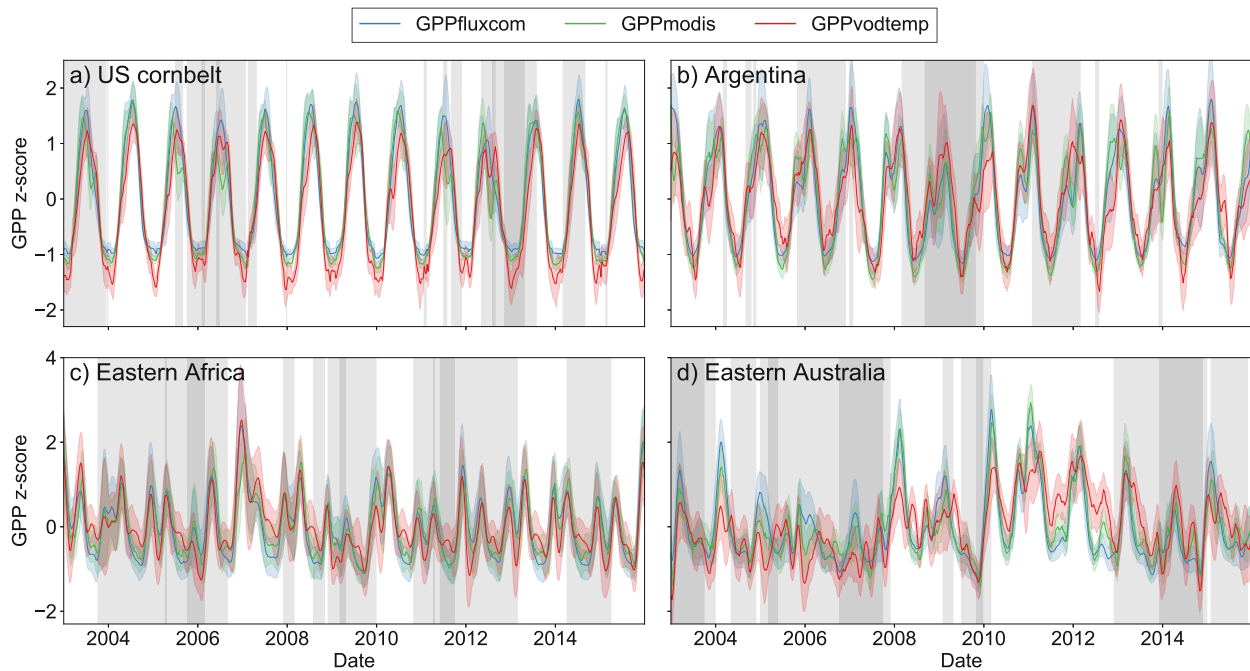
Figure 4.8: Regional mean of standardized GPP values for regions as indicated in Figure 4.7 over the study period. Shaded areas denote the standard deviation for the regional aggregated time series. Vertical grey areas indicate periods with different levels of dryness conditions for regional aggregated SPEI12: SPEI12<-1 (dark grey), -1<=SPEI12<0 (light grey) and SPEI12>=0 (white areas). Data were smoothed to aid visual comparison.

On the temporal scale, temperature-corrected respiration rates, as observed for stem respiration of deciduous trees or for needle-leave evergreen trees, exhibit a seasonal variation leading to higher respiration rates during summer than during winter (Maier et al., 1998; Ceschia et al., 2002; Vose and Ryan, 2002; Zha et al., 2004). Consistently, we observed a dampening of GPPvodtemp during winter compared to GPPvod. The addition of temperature thus seems to enable the model to reflect differences in basal respiration rates between growing and dormant periods in these regions. Although the temporal component of thermal acclimation of respiration appears to be the dominant contribution, the resulting dependency on temperature represents the cumulative effect of spatial and temporal thermal acclimation of respiration as the relationship for the temperature dependency was estimated from the data without a priori assumptions.

In addition to the temperature dependency, Ra also varies with tissue nitrogen content (Maier et al., 1998; Ceschia et al., 2002; Vose and Ryan, 2002; Tjoelker et al., 2008), which may thus contribute to uncertainties in the GPP estimation derived from VOD. Ra is also known to vary between plant tissues (Vose and Ryan, 2002; Gifford, 2003). The respiration of woody tissue is generally lower than for leaves (Vose and Ryan, 2002). Since VOD generally increases with the fraction of woody vegetation (Chaparro et al., 2019), using the median of VOD as model input may potentially compensate at least partly for differences in respiration rates of stems and branches versus leaves within a grid cell.

4.5.2 Bias between GPP data sets

The addition of temperature dependency revealed contrasting results for the bias. While reductions in bias were observed for temperate and cold regions, a strong increase in bias was found for the tropics. Since the interaction term between VOD and $T2M$ represents a relationship in the 3-dimensional

space, certain combinations of VOD and $T2M$ intervals in the parameter space may not be well represented by the training data. FLUXNET stations are not evenly distributed around the globe, as the majority of stations are located in the temperate region. This may have caused the model to be not well constrained in certain regions, e.g. where temperature and VOD are very high, and thus might have contributed to the increase in bias in the tropics. Therefore, additional FLUXNET stations might help to better constrain the VOD-GPP model. Nevertheless, differences between the dataset were already evident at the site-level, which suggests that the observed difference at global scale may at least partly be caused by differences in the training dataset. In general, the agreement in annual GPP estimates is lowest in the tropics (Anav et al., 2015). Estimates for the FLUXCOM RS setup, which was used in our study, were reported to yield lower global estimates than the FLUXCOM RS+METEO setup or GPP estimates from vegetation models (Jung et al., 2020). Similarly, MODIS was found to underestimate GPP in the tropics (Turner et al., 2006). The need for better constraints for GPP estimates especially in the tropics is well recognized (MacBean et al., 2018) and tackled in different studies (e.g., MacBean et al., 2018; Sun et al., 2018; Wu et al., 2020) but is usually hampered by the availability of in situ estimates.

4.5.3 Implications of possible saturation of VOD at high biomass

The choice of microwave frequency for the estimation of GPP may have certain implications. Different studies have demonstrated that L-band VOD yields more robust estimates of total above-ground biomass than X-band VOD, as low frequency VOD does not saturate at high biomass values (Chaparro et al., 2019; Frappart et al., 2020; Li et al., 2021). Nonetheless, the impact of such potential saturation with biomass on the estimation of GPP is less trivial, especially with regard to densely vegetated areas like the tropics. Non-linearity in the conversion between VOD and AGB should ideally be reflected in the partial dependency plot of GAM, which was also the reason for choosing this type of modelling approach. Scatterplots of the resulting GPPvodtemp estimates did not show clear signs of saturation at high in situ GPP. The FLUXNET training data set, however, only has few stations in the tropics and thus the robustness of the model may be limited by the availability of in situ stations. Apart from this, the relationship between VOD and GPP has been found to be in closer agreement for X-band VOD than for L-band (Teubner et al., 2018, 2019; Kumar et al., 2020), which was also observed for the correlation with in situ FLUXNET GPP (Figure 4.A.1). At first glance, this might appear contradictory to the above-mentioned better performance of L-band VOD for biomass estimation. A comparison of biomass estimates from different plant components with GPP, however, demonstrated that large structural components, which make up a large fraction of the total biomass, may contribute less to GPP than metabolically active plant parts (Litton et al., 2007). Since high frequency VOD is more sensitive to small plant parts like leaves and twigs (Woodhouse, 2005), this could be an explanation why X-band VOD might be better suited for the estimation of GPP and why saturation at high total above-ground biomass may be less of an issue here.

4.5.4 Independence of global GPP data sets

For the comparison with VOD-based GPP estimates, we used independent global data set from FLUX-COM and MODIS. Both data sets include to some extent information from FLUXNET data. FLUX-COM has been trained against FLUXNET data (Tramontana et al., 2016; Jung et al., 2020), however, with a larger number of stations than in the freely available Tier 1 data set that was used for our

model. Also, MODIS has been partly calibrated to some FLUXNET stations (Running et al., 1999). Therefore, the FLUXCOM and MODIS may not be fully independent from our VOD-based GPP estimates. Nevertheless, there is no alternative to constrain absolute GPP estimates at global scale than by using FLUXNET data. In addition, the agreement between GPP and VOD-based GPP estimates was also confirmed at site level using leave-site-out cross validation. Since this analysis is independent from the comparison with global data sets, it supports the use of VOD for deriving GPP.

4.5.5   The "zero-GPP problem" and non-structural carbohydrates

For GPPvodtemp, we observed that winter GPP values for an example over Europe were slightly higher compared to GPPfluxcom and GPPmodis. This issue of estimating GPP values close to zero was also observed in the scatter plots between GPPvodtemp and in situ GPPfluxnet. The reason for the overestimation at low GPP may be on the one hand an artefact related to the rehydration of plant residues after rain events and on the other hand may be explained by the sink-driven nature of our approach. In the latter case, the non-zero GPPvodtemp values may be caused by perennial vegetation. Both evergreen and deciduous vegetation are respiring throughout the dormant period (Maier et al., 1998; Vose and Ryan, 2002) and concurrently are containing water. In turn, this presence of vegetation water content is detected through microwave sensors leading to non-zero GPPvodtemp estimates. It thus may point towards the existence of a storage term. In plants, photosynthetic assimilates can be stored in the form of non-structural carbohydrates (NSC), which can be converted back to plant usable sugars to support respiration during the dormant period and growth at the start of the growing season (e.g., Martínez-Vilalta et al., 2016). For tropical forest plots, the balancing of plot level measurements of source and sink terms showed a decoupling between the two in response to drought which the authors attributed to the existence of NSC (Doughty et al., 2015b). Therefore, such a storage term can thus support a temporary imbalance between sources and sinks of carbon, which may translate into differences between source- and sink-driven GPP.

4.5.6   Magnitude of input terms

Based on the partial dependency plots, we found that for the maintenance-related term, i.e. the interaction term between VOD and $T2M$, the value range is higher than for ΔVOD. Although our model represents the sum of NPP and growth Ra and not just growth Ra, the magnitude of the two input terms is consistent with studies that analyzed the contribution of maintenance and growth to Ra. For whole plants as well as for stem respiration of boreal needle-leave trees, maintenance respiration was shown to play the dominant role for Ra with a contribution 70% (Chambers et al., 2004) and 80% (Zha et al., 2004), respectively.

4.5.7   Response to water availability

The analysis of VOD-GPP residuals with respect to FLUXCOM and MODIS revealed that GPPvodtemp largely showed a similar behavior as the independent GPP data sets as demonstrated by the widespread non-significant correlations with SPEI. This result is further supported by the general agreement in interannual variability. In addition to the possible impact of NSC, occurrences of significant correlations between VOD-GPP residuals and SPEI may indicate different plant strategies for dealing with changes in dry or wet conditions. For negative correlations, this could be mainly related to differences in plant hydraulics, while for positive correlations, it might indicate shifts between

above- and belowground carbon allocation.

Different plant strategies with regard to hydraulics can be expressed with the concept of isohydricity, which describes the regulation of stomatal control (Konings and Gentine, 2017; Giardina et al., 2018; Martínez-Vilalta and Garcia-Forner, 2017). At ecosystem level, this parameter can be obtained using the difference in twice daily overpasses of microwave observations (Konings and Gentine, 2017). Although Martínez-Vilalta and Garcia-Forner (2017) argue that the regulation of water potential may not necessarily be strongly coupled with the assimilation during drought, the degree of isohydricity may still be an explanation for the observed variation in GPPvodtemp relative to GPPfluxcom and GPPmodis. Pronounced negative correlation for the analysis of GPP residuals were found in Argentina and the US corn belt, which are regions where Konings and Gentine (2017) observed high values of isohydricity. Corn, which exhibits isohydric behavior (Lambers and Oliveira, 2019; Martínez-Vilalta and Garcia-Forner, 2017), i.e. is maintaining water potential through strong regulation of stomata, additionally has the ability, like other grasses, to roll up leaves in response to drought for reducing the loss of water from the plant's cuticular (e.g., Ribaut et al., 2009). In conjunction with the isohydric behavior, this might be an explanation for the strong signal reduction of GPPfluxcom and GPPmodis relative to GPPvodtemp observed over Argentina. Although our analysis is based on 8-daily time steps, characteristics of plant hydraulics which are retrieved from sub-daily data show similar features as for our analysis of residuals between source- and sink-driven GPP in response to changes in water availability.

In contrast to the isohydric behavior, anisohydric behavior should not lead to pronounced differences between GPPvodtemp and GPPfluxcom or GPPmodis as stomatal conductance and leaf water potential are both reduced in response to dry conditions (Lambers and Oliveira, 2019). The anisohydric behavior thus potentially relates to the non-significant correlations. Nevertheless, the degree of isohydricity may also vary between wet and dry season (Konings and Gentine, 2017), which also needs to be taken into account for the interpretation of the residuals.

The observed positive correlations, i.e. reductions of GPPvodtemp relative to GPPfluxcom or GPPmodis, could be associated with a stronger shift of assimilates to belowground plant organs. Different studies have shown that root growth may increase in face of drought to maintain water access (Sanaullah et al., 2012; Burri et al., 2014) and consequently also nutrient supply (Lambers and Oliveira, 2019). Since VOD observations only detect above-ground living vegetation, a shift towards belowground plant organs may lead to apparently lower GPPvodtemp. Nevertheless, also the inverse, i.e. an increase of allocation to shoots, was observed in the presence of legume species during drought (Sanaullah et al., 2012) and for tropical forest plots after drought (Doughty et al., 2015b).

Comparisons of GPPvodtemp with in situ observations of vegetation properties during such extreme events like drought, however, may be needed to improve the understanding of the plant's response to changes in environmental conditions at the ecosystem to global scale.

4.6   Conclusions

The VOD-GPP model was analyzed with regard to the impact of adding temperature as model input in order to account for the temperature dependency of autotrophic respiration. The resulting GPP estimates, GPPvodtemp, showed a high consistency with GPPfluxcom and GPPmodis for the temporal dynamic both at intra- and interannual time scale. For bias and error, the addition of temperature resulted in a regionally diverse response with a general improvement for temperate and cold regions

and a decrease in performance mainly in the tropics. The improvement upon adding temperature, however, was less than might have been expected, which indicates that the previous lack of temperature dependency in the model formulation can only partly account for the observed differences between the global GPP datasets. Nevertheless, this result demonstrates that an improvement by adding temperature is possible but might require further model constraints for a more robust estimation of GPP.

The analysis of the VOD-GPP residuals revealed that GPPvodtemp largely yields a similar behavior as GPPfluxcom and GPPmodis with respect to SPEI. This highlights that the relationship between VOD and GPP generally may be valid even under varying conditions of water availability. For some regions, where significant correlations were observed, the observed differences between GPPvodtemp and GPPfluxcom or GPPmodis may indicate different plant strategies for dealing with drought conditions.

Overall, our results showed that GPPvodtemp potentially contains information on plant characteristics that may be relevant for large-scale ecological studies that are addressing the response to varying environmental conditions.

4.7   Data availability

VODCA products are available at `https://doi.org/10.5281/zenodo.2575599`. FLUXCOM products are available from `http://www.fluxcom.org` or on request to Martin Jung (mjung@bgc-jena.mpg.de). MODIS GPP estimates can be accessed at `https://lpdaac.usgs.gov/products/mod17a2hv006/`. Data form the FLUXNET network is available at `https://fluxnet.org/data/fluxnet2015-dataset/`.

4.8   Author contribution

IT conceived the study, carried out the analysis and drafted the manuscript with contributions from WD and MF on the study design. BW contributed to data preparation. LM provided VOD estimates from VODCA. All authors discussed the results and commented on the manuscript.

4.9   Competing interests

The authors declare that they have no conflict of interest.

4.10   Acknowledgements

Management Project and Fluxdata project of FLUXNET, with the support of CDIAC, and the OzFlux,
ChinaFlux and AsiaFlux offices.

Appendix

4.A Supplement

Table 4.A.1: Overview of FLUXNET Tier1 v1 stations within the period 2003 to 2014. Land cover from IGBP (International Geosphere–Biosphere Programme) is obtained from the FLUXNET station metadata. Land cover abbreviations and number of stations per land cover class sorted by station number: ENF (Evergreen Needleleaf Forests; 23), GRA (Grasslands; 22), DBF (Deciduous Broadleaf Forests; 14), CRO (Croplands; 11), EBF (Evergreen Broadleaf Forests; 9), WET (Permanent Wetlands; 9), OSH (Open Shrublands; 7), MF (Mixed Forests; 6), SAV (Savannas; 6), WSA (Woody Savannas; 4) and CSH (Closed Shrublands; 1).

FLUXNET-ID	Name	Lon [° E]	Lat [° N]	Years used	Land cover
AR-SLu	San Luis	-66.46	-33.46	2009-2011	MF
AR-Vir	Virasoro	-56.19	-28.24	2010-2012	ENF
AT-Neu	Neustift	11.32	47.12	2003-2012	GRA
AU-ASM	Alice Springs	133.25	-22.28	2010-2013	ENF
AU-Ade	Adelaide River	131.12	-13.08	2007-2009	WSA
AU-Cpr	Calperum	140.59	-34.00	2010-2013	SAV
AU-Cum	Cumberland Plains	150.72	-33.61	2012-2013	EBF
AU-DaP	Daly River Savanna	131.32	-14.06	2008-2013	GRA
AU-DaS	Daly River Cleared	131.39	-14.16	2008-2013	SAV
AU-Dry	Dry River	132.37	-15.26	2008-2013	SAV
AU-Emr	Emerald, Queensland, Australia	148.47	-23.86	2011-2013	GRA
AU-Fog	Fogg Dam	131.31	-12.55	2006-2008	WET
AU-GWW	Great Western Woodlands, Western Australia, Australia	120.65	-30.19	2013-2014	SAV
AU-RDF	Red Dirt Melon Farm, Northern Territory	132.48	-14.56	2011-2013	WSA
AU-Rig	Riggs Creek	145.58	-36.65	2011-2013	GRA
AU-Rob	Robson Creek, Queensland, Australia	145.63	-17.12	2014-2014	EBF
AU-Tum	Tumbarumba	148.15	-35.66	2003-2013	EBF
AU-Whr	Whroo	145.03	-36.67	2011-2013	EBF
BE-Bra	Brasschaat	4.52	51.31	2004-2013	MF
BE-Lon	Lonzee	4.75	50.55	2004-2014	CRO
BE-Vie	Vielsalm	6.00	50.31	2003-2014	MF
BR-Sa3	Santarem-Km83-Logged Forest	-54.97	-3.02	2003-2004	EBF
CA-NS1	UCI-1850 burn site	-98.48	55.88	2003-2005	ENF
CA-NS3	UCI-1964 burn site	-98.38	55.91	2003-2005	ENF
CA-NS4	UCI-1964 burn site wet	-98.38	55.91	2003-2005	ENF
CA-NS5	UCI-1981 burn site	-98.49	55.86	2003-2005	ENF
CA-NS6	UCI-1989 burn site	-98.96	55.92	2003-2005	OSH
CA-NS7	UCI-1998 burn site	-99.95	56.64	2003-2005	OSH
CA-Qfo	Quebec - Eastern Boreal, Mature Black Spruce	-74.34	49.69	2003-2010	ENF
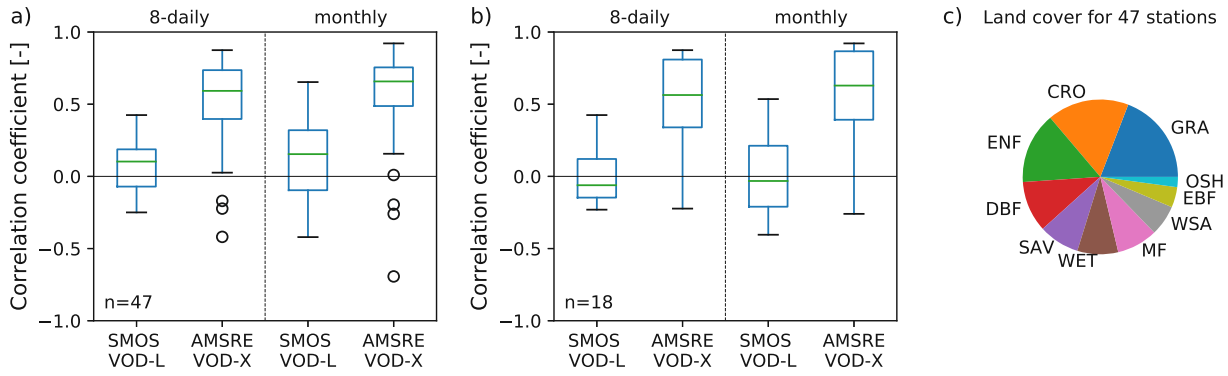
Figure 4.A.1: Pre-analysis of correlation between in situ FLUXNET GPP and single sensor VOD from
L- and X-band. (a): Pearson correlation between FLUXNET GPP (mean of GPP_DT_VUT_REF
and GPP_NT_VUT_REF) and L-band VOD (SMOS VOD-L, 7/2010–12/2014) and X-band VOD
(AMSR-E VOD-X, 1/2007–9/2011). Data were resampled to 8-daily or monthly values. The analysis
was conducted only for stations where both of the VOD data set are available (47 stations). For
details about the VOD datasets and their data processing, see Teubner et al. (2018). (b): As in
(a) but for the subset of forest land cover classes (ENF, DBF, EBF and MF). (c): Composition of
IGBP land cover classes for the stations used in this pre-analysis. Abbreviations: GRA (Grasslands),
CRO (Croplands), ENF (Evergreen Needleleaf Forests), DBF (Deciduous Broadleaf Forests), EBF
(Evergreen Broadleaf Forests), SAV (Savannas), MF (Mixed Forests), WET (Permanent Wetlands),
WSA (Woody Savannas) and OSH (Open Shrublands).
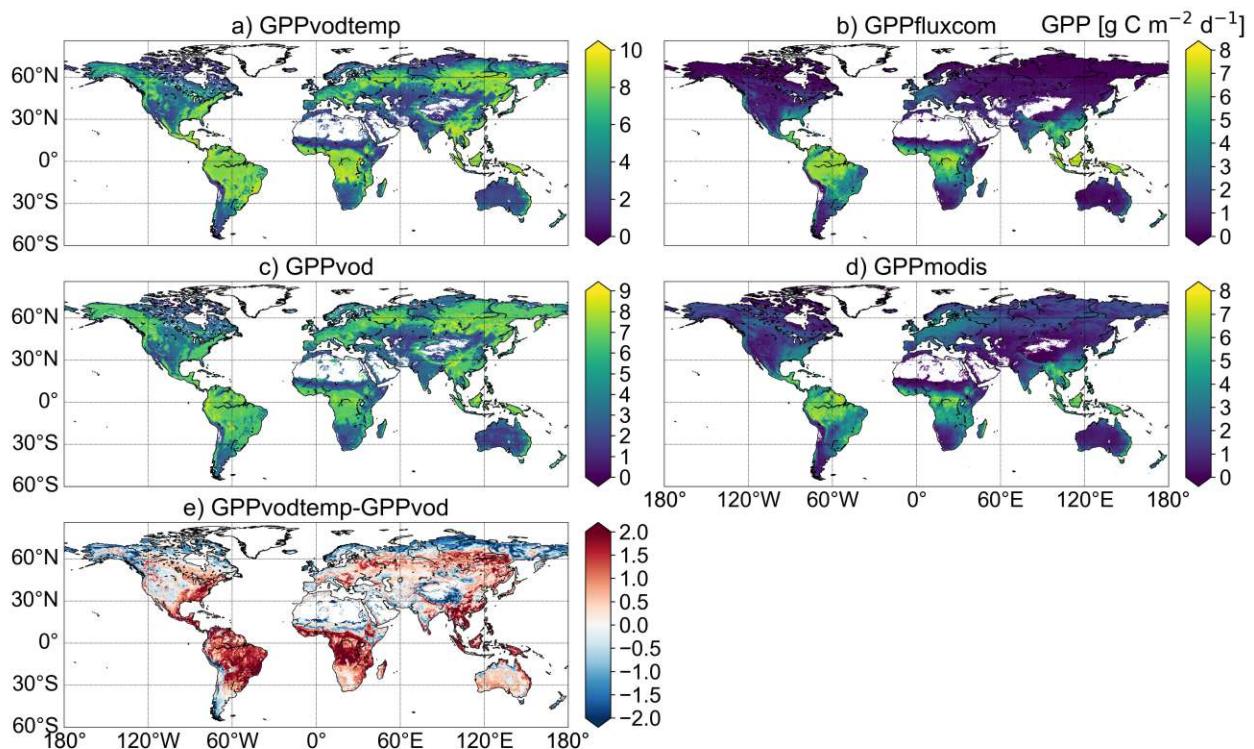
Figure 4.A.2: Temporal median maps for (a) GPPvodtemp, (b) GPPfluxcom, (c) GPPvod, (d) GPP-
modis and (e) difference between the median maps of GPPvodtemp and GPPvod. For GPPvodtemp
and GPPvod, areas where both GPPfluxcom and GPPmodis are missing were masked, since these
data were not used during the analysis. Data were computed over the whole study period (2003-2015).
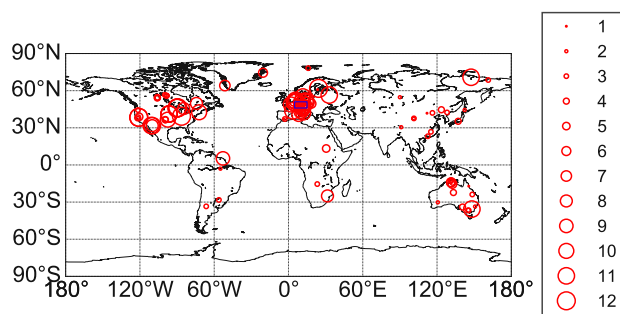
Figure 4.A.3: Location of FLUXNET Tier1 v1 stations within the period 2003 to 2014. The size of the circles represents the number of available years for each station. The blue rectangle denotes the location of the region in Europe used Figure 4.5.
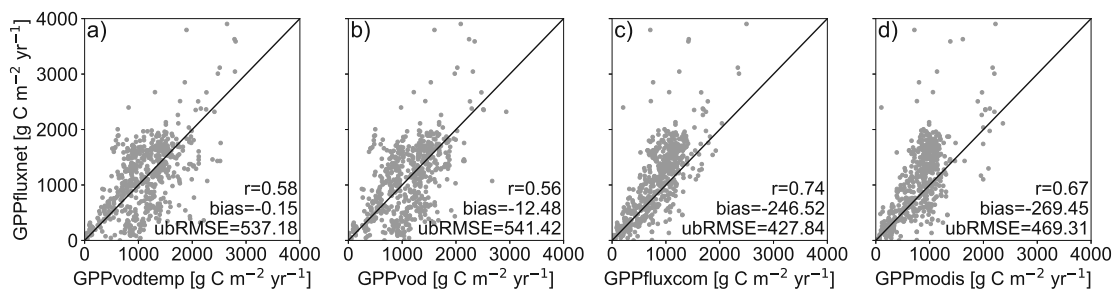
Figure 4.A.4: Scatterplot of annual GPP for GPPfluxnet versus (a) GPPvodtemp, (b) GPPvod, (c) GPPfluxcom and (d) GPPmodis. Annual values were calculated from 8-daily GPP for each data set and cover the FLUXNET period 2003-2014.

FLUXNET-ID	Name	Lon [° E]	Lat [° N]	Years used	Land cover
continued from previous page					
CA-SF1	Saskatchewan - Western Boreal, forest burned in 1977	-105.82	54.49	2003-2006	ENF
CA-SF2	Saskatchewan - Western Boreal, forest burned in 1989	-105.88	54.25	2003-2005	ENF
CA-SF3	Saskatchewan - Western Boreal, forest burned in 1998	-106.01	54.09	2003-2006	OSH
CH-Cha	Chamau	8.41	47.21	2006-2012	GRA
CH-Fru	Früebüel	8.54	47.12	2006-2012	GRA
CH-Oe1	Oensingen grassland	7.73	47.29	2003-2008	GRA
CN-Cha	Changbaishan	128.10	42.40	2003-2005	MF
CN-Cng	Changling	123.51	44.59	2007-2010	GRA
CN-Dan	Dangxiong	91.07	30.50	2004-2005	GRA
CN-Din	Dinghushan	112.54	23.17	2003-2005	EBF
CN-Du2	Duolun_grassland (D01)	116.28	42.05	2006-2008	GRA
CN-Ha2	Haibei Shrubland	101.33	37.61	2003-2005	WET
CN-HaM	Haibei Alpine Tibet site	101.18	37.37	2003-2004	GRA
CN-Qia	Qianyanzhou	115.06	26.74	2003-2005	ENF
CN-Sw2	Siziwang Grazed (SZWG)	111.90	41.79	2010-2012	GRA
CZ-BK1	Bily Kriz forest	18.54	49.50	2003-2008	ENF
CZ-BK2	Bily Kriz grassland	18.54	49.49	2004-2006	GRA
DE-Akm	Anklam	13.68	53.87	2009-2014	WET
DE-Gri	Grillenburg	13.51	50.95	2004-2014	GRA
continued on next page					
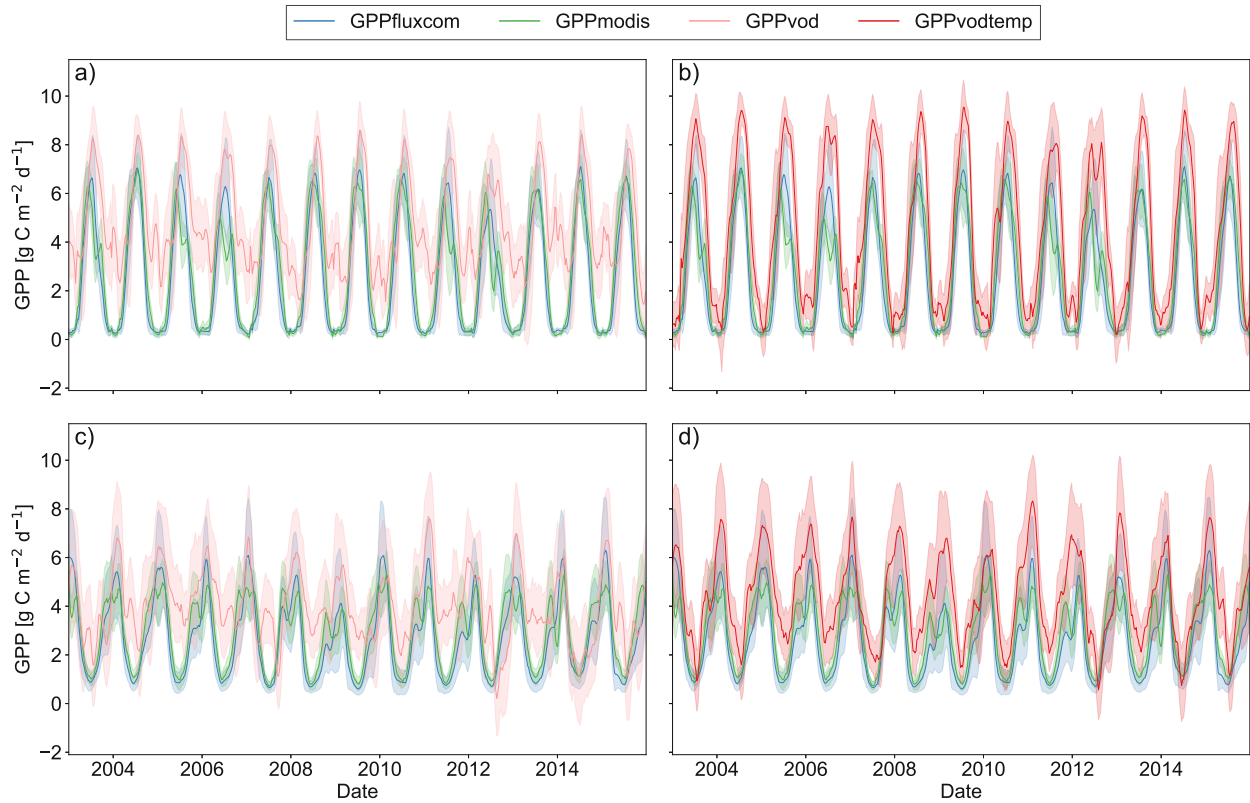
Figure 4.A.5: Time series plot of spatially aggregated GPP estimates for GPPfluxcom, GPPmodis and (a,c) GPPvod or (b,d) GPPvodtemp for the two regions US cornbelt (a,b; region A) and Argentina (c,d; region B) from Figures 4.7, 4.8 and 4.A.7. The analysis is based on the study period 2003-2015. Shaded areas represent the standard deviation over the aggregated grid cells. 8-daily data were smoothed to aid visual comparison.
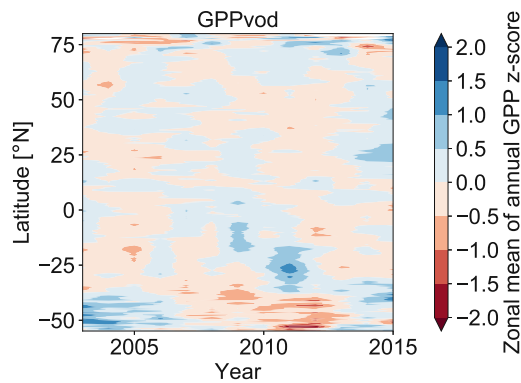
Figure 4.A.6: Hovmöller diagramm for zonal means of annual GPP anomalies (z-scores) for GPPvod over the study period 2003-2015.
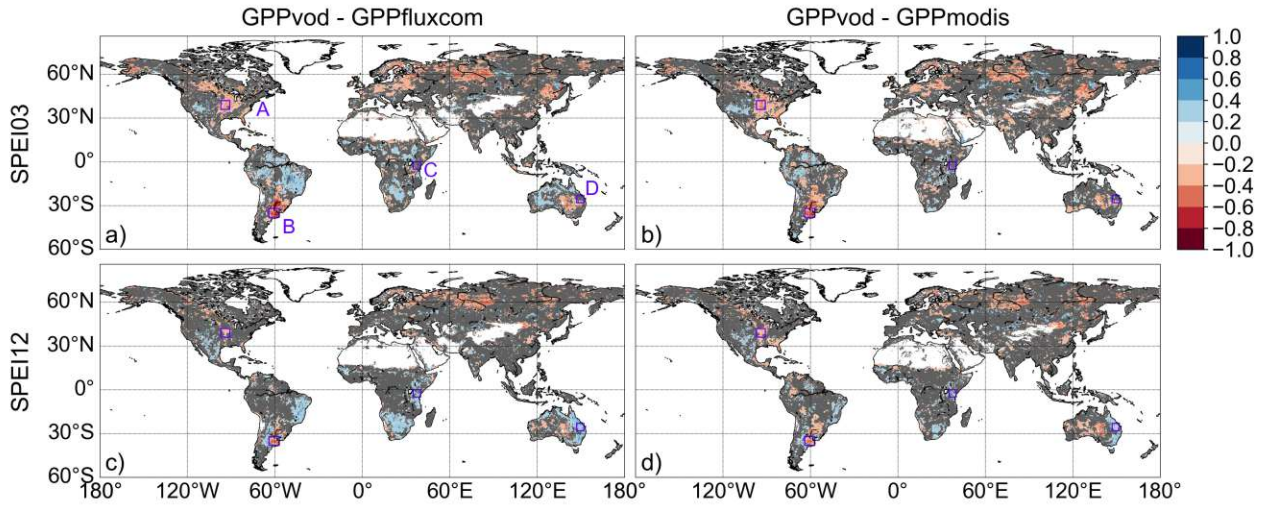
Figure 4.A.7: Correlation between residuals of standardized GPP (GPPvod-GPPfluxcom and GPPvod-GPPmodis) and SPEI. Non-significant correlations are indicated in grey. (a,c): GPPvod-GPPfluxcom, (b,d): GPPvod-GPPmodis, (a,b): SPEI03 (short-term response), (c,d): SPEI12 (long-term response). Regions A-D: US cornbelt (A), Argentina (B), Eastern Africa (C) and Eastern Australia (D). Results are computed based on the study period 2003-2015.
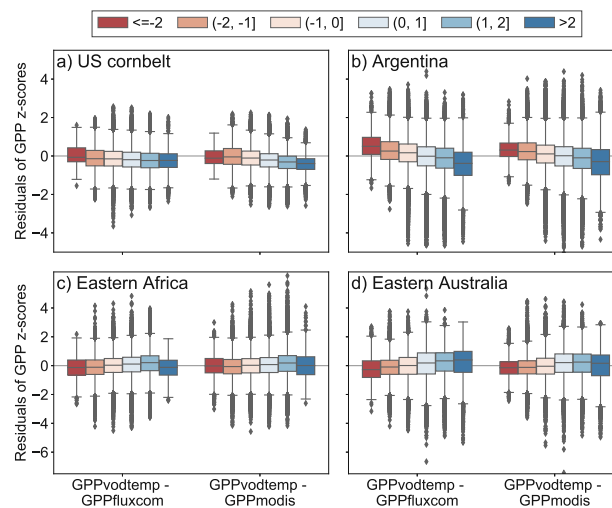
Figure 4.A.8: Boxplot of residuals between standardized GPP values of GPPvodtemp and GPPfluxcom or GPPmodis along SPEI12 categories for the data in Figure 4.8. The intervals for the different SPEI12 categories are given in the legend. Box whiskers indicate 1.5 of the interquartile range. The analysis is based on the whole study period (2003-2015).

continued from previous page

FLUXNET-ID	Name	Lon [° E]	Lat [° N]	Years used	Land cover
DE-Hai	Hainich	10.45	51.08	2003-2012	DBF
DE-Kli	Klingenberg	13.52	50.89	2004-2014	CRO
DE-Lkb	Lackenberg	13.30	49.10	2009-2013	ENF
DE-Obe	Oberbärenburg	13.72	50.78	2008-2014	ENF
DE-RuS	Selhausen Juelich	6.45	50.87	2011-2014	CRO
DE-Spw	Spreewald	14.03	51.89	2010-2014	WET
DE-Tha	Tharandt	13.57	50.96	2003-2014	ENF
DK-NuF	Nuuk Fen	-51.39	64.13	2008-2014	WET
DK-Sor	Soroe	11.64	55.49	2003-2012	DBF
DK-ZaH	Zackenberg Heath	-20.55	74.47	2003-2008	GRA
ES-LgS	Laguna Seca	-2.97	37.10	2007-2009	OSH
ES-Ln2	Lanjaron-Salvage logging	-3.48	36.97	2009-2009	OSH
FI-Hyy	Hyytiala	24.30	61.85	2003-2014	ENF
FI-Jok	Jokioinen	23.51	60.90	2003-2003	CRO
FR-Gri	Grignon	1.95	48.84	2004-2013	CRO
FR-Pue	Puechabon	3.60	43.74	2003-2013	EBF
GF-Guy	Guyaflux (French Guiana)	-52.92	5.28	2004-2012	EBF
IT-CA1	Castel d'Asso 1	12.03	42.38	2011-2013	DBF
IT-CA2	Castel d'Asso 2	12.03	42.38	2011-2013	CRO
IT-CA3	Castel d'Asso 3	12.02	42.38	2011-2013	DBF
IT-Cp2	Castelporziano 2	12.36	41.70	2012-2013	EBF
IT-Isp	Ispra ABC-IS	8.63	45.81	2013-2014	DBF
IT-Lav	Lavarone	11.28	45.96	2003-2012	ENF
IT-Noe	Arca di Noé - Le Prigionette	8.15	40.61	2004-2012	CSH
IT-PT1	Parco Ticino forest	9.06	45.20	2003-2004	DBF
IT-Ren	Renon	11.43	46.59	2003-2013	ENF
IT-Ro1	Roccarespampani 1	11.93	42.41	2003-2008	DBF
IT-Ro2	Roccarespampani 2	11.92	42.39	2003-2012	DBF
IT-SR2	San Rossore 2	10.29	43.73	2013-2014	ENF
IT-SRo	San Rossore	10.28	43.73	2003-2012	ENF
IT-Tor	Torgnon	7.58	45.84	2008-2013	GRA
JP-MBF	Moshiri Birch Forest Site	142.32	44.39	2003-2005	DBF
JP-SMF	Seto Mixed Forest Site	137.08	35.26	2003-2006	MF
NL-Hor	Horstermeer	5.07	52.24	2004-2011	GRA
NL-Loo	Loobos	5.74	52.17	2003-2013	ENF
NO-Adv	Adventdalen	15.92	78.19	2012-2014	WET
RU-Che	Cherski	161.34	68.61	2003-2005	WET
RU-Cok	Chokurdakh	147.49	70.83	2003-2013	OSH
RU-Fyo	Fyodorovskoye	32.92	56.46	2003-2013	ENF
RU-Ha1	Hakasia steppe	90.00	54.73	2003-2004	GRA
SD-Dem	Demokeya	30.48	13.28	2005-2009	SAV
US-AR1	ARM USDA UNL OSU Woodward Switchgrass 1	-99.42	36.43	2009-2012	GRA
US-AR2	ARM USDA UNL OSU Woodward Switchgrass 2	-99.60	36.64	2009-2012	GRA
US-ARM	ARM Southern Great Plains site- Lamont	-97.49	36.61	2003-2012	CRO
US-Blo	Blodgett Forest	-120.63	38.90	2003-2007	ENF
US-Ha1	Harvard Forest EMS Tower (HFR1)	-72.17	42.54	2003-2012	DBF
US-Los	Lost Creek	-89.98	46.08	2003-2014	WET
US-MMS	Morgan Monroe State Forest	-86.41	39.32	2003-2014	DBF
US-Me6	Metolius Young Pine Burn	-121.61	44.32	2010-2012	ENF

FLUXNET-ID	Name	Lon [° E]	Lat [° N]	Years used	Land cover
continued from previous page					
US-Myb	Mayberry Wetland	-121.77	38.05	2011-2014	WET
US-Ne1	Mead - irrigated continuous maize site	-96.48	41.17	2003-2013	CRO
US-Ne2	Mead - irrigated maize-soybean rotation site	-96.47	41.16	2003-2013	CRO
US-Ne3	Mead - rainfed maize-soybean rotation site	-96.44	41.18	2003-2013	CRO
US-SRM	Santa Rita Mesquite	-110.87	31.82	2004-2014	WSA
US-Syv	Sylvania Wilderness Area	-89.35	46.24	2003-2014	MF
US-Ton	Tonzi Ranch	-120.97	38.43	2003-2014	WSA
US-Tw3	Twitchell Alfalfa	-121.65	38.12	2013-2014	CRO
US-UMd	UMBS Disturbance	-84.70	45.56	2007-2014	DBF
US-Var	Vaira Ranch- Ione	-120.95	38.41	2003-2014	GRA
US-WCr	Willow Creek	-90.08	45.81	2003-2014	DBF
US-Whs	Walnut Gulch Lucky Hills Shrub	-110.05	31.74	2007-2014	OSH
US-Wkg	Walnut Gulch Kendall Grasslands	-109.94	31.74	2004-2014	GRA
ZA-Kru	Skukuza	31.50	-25.02	2003-2010	SAV
ZM-Mon	Mongu	23.25	-15.44	2007-2009	DBF

Table 4.A.2: Leave-site-out cross validation for GPPvodtemp and GPPvod. The analysis was conducted for the full signal as well as for the anomalies from the mean seasonal cycle. Anomalies were calculated after model application. Values represent mean and standard deviation of the metrics over the cross validation results for each site.

	Pearson r [-]	UbRMSE [gC m^{-2} d^{-1}]	Bias [gC m^{-2} d^{-1}]
GPPvod	0.40 ± 0.32	2.57 ± 1.14	-0.04 ± 2.01
GPPvodtemp	0.54 ± 0.31	2.30 ± 1.01	-0.08 ± 2.01
GPPvod anomalies	0.18 ± 0.22	1.57 ± 0.78	-0.00 ± 0.00
GPPvodtemp anomalies	0.22 ± 0.19	1.53 ± 0.76	0.00 ± 0.00

Chapter 5

Conclusions and outlook

In this PhD thesis, VOD was evaluated for its potential of estimating GPP. The derived VOD-GPP model showed good agreement with other remote sensing based GPP estimates, especially in terms of temporal dynamic, but tended to overestimate annual GPP as already mentioned above. The latter could only partly be reduced by accounting for the temperature dependence of autotrophic respiration in the model formulation. In tropical regions, the bias further increased when including temperature as model input. The lack of improvement for tropical regions might be attributed to the especially low spatial distribution of in situ training stations. Thus, increasing the number of in situ stations in regions with low station density might contribute to the robustness of the model estimates.

One of the aspects, which may improve model performance, is the representation of land cover. In the current model formulation, land cover is represented through the grid cell median VOD, which, however, is a static component. Although the bulk VOD signal already implicitly tracks land cover changes, the overall effect of land cover changes potentially is not fully represented since the median VOD is static per grid cell and, hence, does not change over time. In addition, the median VOD is only a rough proxy for land cover which may require refinement. Thus, analyzing the impact of a static versus a dynamic component and the model's sensitivity to different land cover classes might improve model performance.

A further aspect is the scale difference between in situ GPP training data and VOD observations. Compared with optical remote sensing, the spatial resolution of current VOD products is much lower. This coarse spatial resolution may lead to potential mismatches during model training if the station is not representative for the overall VOD grid cell. Efforts of deriving VOD products at higher spatial resolution might contribute to bridging this gap. Those efforts include the derivation of VOD from Sentinel observations (Vreugdenhil et al., 2020) or future VOD retrievals from the upcoming Copernicus Imaging Microwave Radiometer (CIMR) mission (Earth and Division, 2019). Such a higher spatial resolution of VOD observations could support more robust model training in the future.

The choice of VOD frequency for estimating GPP presented one of the key issues in this PhD thesis. Since the concept for the VOD-GPP model relies on biomass as input and since microwave observations are sensitive to the object size (Woodhouse, 2005), it was expected that L-band VOD would be better suited than high-frequency VOD. Although L-band VOD is observed to saturate less at high biomass (Chaparro et al., 2019; Frappart et al., 2020; Li et al., 2021), results in this PhD thesis demonstrated that X-band VOD yields higher performance in estimating GPP. This suggests that the small vegetation parts like leaves and twigs constitute the dominant contribution. This finding, which is supported by in situ observations of autotrophic respiration for different plant parts (Chambers

et al., 2004; Zha et al., 2004) and the comparison of GPP with plant biomass estimates Litton et al. (2007), only refers to the use of a single VOD frequency. It is not clear if the use of a single frequency is sufficient, i.e., could be justified via allometric relations to serve as proxy for all sink-terms, or if a more detailed representation of the various plant parts could help to improve the model. As metabolic activity differs between plant components such as leaves and stems (e.g., Chambers et al., 2004; Zha et al., 2004; Litton et al., 2007), an analysis of jointly using X- and L-band VOD in a multi-frequency approach could help to test this hypothesis. In addition to currently available VOD datasets, the CIMR mission will provide VOD at L-, C- and X-band from the same platform (Earth and Division, 2019), which could generate a suitable data basis for such an analysis that could thus provide further insights into the required model structure of the sink-driven approach.

In addition to uncertainties in absolute GPP values, also trends in GPP and interannual variability are subject to a high variability among GPP estimates (Anav et al., 2015). The upcoming long-term GPP record (Wild et al., 2021) presents an additional independent GPP dataset which has the potential to contribute to further investigate these observed variabilities as it presents a different perspective through the sink-term approach but at the same time is data-driven. It is important to note, however, that the satellite observations can only represent the aboveground vegetation parts. The VOD-GPP model makes the assumption that aboveground and belowground dynamics are similar. At first glance this might appear as a drawback. However, if balanced with source-driven GPP, changes in the ratio of aboveground to belowground dynamics in response to extreme environmental conditions may be detected with the VOD-based GPP estimates. As the VOD-based GPP will be available as long-term record (Wild et al., 2021), it is suitable for environmental or climate change studies that focus on quantifying sink-terms of carbon or the relation between aboveground and belowground carbon allocation.

With the all-weather capabilities of microwave observations and satellite revisit times of up to twice a day, VOD-based GPP estimates can potentially be produced at daily resolution. At such short time scale, however, the temperature dependence may result in a stronger contribution of the instantaneous temperature response of autotrophic respiration at the expense of the seasonal response and thus may differ from the relationship found at 8 day resolution. In addition, short-term variations in the vegetations water content might play a stronger role at daily time scale and could potentially affect the robustness of the model. The impact of both effects thus needs to be investigated, when aiming at increasing the temporal resolution of the VOD-GPP model.

To conclude, the VOD-GPP model presents an independent GPP data set and provides the opportunity to study sink terms in the plant carbon cycle. In conjunction with source-driven approaches, the model can thus contribute to gain knowledge about large-scale variations in carbon allocation pattern. The VOD-GPP model might thus provide the means to further our understanding on the impact of natural disturbances and how vegetation can cope with environmental changes at a large scale.

Bibliography

Akaike, H. A new look at the statistical model identification. *IEEE transactions on automatic control*, 19(6):716–723, 1974.

Alemohammad, S. H., Fang, B., Konings, A. G., Aires, F., Green, J. K., Kolassa, J., Gonzalez Miralles, D., Prigent, C., and Gentine, P. Water, energy, and carbon with artificial neural networks (wecann): a statistically based estimate of global surface turbulent fluxes and gross primary productivity using solar-induced fluorescence. *Biogeosciences*, 14(18):4101–4124, 2017.

Anav, A., Friedlingstein, P., Beer, C., Ciais, P., Harper, A., Jones, C., Murray-Tortarolo, G., Papale, D., Parazoo, N. C., Peylin, P., Piao, S., Sitch, S., Viovy, N., Wiltshire, A., and Zhao, M. Spatiotemporal patterns of terrestrial gross primary production: A review. *Reviews of Geophysics*, 53 (3):785–818, 2015. doi: https://doi.org/10.1002/2015RG000483.

Andela, N., Liu, Y., Van Dijk, A., de Jeu, R., and McVicar, T. Global changes in dryland vegetation dynamics (1988–2008) assessed by satellite remote sensing: comparing a new passive microwave vegetation density record with reflective greenness data. *Biogeosciences*, 10(10):6657–6676, 2013. doi: 10.5194/bg-10-6657-2013.

Atkin, O. K. and Tjoelker, M. G. Thermal acclimation and the dynamic response of plant respiration to temperature. *Trends in plant science*, 8(7):343–351, 2003.

Atkin, O. K., Bruhn, D., Hurry, V. M., and Tjoelker, M. G. Evans review no. 2: The hot and the cold: unravelling the variable response of plant respiration to temperature. *Functional Plant Biology*, 32 (2):87–105, 2005.

Atkin, O. K., Atkinson, L. J., Fisher, R. A., Campbell, C. D., Zaragoza-Castells, J., Pitchford, J. W., Woodward, F. I., and Hurry, V. Using temperature-dependent changes in leaf scaling relationships to quantitatively account for thermal acclimation of respiration in a coupled global climate–vegetation model. *Global change biology*, 14(11):2709–2726, 2008.

Attema, E. and Ulaby, F. T. Vegetation modeled as a water cloud. *Radio science*, 13(2):357–364, 1978.

Badgley, G., Anderegg, L. D., Berry, J. A., and Field, C. B. Terrestrial gross primary production: Using nirv to scale from site to globe. *Global change biology*, 25(11):3731–3740, 2019. doi: 10.1111/gcb.14729.

Bais, H. P., Weir, T. L., Perry, L. G., Gilroy, S., and Vivanco, J. M. The role of root exudates in rhizosphere interactions with plants and other organisms. *Annual Review of Plant Biology*, 57: 233–266, 2006. doi: 10.1146/annurev.arplant.57.032905.105159.

Baldocchi, D., Falge, E., Gu, L., Olson, R., Hollinger, D., Running, S., Anthoni, P., Bernhofer, C., Davis, K., Evans, R., Fuentes, J., Goldstein, A., Katul, G., Law, B., Lee, X., Malhi, Y., Meyers, T., Munger, W., Oechel, W., Paw U, K., Pilegaard, K., Schmid, H., Valentini, R., Verma, S., Vesala, T., Wilson, K., and Wofsy, S. Fluxnet: A new tool to study the temporal and spatial variability of ecosystem-scale carbon dioxide, water vapor, and energy flux densities. *Bulletin of the American Meteorological Society*, 82(11):2415–2434, 2001. doi: 10.1175/1520-0477(2001)082<2415: FANTTS>2.3.CO;2.

Baldocchi, D. D. Assessing the eddy covariance technique for evaluating carbon dioxide exchange rates of ecosystems: past, present and future. *Global change biology*, 9(4):479–492, 2003. doi: 10.1046/j.1365-2486.2003.00629.x.

Barnard, D. M., Meinzer, F. C., Lachenbruch, B., McCulloh, K. A., Johnson, D. M., and Woodruff, D. R. Climate-related trends in sapwood biophysical properties in two conifers: avoidance of hydraulic dysfunction through coordinated adjustments in xylem efficiency, safety and capacitance. *Plant, Cell & Environment*, 34(4):643–654, 2011.

Beck, H. E., Van Dijk, A. I., Levizzani, V., Schellekens, J., Gonzalez Miralles, D., Martens, B., and De Roo, A. Mswep: 3-hourly 0.25 global gridded precipitation (1979-2015) by merging gauge, satellite, and reanalysis data. *Hydrology and Earth System Sciences*, 21(1):589–615, 2017.

Beer, C., Reichstein, M., Tomelleri, E., Ciais, P., Jung, M., Carvalhais, N., Rödenbeck, C., Arain, M. A., Baldocchi, D., Bonan, G. B., Bondeau, A., Cescatti, A., Lasslop, G., Lindroth, A., Lomas, M., Luyssaert, S., Margolis, H., Oleson, K. W., Roupsard, O., Veenendaal, E., Viovy, N., Williams, C., Woodward, F. I., and Papale, D. Terrestrial gross carbon dioxide uptake: global distribution and covariation with climate. *Science*, 329(5993):834–838, 2010. doi: 10.1126/science.1184984.

Beguería, S., Latorre, B., Reig, F., and Vicente-Serrano, S. sbegueria/speibase: Version 2.5. 1. *Glob. SPEI Database*, 2017.

Bertin, C., Yang, X., and Weston, L. A. The role of root exudates and allelochemicals in the rhizosphere. *Plant and soil*, 256(1):67–83, 2003. doi: 10.1023/A:1026290508166.

Bonan, G. *Ecological climatology: concepts and applications*. Cambridge University Press, 2015. URL https://books.google.at/books/about/Ecological_Climatology.html?id=kq8kDQAAQBAJ.

Bonan, G. B. Forests and climate change: forcings, feedbacks, and the climate benefits of forests. *science*, 320(5882):1444–1449, 2008. doi: 10.1126/science.1155121.

Bontemps, S., Defourny, P., Radoux, J., Van Bogaert, E., Lamarche, C., Achard, F., Mayaux, P., Boettcher, M., Brockmann, C., Kirches, G., Zülkhe, M., Kalogirou, V., Seifert, F., and Arino, O. Consistent global land cover maps for climate modelling communities: current achievements of the esa's land cover cci. In *Proceedings of the ESA living planet symposium, Edimburgh*, pages 9–13, 2013. URL https://ftp.space.dtu.dk/pub/Ioana/papers/s274_2bont.pdf.

Borchert, R. Soil and stem water storage determine phenology and distribution of tropical dry forest trees. *Ecology*, 75(5):1437–1449, 1994a. doi: 10.2307/1937467.

Borchert, R. Water status and development of tropical trees during seasonal drought. *Trees*, 8(3): 115–125, 1994b. URL http://link.springer.com/article/10.1007/BF00196635.

Brandt, M., Wigneron, J.-P., Chave, J., Tagesson, T., Penuelas, J., Ciais, P., Rasmussen, K., Tian, F., Mbow, C., Al-Yaari, A., Rodriguez-Fernandez, N., Schurgers, G., Zhang, W., Chang, J., Kerr, Y., Verger, A., Tucker, C., Mialon, A., Rasmussen, L. V., Fan, L., and Fensholt, R. Satellite passive microwaves reveal recent climate-induced carbon losses in african drylands. *Nature ecology & evolution*, 2(5):827–835, 2018.

Brodribb, T. J. and Holbrook, N. M. Stomatal closure during leaf dehydration, correlation with other leaf physiological traits. *Plant Physiology*, 132(4):2166–2173, 2003.

Burri, S., Sturm, P., Prechsl, U. E., Knohl, A., and Buchmann, N. The impact of extreme summer drought on the short-term carbon coupling of photosynthesis to soil co2 efflux in a temperate grassland. *Biogeosciences*, 11(4):961–975, 2014.

C3S. C3s era5-land reanalysis. copernicus climate change service, 2019. URL `https://cds.climate.copernicus.eu/cdsapp#!/home`. 15.11.2019.

Calvet, J.-C., Wigneron, J.-P., Walker, J., Karbou, F., Chanzy, A., and Albergel, C. Sensitivity of passive microwave observations to soil moisture and vegetation water content: L-band to w-band. *IEEE Transactions on Geoscience and Remote Sensing*, 49(4):1190–1199, 2011. doi: 10.1109/TGRS.2010.2050488.

Campioli, M., Gielen, B., Göckede, M., Papale, D., Bouriaud, O., and Granier, A. Temporal variability of the npp-gpp ratio at seasonal and interannual time scales in a temperate beech forest. *Biogeosciences*, 8(9):2481–2492, 2011. doi: 10.5194/bg-8-2481-2011.

Campioli, M., Malhi, Y., Vicca, S., Luyssaert, S., Papale, D., Peñuelas, J., Reichstein, M., Migliavacca, M., Arain, M., and Janssens, I. A. Evaluating the convergence between eddy-covariance and biometric methods for assessing carbon budgets of forests. *Nature communications*, 7(1):1–12, 2016. doi: 10.1038/ncomms13717.

Ceschia, É., Damesin, C., Lebaube, S., Pontailler, J.-Y., and Dufrêne, É. Spatial and seasonal variations in stem respiration of beech trees (fagus sylvatica). *Annals of Forest Science*, 59(8):801–812, 2002.

Chambers, J. Q., Tribuzy, E. S., Toledo, L. C., Crispim, B. F., Higuchi, N., Santos, J. d., Araújo, A. C., Kruijt, B., Nobre, A. D., and Trumbore, S. E. Respiration from a tropical forest ecosystem: partitioning of sources and low carbon use efficiency. *Ecological Applications*, 14(sp4):72–88, 2004.

Chaparro, D., Piles, M., Vall-Llossera, M., Camps, A., Konings, A. G., and Entekhabi, D. L-band vegetation optical depth seasonal metrics for crop yield assessment. *Remote Sensing of Environment*, 212:249–259, 2018.

Chaparro, D., Duveiller, G., Piles, M., Cescatti, A., Vall-Llossera, M., Camps, A., and Entekhabi, D. Sensitivity of l-band vegetation optical depth to carbon stocks in tropical forests: a comparison to higher frequencies and optical indices. *Remote sensing of environment*, 232:111303, 2019. doi: https://doi.org/10.1016/j.rse.2019.111303.

Chen, B., Ge, Q., Fu, D., Yu, G., Sun, X., Wang, S., and Wang, H. A data-model fusion approach for upscaling gross ecosystem productivity to the landscape scale based on remote sensing and flux footprint modelling. *Biogeosciences*, 7(9):2943–2958, 2010. doi: 10.5194/bg-7-2943-2010.

Chen, J., Jönsson, P., Tamura, M., Gu, Z., Matsushita, B., and Eklundh, L. A simple method for reconstructing a high-quality ndvi time-series data set based on the savitzky–golay filter. *Remote sensing of Environment*, 91(3-4):332–344, 2004. doi: 10.1016/j.rse.2004.03.014.

Ciais, P., Sabine, C., Bala, G., Bopp, L., Brovkin, V., Canadell, J., Chhabra, A., DeFries, R., Galloway, J., Heimann, M., Jones, C., Le Quéré, C., Myneni, R., Piao, S., and Thornton, P. Carbon and other biogeochemical cycles. In Stocker, T., Qin, D., Plattner, G.-K., Tignor, M., Allen, S., Boschung, J., Nauels, A., Xia, Y., Bex, V., and Midgley, P., editors, *Climate change 2013: the physical science basis. Contribution of Working Group I to the Fifth Assessment Report of the Intergovernmental Panel on Climate Change*. Cambridge University Press, Cambridge, United Kingdom and New York, NY, USA, 2013.

Clark, D. A., Brown, S., Kicklighter, D. W., Chambers, J. Q., Thomlinson, J. R., and Ni, J. Measuring net primary production in forests: concepts and field methods. *Ecological applications*, 11(2):356–370, 2001a. doi: 10.1890/1051-0761(2001)011[0356:MNPPIF]2.0.CO;2.

Clark, D. A., Brown, S., Kicklighter, D. W., Chambers, J. Q., Thomlinson, J. R., Ni, J., and Holland, E. A. Net primary production in tropical forests: an evaluation and synthesis of existing field data. *Ecological applications*, 11(2):371–384, 2001b. URL `ftp://ftp.forest.sr.unh.edu/pub/ MLSmith/John20R/Backup/NPP,carbon20pub/i1051-0761-011-02-0371.pdf`.

Collatz, G. J., Ribas-Carbo, M., and Berry, J. Coupled photosynthesis-stomatal conductance model for leaves of c4 plants. *Functional Plant Biology*, 19(5):519–538, 1992. doi: 10.1071/PP9920519.

Crocetti, L., Forkel, M., Fischer, M., Jurečka, F., Grlj, A., Salentinig, A., Trnka, M., Anderson, M., Ng, W.-T., Kokalj, Ž., Bucur, A., and Dorigo, W. Earth observation for agricultural drought monitoring in the pannonian basin (southeastern europe): current state and future directions. *Regional Environmental Change*, 20(4):1–17, 2020. doi: https://doi.org/10.1007/s10113-020-01710-w.

D'Agostino, R. and Pearson, E. Tests for departure from normality. Empirical results for the distributions of b2 and $\sqrt{b1}$. *Biometrika*, 60(3):613–622, 1973. doi: 10.1093/biomet/60.3.613.

D'Agostino, R. B. An omnibus test of normality for moderate and large size samples. *Biometrika*, 58(2):341–348, 1971. doi: 10.1093/biomet/58.2.341.

Damm, A., Guanter, L., Paul-Limoges, E., Van der Tol, C., Hueni, A., Buchmann, N., Eugster, W., Ammann, C., and Schaepman, M. E. Far-red sun-induced chlorophyll fluorescence shows ecosystem-specific relationships to gross primary production: An assessment based on observational and modeling approaches. *Remote Sensing of Environment*, 166:91–105, 2015. doi: 10.1016/j.rse.2015.06.004.

Damour, G., Simonneau, T., Cochard, H., and Urban, L. An overview of models of stomatal conductance at the leaf level. *Plant, cell & environment*, 33(9):1419–1438, 2010. doi: 10.1111/j.1365-3040.2010.02181.x.

De Jeu, R. A., Wagner, W., Holmes, T., Dolman, A., Van De Giesen, N., and Friesen, J. Global soil moisture patterns observed by space borne microwave radiometers and scatterometers. *Surveys in Geophysics*, 29(4-5):399–420, 2008. doi: 10.1007/s10712-008-9044-0.

De Keersmaecker, W., Lhermitte, S., Tits, L., Honnay, O., Somers, B., and Coppin, P. A model quantifying global vegetation resistance and resilience to short-term climate anomalies and their

relationship with vegetation cover. *Global Ecology and Biogeography*, 24(5):539–548, 2015. doi: 10.1111/geb.12279.

Dee, D. P., Uppala, S., Simmons, A., Berrisford, P., Poli, P., Kobayashi, S., Andrae, U., Balmaseda, M., Balsamo, G., Bauer, P., Bechtold, P., Beljaars, A., van de Berg, L., Bidlot, J., Bormann, N., Delsol, C., Dragani, R., Fuentes, M., Geer, A., Haimberger, L., Healy, S., Hersbach, H., Hólm, E., Isaksen, L., Kållberg, P., Köhler, M., Matricardi, M., McNally, A., Monge-Sanz, B., Morcrette, J.-J., Park, B.-K., Peubey, C., de Rosnay, P., Tavolato, C., Thépaut, J.-N., and Vitart, F. The era-interim reanalysis: Configuration and performance of the data assimilation system. *Quarterly Journal of the royal meteorological society*, 137(656):553–597, 2011.

Dorigo, W., Gruber, A., de Jeu, R., Wagner, W., Stacke, T., Loew, A., Albergel, C., Brocca, L., Chung, D., Parinussa, R., and Kidd, R. Evaluation of the esa cci soil moisture product using ground-based observations. *Remote Sensing of Environment*, 162:380–395, 2015. doi: 10.1016/j.rse.2014.07.023.

Dorigo, W. A. Improving the robustness of cotton status characterisation by radiative transfer model inversion of multi-angular chris/proba data. *IEEE Journal of Selected Topics in Applied Earth Observations and Remote Sensing*, 5(1):18–29, 2012. doi: 10.1109/JSTARS.2011.2171181.

Dorigo, W. A., Zurita-Milla, R., de Wit, A. J., Brazile, J., Singh, R., and Schaepman, M. E. A review on reflective remote sensing and data assimilation techniques for enhanced agroecosystem modeling. *International journal of applied earth observation and geoinformation*, 9(2):165–193, 2007. doi: 10.1016/j.jag.2006.05.003.

Doughty, C. E., Metcalfe, D., Girardin, C., Amezquita, F. F., Cabrera, D. G., Huasco, W. H., Silva-Espejo, J., Araujo-Murakami, A., Da Costa, M., Rocha, W., Feldpausch, T., Mendoza, A., da Costa, A., Meir, P., Phillips, O., and Malhi, Y. Drought impact on forest carbon dynamics and fluxes in amazonia. *Nature*, 519(7541):78–82, 2015a. doi: 10.1038/nature14213.

Doughty, C. E., Metcalfe, D., Girardin, C. A., Amezquita, F. F., Durand, L., Huasco, W. H., Silva-Espejo, J. E., Araujo-Murakami, A., Da Costa, M., da Costa, A. C. L., Rocha, W., Meir, P., Galbraith, D., and Malhi, Y. Source and sink carbon dynamics and carbon allocation in the amazon basin. *Global Biogeochemical Cycles*, 29(5):645–655, 2015b.

Drake, J. E., Tjoelker, M. G., Aspinwall, M. J., Reich, P. B., Barton, C. V., Medlyn, B. E., and Duursma, R. A. Does physiological acclimation to climate warming stabilize the ratio of canopy respiration to photosynthesis? *New Phytologist*, 211(3):850–863, 2016.

Draper, C., Reichle, R., De Lannoy, G., and Liu, Q. Assimilation of passive and active microwave soil moisture retrievals. *Geophysical Research Letters*, 39(4), 2012. doi: 10.1029/2011GL050655.

Du, J., Kimball, J. S., Jones, L. A., Kim, Y., Glassy, J., and Watts, J. D. A global satellite environmental data record derived from amsr-e and amsr2 microwave earth observations. *Earth System Science Data*, 9(2):791–808, 2017. doi: 10.5194/essd-9-791-2017.

Earth and Division, M. S. Copernicus imaging microwave radiometer (CIMR) requirements document, 2019. URL https://cimr.eu/sites/cimr.met.no/files/documents/CIMR-MRD-v2.0-20190305-ISSUED_0.pdf.

El Hajj, M., Baghdadi, N., Wigneron, J.-P., Zribi, M., Albergel, C., Calvet, J.-C., and Fayad, I. First vegetation optical depth mapping from sentinel-1 c-band sar data over crop fields. *Remote Sensing*, 11(23):2769, 2019. doi: 10.3390/rs11232769.

Fan, L., Wigneron, J.-P., Ciais, P., Chave, J., Brandt, M., Fensholt, R., Saatchi, S. S., Bastos, A., Al-Yaari, A., Hufkens, K., Qin, Y., Xiao, X., Chen, C., Myneni, R. B., Fernandez-Moran, R., Mialon, A., Rodriguez-Fernandez, N., Kerr, Y., Tian, F., and Peñuelas, J. Satellite-observed pantropical carbon dynamics. *Nature plants*, 5(9):944–951, 2019.

Farquhar, G. D., von Caemmerer, S. v., and Berry, J. A. A biochemical model of photosynthetic CO2 assimilation in leaves of C3 species. *Planta*, 149(1):78–90, 1980. doi: 10.1007/BF00386231.

Fatichi, S., Leuzinger, S., and Körner, C. Moving beyond photosynthesis: from carbon source to sink-driven vegetation modeling. *New Phytologist*, 201(4):1086–1095, 2014.

Feldman, A. F., Gianotti, D. J. S., Konings, A. G., McColl, K. A., Akbar, R., Salvucci, G. D., and Entekhabi, D. Moisture pulse-reserve in the soil-plant continuum observed across biomes. *Nature plants*, 4(12):1026–1033, 2018.

Fisher, R. A., Williams, M., Do Vale, R. L., Da Costa, A. L., and Meir, P. Evidence from amazonian forests is consistent with isohydric control of leaf water potential. *Plant, Cell & Environment*, 29 (2):151–165, 2006. doi: 10.1111/j.1365-3040.2005.01407.x.

Forkel, M., Carvalhais, N., Verbesselt, J., Mahecha, M. D., Neigh, C. S., and Reichstein, M. Trend change detection in ndvi time series: Effects of inter-annual variability and methodology. *Remote Sensing*, 5(5):2113–2144, 2013. doi: 10.3390/rs5052113.

Forkel, M., Dorigo, W., Lasslop, G., Teubner, I., Chuvieco, E., and Thonicke, K. A data-driven approach to identify controls on global fire activity from satellite and climate observations (sofia v1). *Geoscientific Model Development*, 10(12):4443–4476, 2017. doi: 10.5194/gmd-10-4443-2017.

Forkel, M., Dorigo, W., Lasslop, G., Chuvieco, E., Hantson, S., Heil, A., Teubner, I., Thonicke, K., and Harrison, S. P. Recent global and regional trends in burned area and their compensating environmental controls. *Environmental Research Communications*, 1(5):051005, 2019. doi: 10.1088/2515-7620/ab25d2.

Frankenberg, C., Fisher, J. B., Worden, J., Badgley, G., Saatchi, S. S., Lee, J.-E., Toon, G. C., Butz, A., Jung, M., Kuze, A., and Yokota, T. New global observations of the terrestrial carbon cycle from gosat: Patterns of plant fluorescence with gross primary productivity. *Geophysical Research Letters*, 38(17), 2011. doi: 10.1029/2011GL048738.

Frankenberg, C., O'Dell, C., Berry, J., Guanter, L., Joiner, J., Köhler, P., Pollock, R., and Taylor, T. E. Prospects for chlorophyll fluorescence remote sensing from the orbiting carbon observatory-2. *Remote Sensing of Environment*, 147:1–12, 2014. doi: 10.1016/j.rse.2014.02.007.

Frappart, F., Wigneron, J.-P., Li, X., Liu, X., Al-Yaari, A., Fan, L., Wang, M., Moisy, C., Le Masson, E., Lafkih, Z. A., Vallé, C., Ygorra, B., and Baghdadi, N. Global monitoring of the vegetation dynamics from the vegetation optical depth (vod): A review. *Remote Sensing*, 12(18):2915, 2020. doi: 10.3390/rs12182915.

Giardina, F., Konings, A. G., Kennedy, D., Alemohammad, S. H., Oliveira, R. S., Uriarte, M., and Gentine, P. Tall amazonian forests are less sensitive to precipitation variability. *Nature Geoscience*, 11(6):405–409, 2018.

Gifford, R. M. Plant respiration in productivity models: conceptualisation, representation and issues for global terrestrial carbon-cycle research. *Functional Plant Biology*, 30(2):171–186, 2003.

Gilabert, M. A., Sánchez-Ruiz, S., and Moreno, Á. Annual gross primary production from vegetation indices: A theoretically sound approach. *Remote Sensing*, 9(3):193, 2017. doi: 10.3390/rs9030193.

Girardin, C. A. J., Malhi, Y., Aragao, L., Mamani, M., Huaraca Huasco, W., Durand, L., Feeley, K., Rapp, J., Silva-Espejo, J., Silman, M., Salinas, N., and Whittaker, R. Net primary productivity allocation and cycling of carbon along a tropical forest elevational transect in the peruvian andes. *Global Change Biology*, 16(12):3176–3192, 2010. doi: 10.1111/j.1365-2486.2010.02235.x.

Gitelson, A. A., Peng, Y., Arkebauer, T. J., and Schepers, J. Relationships between gross primary production, green lai, and canopy chlorophyll content in maize: Implications for remote sensing of primary production. *Remote Sensing of Environment*, 144:65–72, 2014. doi: 10.1016/j.rse.2014.01.004.

Good, S. P., Moore, G. W., and Miralles, D. G. A mesic maximum in biological water use demarcates biome sensitivity to aridity shifts. *Nature ecology & evolution*, 1(12):1883, 2017.

Goodrich, J., Campbell, D., Clearwater, M., Rutledge, S., and Schipper, L. High vapor pressure deficit constrains gpp and the light response of nee at a southern hemisphere bog. *Agricultural and Forest Meteorology*, 203:54–63, 2015.

Gower, S., Krankina, O., Olson, R., Apps, M., Linder, S., and Wang, C. Net primary production and carbon allocation patterns of boreal forest ecosystems. *Ecological applications*, 11(5):1395–1411, 2001. doi: 10.1890/1051-0761(2001)011[1395:NPPACA]2.0.CO;2.

Greve, P., Orlowsky, B., Mueller, B., Sheffield, J., Reichstein, M., and Seneviratne, S. I. Global assessment of trends in wetting and drying over land. *Nature geoscience*, 7(10):716, 2014.

Guan, K., Berry, J. A., Zhang, Y., Joiner, J., Guanter, L., Badgley, G., and Lobell, D. B. Improving the monitoring of crop productivity using spaceborne solar-induced fluorescence. *Global change biology*, 22(2):716–726, 2016. doi: 10.1111/gcb.13136.

Guanter, L., Frankenberg, C., Dudhia, A., Lewis, P. E., Gómez-Dans, J., Kuze, A., Suto, H., and Grainger, R. G. Retrieval and global assessment of terrestrial chlorophyll fluorescence from gosat space measurements. *Remote Sensing of Environment*, 121:236–251, 2012. doi: 10.1016/j.rse.2012.02.006.

Guanter, L., Zhang, Y., Jung, M., Joiner, J., Voigt, M., Berry, J. A., Frankenberg, C., Huete, A. R., Zarco-Tejada, P., Lee, J.-E., Moran, M. S., Ponce-Campos, G., Beer, C., Camps-Valls, G., Buchmann, N., Gianelle, D., Klumpp, K., Cescatti, A., Baker, J. M., and Griffis, T. J. Global and time-resolved monitoring of crop photosynthesis with chlorophyll fluorescence. *Proceedings of the National Academy of Sciences*, 111(14):E1327–E1333, 2014. doi: 10.1073/pnas.1320008111.

Guenther, A. The contribution of reactive carbon emissions from vegetation to the carbon balance of terrestrial ecosystems. *Chemosphere*, 49(8):837–844, 2002. doi: 10.1016/S0045-6535(02)00384-3.

Guenther, A., Hewitt, C. N., Erickson, D., Fall, R., Geron, C., Graedel, T., Harley, P., Klinger, L., Lerdau, M., McKay, W., Pierce, T., Scholes, B., Steinbrecher, R., Tallamraju, R., Taylor, J., and Zimmerman, P. A global model of natural volatile organic compound emissions. *Journal of Geophysical Research: Atmospheres*, 100(D5):8873–8892, 1995. doi: 10.1029/94JD02950.

Hahn, S., Reimer, C., Vreugdenhil, M., Melzer, T., and Wagner, W. Dynamic characterization of the incidence angle dependence of backscatter using metop ascat. *IEEE Journal of Selected Topics in Applied Earth Observations and Remote Sensing*, 10(5):2348–2359, 2017. doi: 10.1109/JSTARS. 2016.2628523.

Hastie, T. and Tibshirani, R. Generalized additive models: some applications. *Journal of the American Statistical Association*, 82(398):371–386, 1987.

Hastie, T. and Tibshirani, R. *Generalized additive models*. Chapman & Hall/CRC, Boca Raton, Fla, 1990. ISBN 978-0-412-34390-2.

Hersbach, H., Bell, B., Berrisford, P., Hirahara, S., Horányi, A., Muñoz-Sabater, J., Nicolas, J., Peubey, C., Radu, R., Schepers, D., Simmons, A., Soci, C., Abdalla, S., Abellan, X., Balsamo, G., Bechtold, P., Biavati, G., Bidlot, J., Bonavita, M., De Chiara, G., Dahlgren, P., Dee, D., Diamantakis, M., Dragani, R., Flemming, J., Forbes, R., Fuentes, M., Geer, A., Haimberger, L., Healy, S., Hogan, R. J., Hólm, E., Janisková, M., Keeley, S., Laloyaux, P., Lopez, P., Lupu, C., Radnoti, G., de Rosnay, P., Rozum, I., Vamborg, F., Villaume, S., and Thépaut, J.-N. The era5 global reanalysis. *Quarterly Journal of the Royal Meteorological Society*, 146(730):1999–2049, 2020. doi: https://doi.org/10.1002/qj.3803.

Holben, B. N. Characteristics of maximum-value composite images from temporal avhrr data. *International journal of remote sensing*, 7(11):1417–1434, 1986. doi: 10.1080/01431168608948945.

Huete, A., Didan, K., van Leeuwen, W., Miura, T., and Glenn, E. Modis vegetation indices. In *Land remote sensing and global environmental change*, pages 579–602. Springer, 2011. URL http://link.springer.com/chapter/10.1007/978-1-4419-6749-7_26.

Huete, A. R., Didan, K., Shimabukuro, Y. E., Ratana, P., Saleska, S. R., Hutyra, L. R., Yang, W., Nemani, R. R., and Myneni, R. Amazon rainforests green-up with sunlight in dry season. *Geophysical research letters*, 33(6), 2006. doi: 10.1029/2005GL025583.

Huffman, G. J., Adler, R. F., Morrissey, M. M., Bolvin, D. T., Curtis, S., Joyce, R., McGavock, B., and Susskind, J. Global precipitation at one-degree daily resolution from multisatellite observations. *Journal of hydrometeorology*, 2(1):36–50, 2001. doi: 10.1175/1525-7541(2001)002<0036:GPAODD> 2.0.CO;2.

Hutyra, L. R., Munger, J. W., Saleska, S. R., Gottlieb, E., Daube, B. C., Dunn, A. L., Amaral, D. F., De Camargo, P. B., and Wofsy, S. C. Seasonal controls on the exchange of carbon and water in an amazonian rain forest. *Journal of Geophysical Research: Biogeosciences*, 112(G3), 2007. doi: 10.1029/2006JG000365.

Intergovernmental Panel on Climate Change. *Global warming of 1.5° C: an IPCC special report on the impacts of global warming of 1.5° C above pre-industrial levels and related global greenhouse gas emission pathways, in the context of strengthening the global response to the threat of climate change,*

sustainable development, and efforts to eradicate poverty. Intergovernmental Panel on Climate Change, 2018.

Jackson, T. and Schmugge, T. Vegetation effects on the microwave emission of soils. *Remote Sensing of Environment*, 36(3):203–212, 1991. doi: 10.1016/0034-4257(91)90057-D.

Joiner, J., Guanter, L., Lindstrot, R., Voigt, M., Vasilkov, A., Middleton, E., Huemmrich, K., Yoshida, Y., and Frankenberg, C. Global monitoring of terrestrial chlorophyll fluorescence from moderate-spectral-resolution near-infrared satellite measurements: methodology, simulations, and application to gome-2. *Atmospheric Measurement Techniques*, 6(10):2803–2823, 2013. URL http://www.atmos-meas-tech.net/6/2803/2013/amt-6-2803-2013.pdf.

Joiner, J., Yoshida, Y., Vasilkov, A., Schaefer, K., Jung, M., Guanter, L., Zhang, Y., Garrity, S., Middleton, E., Huemmrich, K., Gu, L., and Belelli Marchesini, L. The seasonal cycle of satellite chlorophyll fluorescence observations and its relationship to vegetation phenology and ecosystem atmosphere carbon exchange. *Remote Sensing of Environment*, 152:375–391, 2014. doi: 10.1016/j.rse.2014.06.022.

Joiner, J., Yoshida, Y., Guanter, L., and Middleton, E. M. New methods for the retrieval of chlorophyll red fluorescence from hyperspectral satellite instruments: simulations and application to gome-2 and sciamachy. *Atmospheric Measurement Techniques*, 9(8):3939–3967, 2016. doi: 10.5194/amt-9-3939-2016.

Jones, D. L., Nguyen, C., and Finlay, R. D. Carbon flow in the rhizosphere: carbon trading at the soil–root interface. *Plant and soil*, 321(1):5–33, 2009. doi: 10.1007/s11104-009-9925-0.

Jones, M. O., Jones, L. A., Kimball, J. S., and McDonald, K. C. Satellite passive microwave remote sensing for monitoring global land surface phenology. *Remote Sensing of Environment*, 115(4): 1102–1114, 2011. doi: 10.1016/j.rse.2010.12.015.

Jones, M. O., Kimball, J. S., Jones, L. A., and McDonald, K. C. Satellite passive microwave detection of north america start of season. *Remote Sensing of Environment*, 123:324–333, 2012. doi: 10.1016/j.rse.2012.03.025.

Jones, M. O., Kimball, J. S., and Nemani, R. R. Asynchronous amazon forest canopy phenology indicates adaptation to both water and light availability. *Environmental Research Letters*, 9(12): 124021, 2014. doi: 10.1088/1748-9326/9/12/124021.

Jung, M., Reichstein, M., and Bondeau, A. Towards global empirical upscaling of fluxnet eddy covariance observations: validation of a model tree ensemble approach using a biosphere model. *Biogeosciences*, 6(10):2001–2013, 2009. doi: 10.5194/bg-6-2001-2009.

Jung, M., Reichstein, M., Margolis, H. A., Cescatti, A., Richardson, A. D., Arain, M. A., Arneth, A., Bernhofer, C., Bonal, D., Chen, J., Gianelle, D., Gobron, N., Kiely, G., Kutsch, W., Lasslop, G., Law, B. E., Lindroth, A., Merbold, L., Montagnani, L., Moors, E. J., Papale, D., Sottocornola, M., Vaccari, F., and Williams, C. Global patterns of land-atmosphere fluxes of carbon dioxide, latent heat, and sensible heat derived from eddy covariance, satellite, and meteorological observations. *Journal of Geophysical Research: Biogeosciences*, 116(G3), 2011. doi: 10.1029/2010JG001566.

Jung, M., Schwalm, C., Migliavacca, M., Walther, S., Camps-Valls, G., Koirala, S., Anthoni, P., Besnard, S., Bodesheim, P., Carvalhais, N., Chevallier, F., Gans, F., Goll, D., Haverd, V., Köhler, P., Ichii, K., Jain, A., Liu, J., Lombardozzi, D., Nabel, J., Nelson, J., O'Sullivan, M., Pallandt, M., Papale, D., Peters, W., Pongratz, J., Rödenbeck, C., Sitch, S., Tramontana, G., Walker, A., Weber, U., and Reichstein, M. Scaling carbon fluxes from eddy covariance sites to globe: synthesis and evaluation of the fluxcom approach. *Biogeosciences*, 17(5):1343–1365, 2020. doi: 10.5194/bg-17-1343-2020.

Kesselmeier, J., Ciccioli, P., Kuhn, U., Stefani, P., Biesenthal, T., Rottenberger, S., Wolf, A., Vitullo, M., Valentini, R., Nobre, A., Kabat, P., and Andreae, M. O. Volatile organic compound emissions in relation to plant carbon fixation and the terrestrial carbon budget. *Global Biogeochemical Cycles*, 16(4):73–1, 2002. doi: 10.1029/2001GB001813.

Kim, Y., Jackson, T., Bindlish, R., Lee, H., and Hong, S. Radar vegetation index for estimating the vegetation water content of rice and soybean. *IEEE Geoscience and Remote Sensing Letters*, 9(4): 564–568, 2012. doi: 10.1109/LGRS.2011.2174772.

Kitajima, K., Mulkey, S. S., Samaniego, M., and Joseph Wright, S. Decline of photosynthetic capacity with leaf age and position in two tropical pioneer tree species. *American Journal of Botany*, 89(12): 1925–1932, 2002. doi: 10.3732/ajb.89.12.1925.

Klein, T. The variability of stomatal sensitivity to leaf water potential across tree species indicates a continuum between isohydric and anisohydric behaviours. *Functional Ecology*, 28(6):1313–1320, 2014.

Kokoska, S. and Zwillinger, D. *CRC standard probability and statistics tables and formulae*. Crc Press, 2000. ISBN 978-0-8493-0026-4.

Konings, A., Williams, A., and Gentine, P. Sensitivity of grassland productivity to aridity controlled by stomatal and xylem regulation. *Nature Geoscience*, 10(4):284–288, 2017a. doi: 10.1038/ngeo2903.

Konings, A. G. and Gentine, P. Global variations in ecosystem-scale isohydricity. *Global change biology*, 23(2):891–905, 2017.

Konings, A. G., Yu, Y., Xu, L., Yang, Y., Schimel, D. S., and Saatchi, S. S. Active microwave observations of diurnal and seasonal variations of canopy water content across the humid african tropical forests. *Geophysical Research Letters*, 44(5):2290–2299, 2017b. doi: 10.1002/2016GL072388.

Konings, A. G., Rao, K., and Steele-Dunne, S. C. Macro to micro: microwave remote sensing of plant water content for physiology and ecology. *New Phytologist*, 223(3):1166–1172, 2019.

Körner, C. Paradigm shift in plant growth control. *Current opinion in plant biology*, 25:107–114, 2015.

Kumar, S. V., Holmes, T. R., Bindlish, R., Jeu, R. d., and Peters-Lidard, C. Assimilation of vegetation optical depth retrievals from passive microwave radiometry. *Hydrology and Earth System Sciences*, 24(7):3431–3450, 2020.

Lambers, H. and Oliveira, R. S. Plant water relations. In *Plant physiological ecology*, pages 187–263. Springer, Cham, 2019. doi: 10.1007/978-3-030-29639-1_5.

Lambers, H., Chapin III, F. S., and Pons, T. L. *Plant physiological ecology*. Springer Science & Business Media, 2008. URL `https://books.google.at/books/about/Plant_Physiological_Ecology.html?hl=de&id=PXBq6jsT5SYC`.

Lasslop, G., Reichstein, M., Papale, D., Richardson, A. D., Arneth, A., Barr, A., Stoy, P., and Wohlfahrt, G. Separation of net ecosystem exchange into assimilation and respiration using a light response curve approach: critical issues and global evaluation. *Global Change Biology*, 16(1):187–208, 2010. doi: 10.1111/j.1365-2486.2009.02041.x.

Lasslop, G., Migliavacca, M., Bohrer, G., Reichstein, M., Bahn, M., Ibrom, A., Jacobs, C., Kolari, P., Papale, D., Vesala, T., Wohlfahrt, G., and Cescatti, A. On the choice of the driving temperature for eddy-covariance carbon dioxide flux partitioning. *Biogeosciences*, 9(12):5243–5259, 2012. doi: 10.5194/bg-9-5243-2012.

Lavigne, M. and Ryan, M. Growth and maintenance respiration rates of aspen, black spruce and jack pine stems at northern and southern boreas sites. *Tree Physiology*, 17(8-9):543–551, 1997.

Lavigne, M., Franklin, S., and Hunt Jr, E. Estimating stem maintenance respiration rates of dissimilar balsam fir stands. *Tree Physiology*, 16(8):687–695, 1996. URL `https://www.researchgate.net/profile/Michael_Lavigne2/publication/8778227_Estimating_stem_maintenance_respiration_rates_of_dissimilar_balsam_fir_stands/links/02e7e51819154d8e72000000.pdf`.

Leuzinger, S., Manusch, C., Bugmann, H., and Wolf, A. A sink-limited growth model improves biomass estimation along boreal and alpine tree lines. *Global Ecology and Biogeography*, 22(8):924–932, 2013.

Li, L., Njoku, E. G., Im, E., Chang, P. S., and Germain, K. S. A preliminary survey of radio-frequency interference over the us in aqua amsr-e data. *IEEE Transactions on Geoscience and Remote Sensing*, 42(2):380–390, 2004.

Li, X., Wigneron, J.-P., Frappart, F., Fan, L., Ciais, P., Fensholt, R., Entekhabi, D., Brandt, M., Konings, A. G., Liu, X., Wang, M., Al-Yaari, A., and Moisy, C. Global-scale assessment and inter-comparison of recently developed/reprocessed microwave satellite vegetation optical depth products. *Remote Sensing of Environment*, 253:112208, 2021. doi: 10.1016/j.rse.2020.112208.

Litton, C. M., Raich, J. W., and Ryan, M. G. Carbon allocation in forest ecosystems. *Global Change Biology*, 13(10):2089–2109, 2007.

Liu, P.-W., Judge, J., DeRoo, R. D., England, A. W., Bongiovanni, T., and Luke, A. Dominant backscattering mechanisms at l-band during dynamic soil moisture conditions for sandy soils. *Remote Sensing of Environment*, 178:104–112, 2016. doi: 10.1016/j.rse.2016.02.062.

Liu, Y. Y., van Dijk, A. I., de Jeu, R. A., and Holmes, T. R. An analysis of spatiotemporal variations of soil and vegetation moisture from a 29-year satellite-derived data set over mainland australia. *Water Resources Research*, 45(7), 2009. doi: 10.1029/2008WR007187.

Liu, Y. Y., de Jeu, R. A., McCabe, M. F., Evans, J. P., and Van Dijk, A. I. Global long-term passive microwave satellite-based retrievals of vegetation optical depth. *Geophysical Research Letters*, 38 (18), 2011. doi: 10.1029/2011GL048684.

Liu, Y. Y., Evans, J. P., McCabe, M. F., de Jeu, R. A., van Dijk, A. I., Dolman, A. J., and Saizen, I. Changing climate and overgrazing are decimating mongolian steppes. *PloS one*, 8(2):e57599, 2013a. doi: 10.1371/journal.pone.0057599.

Liu, Y. Y., van Dijk, A. I., McCabe, M. F., Evans, J. P., and de Jeu, R. A. Global vegetation biomass change (1988–2008) and attribution to environmental and human drivers. *Global Ecology and Biogeography*, 22(6):692–705, 2013b. doi: 10.1111/geb.12024.

Liu, Y. Y., Van Dijk, A. I., de Jeu, R. A., Canadell, J. G., McCabe, M. F., Evans, J. P., and Wang, G. Recent reversal in loss of global terrestrial biomass. *Nature Climate Change*, 5(5):470–474, 2015.

Luyssaert, S., Inglima, I., Jung, M., Richardson, A. D., Reichstein, M., Papale, D., Piao, S., Schulze, E.-D., Wingate, L., Matteucci, G., Aragao, L., Aubinet, M., Beer, C., Bernhofer, C., Black, K., Bonal, D., Bonnefond, J.-M., Chambers, J., Ciais, P., Cook, B., Davis, K., Dolman, A., Gielen, B., Goulden, M., Grace, J., Granier, A., Grelle, A., Griffis, T., Grünwald, T., Guidolotti, G., Hanson, P., Harding, R., Hollinger, D., Hutyra, L., Kolari, P., Kruijt, B., Kutsch, W., Lagergren, F., Laurila, T., Law, B., Le Maire, G., Lindroth, A., Loustau, D., Malhi, Y., Mateus, J., Migliavacca, M., Misson, L., Montagnani, L., Moncrieff, J., Moors, E., Munger, J., Nikinmaa, E., Ollinger, S., Pita, G., Rebmann, C., Roupsard, O., Saigusa, N., Sanz, M., Seufert, G., Sierra, C., Smith, M.-L., Tang, J., Valentini, R., Vesala, T., and Janssens, I. CO2 balance of boreal, temperate, and tropical forests derived from a global database. *Global change biology*, 13(12):2509–2537, 2007. doi: 10.1111/j.1365-2486.2007.01439.x.

MacBean, N., Maignan, F., Bacour, C., Lewis, P., Peylin, P., Guanter, L., Köhler, P., Gómez-Dans, J., and Disney, M. Strong constraint on modelled global carbon uptake using solar-induced chlorophyll fluorescence data. *Scientific reports*, 8(1):1–12, 2018. doi: 10.1038/s41598-018-20024-w.

Maier, C. A., Zarnoch, S. J., and Dougherty, P. Effects of temperature and tissue nitrogen on dormant season stem and branch maintenance respiration in a young loblolly pine (pinus taeda) plantation. *Tree Physiology*, 18(1):11–20, 1998.

Martens, B., Miralles, D. G., Lievens, H., van der Schalie, R., de Jeu, R. A., Férnandez-Prieto, D., Beck, H. E., Dorigo, W. A., and Verhoest, N. E. Gleam v3: Satellite-based land evaporation and root-zone soil moisture. *Geoscientific Model Development Discussions*, pages 1–36, 2016. doi: 10.5194/gmd-2016-162.

Martens, B., Gonzalez Miralles, D., Lievens, H., Van Der Schalie, R., de Jeu, R. A., Fernández-Prieto, D., Beck, H. E., Dorigo, W., and Verhoest, N. Gleam v3: Satellite-based land evaporation and root-zone soil moisture. *Geoscientific Model Development*, 10(5):1903–1925, 2017.

Martínez-Vilalta, J. and Garcia-Forner, N. Water potential regulation, stomatal behaviour and hydraulic transport under drought: deconstructing the iso/anisohydric concept. *Plant, Cell & Environment*, 40(6):962–976, 2017.

Martínez-Vilalta, J., Sala, A., Asensio, D., Galiano, L., Hoch, G., Palacio, S., Piper, F. I., and Lloret, F. Dynamics of non-structural carbohydrates in terrestrial plants: a global synthesis. *Ecological Monographs*, 86(4):495–516, 2016.

Meesters, A. G., de Jeu, R. A., and Owe, M. Analytical derivation of the vegetation optical depth from the microwave polarization difference index. *IEEE Geoscience and Remote Sensing Letters*, 2 (2):121–123, 2005. doi: 10.1109/LGRS.2005.843983.

Melzer, T. Vegetation Modelling in WARP 6.0. In *Understanding the past, observing the present and protecting the future Vienna 2013*, Vienna, Austria, 2013.

Miralles, D. G., Holmes, T., de Jeu, R., Gash, J., Meesters, A., and Dolman, A. Global land-surface evaporation estimated from satellite-based observations. *Hydrology and Earth System Sciences*, 15 (2):453–469, 2011.

Miralles, D. G., Nieto, R., McDowell, N. G., Dorigo, W. A., Verhoest, N. E., Liu, Y. Y., Teuling, A. J., Dolman, A. J., Good, S. P., and Gimeno, L. Contribution of water-limited ecoregions to their own supply of rainfall. *Environmental Research Letters*, 11(12):124007, 2016. doi: 10.1088/1748-9326/ 11/12/124007.

Mo, T., Choudhury, B., Schmugge, T., Wang, J., and Jackson, T. A model for microwave emission from vegetation-covered fields. *Journal of Geophysical Research: Oceans*, 87(C13):11229–11237, 1982. doi: 10.1029/JC087iC13p11229.

Moesinger, L., Dorigo, W., de Jeu, R., van der Schalie, R., Scanlon, T., Teubner, I., and Forkel, M. The global long-term microwave vegetation optical depth climate archive (vodca). *Earth System Science Data*, 12(1):177–196, 2020.

Momen, M., Wood, J. D., Novick, K. A., Pangle, R., Pockman, W. T., McDowell, N. G., and Konings, A. G. Interacting effects of leaf water potential and biomass on vegetation optical depth. *Journal of Geophysical Research: Biogeosciences*, 122(11):3031–3046, 2017.

Monteith, J. Solar radiation and productivity in tropical ecosystems. *Journal of applied ecology*, 9(3): 747–766, 1972.

Morton, D. C., Nagol, J., Carabajal, C. C., Rosette, J., Palace, M., Cook, B. D., Vermote, E. F., Harding, D. J., and North, P. R. Amazon forests maintain consistent canopy structure and greenness during the dry season. *Nature*, 506(7487):221–224, 2014. doi: 10.1038/nature13006.

Muñoz-Sabater, J. First era5-land dataset to be released this spring. *ECMWF: Reding, UK*, 159, 2019.

Myneni, R. B., Hoffman, S., Knyazikhin, Y., Privette, J., Glassy, J., Tian, Y., Wang, Y., Song, X., Zhang, Y., Smith, G., Lotsch, A., Friedl, M., Morisette, J., Votava, P., Nemani, R., and Running, S. Global products of vegetation leaf area and fraction absorbed par from year one of modis data. *Remote sensing of environment*, 83(1-2):214–231, 2002. doi: 10.1016/S0034-4257(02)00074-3.

Nemani, R. R., Keeling, C. D., Hashimoto, H., Jolly, W. M., Piper, S. C., Tucker, C. J., Myneni, R. B., and Running, S. W. Climate-driven increases in global terrestrial net primary production from 1982 to 1999. *science*, 300(5625):1560–1563, 2003. doi: 10.1126/science.1082750.

Njoku, E. G., Ashcroft, P., Chan, T. K., and Li, L. Global survey and statistics of radio-frequency interference in amsr-e land observations. *IEEE Transactions on Geoscience and Remote Sensing*, 43(5):938–947, 2005.

Nunes, L., Lopes, D., Rego, F. C., and Gower, S. T. Aboveground biomass and net primary production of pine, oak and mixed pine–oak forests on the vila real district, portugal. *Forest Ecology and Management*, 305:38–47, 2013. doi: 10.1016/j.foreco.2013.05.034.

Odum, E. P. *Fundamentals of ecology*. WB Saunders company, 1959.

Olivares, E. and Medina, E. Water and nutrient relations of woody perennials from tropical dry forests. *Journal of Vegetation Science*, 3(3):383–392, 1992. doi: 10.2307/3235764.

O'Sullivan, M., Smith, W. K., Sitch, S., Friedlingstein, P., Arora, V. K., Haverd, V., Jain, A. K., Kato, E., Kautz, M., Lombardozzi, D., et al. Climate-driven variability and trends in plant productivity over recent decades based on three global products. *Global biogeochemical cycles*, 34(12): e2020GB006613, 2020. doi: 10.1029/2020GB006613.

Owe, M., de Jeu, R., and Walker, J. A methodology for surface soil moisture and vegetation optical depth retrieval using the microwave polarization difference index. *IEEE Transactions on Geoscience and Remote Sensing*, 39(8):1643–1654, 2001.

Owe, M., de Jeu, R., and Holmes, T. Multisensor historical climatology of satellite-derived global land surface moisture. *Journal of Geophysical Research: Earth Surface*, 113(F1):F01002, 2008. doi: 10.1029/2007JF000769.

Papagiannopoulou, C., Miralles, D., Dorigo, W. A., Verhoest, N., Depoorter, M., and Waegeman, W. Vegetation anomalies caused by antecedent precipitation in most of the world. *Environmental Research Letters*, 12(7):074016, 2017. doi: 10.1088/1748-9326/aa7145.

Pastorello, G., Trotta, C., Canfora, E., Chu, H., Christianson, D., Cheah, Y.-W., Poindexter, C., Chen, J., Elbashandy, A., Humphrey, M., Isaac, P., Polidori, D., Reichstein, M., Ribeca, A., van Ingen, C., Vuichard, N., Zhang, L., Amiro, B., Ammann, C., Arain, M. A., Ardö, J., Arkebauer, T., Arndt, S. K., Arriga, N., Aubinet, M., Aurela, M., Baldocchi, D., Barr, A., Beamesderfer, E., Marchesini, L. B., Bergeron, O., Beringer, J., Bernhofer, C., Berveiller, D., Billesbach, D., Black, T. A., Blanken, P. D., Bohrer, G., Boike, J., Bolstad, P. V., Bonal, D., Bonnefond, J.-M., Bowling, D. R., Bracho, R., Brodeur, J., Brümmer, C., Buchmann, N., Burban, B., Burns, S. P., Buysse, P., Cale, P., Cavagna, M., Cellier, P., Chen, S., Chini, I., Christensen, T. R., Cleverly, J., Collalti, A., Consalvo, C., Cook, B. D., Cook, D., Coursolle, C., Cremonese, E., Curtis, P. S., D'Andrea, E., da Rocha, H., Dai, X., Davis, K. J., Cinti, B. D., Grandcourt, A. d., Ligne, A. D., De Oliveira, R. C., Delpierre, N., Desai, A. R., Di Bella, C. M., Tommasi, P. d., Dolman, H., Domingo, F., Dong, G., Dore, S., Duce, P., Dufrêne, E., Dunn, A., Dušek, J., Eamus, D., Eichelmann, U., ElKhidir, H. A. M., Eugster, W., Ewenz, C. M., Ewers, B., Famulari, D., Fares, S., Feigenwinter, I., Feitz, A., Fensholt, R., Filippa, G., Fischer, M., Frank, J., Galvagno, M., Gharun, M., Gianelle, D., Gielen, B., Gioli, B., Gitelson, A., Goded, I., Goeckede, M., Goldstein, A. H., Gough, C. M., Goulden, M. L., Graf, A., Griebel, A., Gruening, C., Grünwald, T., Hammerle, A., Han, S., Han, X., Hansen, B. U., Hanson, C., Hatakka, J., He, Y., Hehn, M., Heinesch, B., Hinko-Najera, N., Hörtnagl, L., Hutley, L., Ibrom, A., Ikawa, H., Jackowicz-Korczynski, M., Janouš, D., Jans, W., Jassal, R., Jiang, S., Kato, T., Khomik, M., Klatt, J., Knohl, A., Knox, S., Kobayashi, H., Koerber, G., Kolle, O., Kosugi, Y., Kotani, A., Kowalski, A., Kruijt, B., Kurbatova, J., Kutsch, W. L., Kwon, H., Launiainen, S., Laurila, T., Law, B., Leuning, R., Li, Y., Liddell, M., Limousin, J.-M., Lion, M.,

Liska, A. J., Lohila, A., López-Ballesteros, A., López-Blanco, E., Loubet, B., Loustau, D., Lucas-Moffat, A., Lüers, J., Ma, S., Macfarlane, C., Magliulo, V., Maier, R., Mammarella, I., Manca, G., Marcolla, B., Margolis, H. A., Marras, S., Massman, W., Mastepanov, M., Matamala, R., Matthes, J. H., Mazzenga, F., McCaughey, H., McHugh, I., McMillan, A. M. S., Merbold, L., Meyer, W., Meyers, T., Miller, S. D., Minerbi, S., Moderow, U., Monson, R. K., Montagnani, L., Moore, C. E., Moors, E., Moreaux, V., Moureaux, C., Munger, J. W., Nakai, T., Neirynck, J., Nesic, Z., Nicolini, G., Noormets, A., Northwood, M., Nosetto, M., Nouvellon, Y., Novick, K., Oechel, W., Olesen, J. E., Ourcival, J.-M., Papuga, S. A., Parmentier, F.-J., Paul-Limoges, E., Pavelka, M., Peichl, M., Pendall, E., Phillips, R. P., Pilegaard, K., Pirk, N., Posse, G., Powell, T., Prasse, H., Prober, S. M., Rambal, S., Rannik, l., Raz-Yaseef, N., Rebmann, C., Reed, D., Dios, V. R. d., Restrepo-Coupe, N., Reverter, B. R., Roland, M., Sabbatini, S., Sachs, T., Saleska, S. R., Sánchez-Cañete, E. P., Sanchez-Mejia, Z. M., Schmid, H. P., Schmidt, M., Schneider, K., Schrader, F., Schroder, I., Scott, R. L., Sedlák, P., Serrano-Ortíz, P., Shao, C., Shi, P., Shironya, I., Siebicke, L., Šigut, L., Silberstein, R., Sirca, C., Spano, D., Steinbrecher, R., Stevens, R. M., Sturtevant, C., Suyker, A., Tagesson, T., Takanashi, S., Tang, Y., Tapper, N., Thom, J., Tomassucci, M., Tuovinen, J.-P., Urbanski, S., Valentini, R., van der Molen, M., van Gorsel, E., van Huissteden, K., Varlagin, A., Verfaillie, J., Vesala, T., Vincke, C., Vitale, D., Vygodskaya, N., Walker, J. P., Walter-Shea, E., Wang, H., Weber, R., Westermann, S., Wille, C., Wofsy, S., Wohlfahrt, G., Wolf, S., Woodgate, W., Li, Y., Zampedri, R., Zhang, J., Zhou, G., Zona, D., Agarwal, D., Biraud, S., Torn, M., and Papale, D. The fluxnet2015 dataset and the oneflux processing pipeline for eddy covariance data. *Scientific Data*, 7(1), 2020. doi: 10.1038/s41597-020-0534-3.

Paulik, C., Hahn, S., and Mistelbauer, T. Pytesmo: V0.3.0, 2015. URL https://zenodo.org/record/596422.

Piao, S., Luyssaert, S., Ciais, P., Janssens, I. A., Chen, A., Cao, C., Fang, J., Friedlingstein, P., Luo, Y., and Wang, S. Forest annual carbon cost: A global-scale analysis of autotrophic respiration. *Ecology*, 91(3):652–661, 2010.

Rao, K., Anderegg, W. R., Sala, A., Martínez-Vilalta, J., and Konings, A. G. Satellite-based vegetation optical depth as an indicator of drought-driven tree mortality. *Remote Sensing of Environment*, 227: 125–136, 2019.

Reichstein, M., Falge, E., Baldocchi, D., Papale, D., Aubinet, M., Berbigier, P., Bernhofer, C., Buchmann, N., Gilmanov, T., Granier, A., Grünwald, T., Havránková, K., Ilvesniemi, H., Janous, D., Knohl, A., Laurila, T., Lohila, A., Loustau, D., Matteucci, G., Meyers, T., Miglietta, F., Ourcival, J.-M., Pumpanen, J., Rambal, S., Rotenberg, E., Sanz, M., Tenhunen, J., Seufert, G., Vaccari, F., Vesala, T., Yakir, D., and Valentini, R. On the separation of net ecosystem exchange into assimilation and ecosystem respiration: review and improved algorithm. *Global change biology*, 11(9): 1424–1439, 2005. doi: 10.1111/j.1365-2486.2005.001002.x.

Ribaut, J.-M., Betran, J., Monneveux, P., and Setter, T. Drought tolerance in maize. In *Handbook of maize: its biology*, pages 311–344. Springer, New York, NY, 2009. doi: 10.1007/978-0-387-79418-1_16.

Rodríguez-Fernández, N. J., Mialon, A., Mermoz, S., Bouvet, A., Richaume, P., Al Bitar, A., Al-Yaari, A., Brandt, M., Kaminski, T., Le Toan, T., Kerr, Y. H., and Wigneron, J.-P. The high sensitivity

of smos l-band vegetation optical depth to biomass. *Biogeosciences Discussions*, 2018:1–20, 2018a. doi: 10.5194/bg-2018-49.

Rodríguez-Fernández, N. J., Mialon, A., Mermoz, S., Bouvet, A., Richaume, P., Al Bitar, A., Al-Yaari, A., Brandt, M., Kaminski, T., Le Toan, T., Kerr, Y., and Wigneron, J.-P. An evaluation of smos l-band vegetation optical depth (l-vod) data sets: high sensitivity of l-vod to above-ground biomass in africa. *Biogeosciences*, 15(14):4627–4645, 2018b. doi: 10.5194/bg-15-4627-2018.

Rogers, A., Medlyn, B. E., Dukes, J. S., Bonan, G., Von Caemmerer, S., Dietze, M. C., Kattge, J., Leakey, A. D., Mercado, L. M., Niinemets, Ü., Prentice, I. C., Serbin, S. P., Sitch, S., Way, D. A., and Zaehle, S. A roadmap for improving the representation of photosynthesis in earth system models. *New Phytologist*, 213(1):22–42, 2017. doi: 10.1111/nph.14283.

Running, S. and Mu, Q. MOD17a2h MODIS/Terra Gross Primary Productivity 8-Day L4 Global 500m SIN Grid V006, 2015.

Running, S., Mu, Q., and Zhao, M. Mod17a2h modis/terra gross primary productivity 8-day l4 global 500m sin grid v006. *NASA EOSDIS Land Processes DAAC*, 2015. doi: 10.5067/MODIS/MOD17A2H.006.

Running, S. W. Environmental control of leaf water conductance in conifers. *Canadian Journal of Forest Research*, 6(1):104–112, 1976. doi: 10.1139/x76-013.

Running, S. W., Nemani, R., Glassy, J. M., and Thornton, P. E. Modis daily photosynthesis (psn) and annual net primary production (npp) product (mod17) algorithm theoretical basis document. *University of Montana, SCF At-Launch Algorithm ATBD Documents (available online at: www. ntsg. umt. edu/modis/ATBD/ATBD_MOD17_v21. pdf)*, 1999.

Running, S. W., Thornton, P. E., Nemani, R., and Glassy, J. M. Global terrestrial gross and net primary productivity from the earth observing system. In *Methods in ecosystem science*, pages 44–57. Springer, New York, NY, 2000. doi: 10.1007/978-1-4612-1224-9_4.

Running, S. W., Nemani, R. R., Heinsch, F. A., Zhao, M., Reeves, M., and Hashimoto, H. A continuous satellite-derived measure of global terrestrial primary production. *Bioscience*, 54(6):547–560, 2004.

Ryan, M. G. Growth and maintenance respiration in stems of pinus contorta and picea engelmannii. *Canadian Journal of Forest Research*, 20(1):48–57, 1990. doi: 10.1139/x90-008.

Ryan, M. G. Effects of climate change on plant respiration. *Ecological Applications*, 1(2):157–167, 1991.

Ryan, M. G., Lavigne, M. B., and Gower, S. T. Annual carbon cost of autotrophic respiration in boreal forest ecosystems in relation to species and climate. *Journal of Geophysical Research: Atmospheres*, 102(D24):28871–28883, 1997.

Sanaullah, M., Chabbi, A., Rumpel, C., and Kuzyakov, Y. Carbon allocation in grassland communities under drought stress followed by 14c pulse labeling. *Soil Biology and Biochemistry*, 55:132–139, 2012.

Sapes, G., Roskilly, B., Dobrowski, S., Maneta, M., Anderegg, W. R., Martinez-Vilalta, J., and Sala, A. Plant water content integrates hydraulics and carbon depletion to predict drought-induced seedling mortality. *Tree physiology*, 39(8):1300–1312, 2019.

Savitzky, A. and Golay, M. J. Smoothing and differentiation of data by simplified least squares procedures. *Analytical chemistry*, 36(8):1627–1639, 1964.

Sawada, Y., Tsutsui, H., Koike, T., Rasmy, M., Seto, R., and Fujii, H. A field verification of an algorithm for retrieving vegetation water content from passive microwave observations. *IEEE Transactions on Geoscience and Remote Sensing*, 54(4):2082–2095, 2015. doi: 10.1109/TGRS.2015.2495365.

Scurlock, J. M., Johnson, K., and Olson, R. J. Estimating net primary productivity from grassland biomass dynamics measurements. *Global Change Biology*, 8(8):736–753, 2002. doi: 10.1046/j.1365-2486.2002.00512.x.

Servén, D. and Brummitt, C. pygam: generalized additive models in python. *Zenodo. DOI*, 10, 2018. doi: http://doi.org/10.5281/zenodo.1208723.

Servén, D., Brummitt, C., and Abedi, H. Dswah/Pygam: V0.5.4, 2018. URL https://zenodo.org/record/1208723.

Sitch, S., Friedlingstein, P., Gruber, N., Jones, S. D., Murray-Tortarolo, G., Ahlström, A., Doney, S. C., Graven, H., Heinze, C., Huntingford, C., et al. Recent trends and drivers of regional sources and sinks of carbon dioxide. *Biogeosciences*, 12(3):653–679, 2015. doi: 10.5194/bg-12-653-2015.

Smith, N. G. and Dukes, J. S. Plant respiration and photosynthesis in global-scale models: incorporating acclimation to temperature and co 2. *Global change biology*, 19(1):45–63, 2013.

Song, L., Li, Y., Ren, Y., Wu, X., Guo, B., Tang, X., Shi, W., Ma, M., Han, X., and Zhao, L. Divergent vegetation responses to extreme spring and summer droughts in southwestern china. *Agricultural and Forest Meteorology*, 279:107703, 2019. doi: 10.1016/j.agrformet.2019.107703.

Sun, Y., Frankenberg, C., Jung, M., Joiner, J., Guanter, L., Köhler, P., and Magney, T. Overview of solar-induced chlorophyll fluorescence (sif) from the orbiting carbon observatory-2: Retrieval, cross-mission comparison, and global monitoring for gpp. *Remote Sensing of Environment*, 209:808–823, 2018. doi: 10.1016/j.rse.2018.02.016.

Suyker, A. E., Verma, S. B., Burba, G. G., and Arkebauer, T. J. Gross primary production and ecosystem respiration of irrigated maize and irrigated soybean during a growing season. *Agricultural and Forest Meteorology*, 131(3-4):180–190, 2005. doi: 10.1016/j.agrformet.2005.05.007.

Teubner, I. E., Forkel, M., Jung, M., Liu, Y. Y., Miralles, D. G., Parinussa, R., van der Schalie, R., Vreugdenhil, M., Schwalm, C. R., Tramontana, G., Camps-Valls, G., and Dorigo, W. A. Assessing the relationship between microwave vegetation optical depth and gross primary production. *International journal of applied earth observation and geoinformation*, 65:79–91, 2018. doi: https://doi.org/10.1016/j.jag.2017.10.006.

Teubner, I. E., Forkel, M., Camps-Valls, G., Jung, M., Miralles, D. G., Tramontana, G., van der Schalie, R., Vreugdenhil, M., Mösinger, L., and Dorigo, W. A. A carbon sink-driven approach to estimate gross primary production from microwave satellite observations. *Remote Sensing of Environment*, 229:100–113, 2019. doi: https://doi.org/10.1016/j.rse.2019.04.022.

Tian, F., Wigneron, J., Ciais, P., Chave, J., Ogée, J., Peñuelas, J., Ræbild, A., Domec, J., Tong, X., Brandt, M., Mialon, A., Rodriguez-Fernandez, N., Tagesson, T., Al-Yaari, A., Kerr, Y., Chen,

C., Myneni, R. B., Zhang, W., Ardö, J., and Fensholt, R. Coupling of ecosystem-scale plant water storage and leaf phenology observed by satellite. *Nature Ecology & Evolution*, 2:1428–1435, 2018.

Tian, F., Brandt, M., Liu, Y. Y., Verger, A., Tagesson, T., Diouf, A. A., Rasmussen, K., Mbow, C., Wang, Y., and Fensholt, R. Remote sensing of vegetation dynamics in drylands: Evaluating vegetation optical depth (vod) using avhrr ndvi and in situ green biomass data over west african sahel. *Remote Sensing of Environment*, 177:265–276, 2016. doi: 10.1016/j.rse.2016.02.056.

Tian, F., Brandt, M., Liu, Y. Y., Rasmussen, K., and Fensholt, R. Mapping gains and losses in woody vegetation across global tropical drylands. *Global change biology*, 23(4):1748–1760, 2017. doi: 10.1111/gcb.13464.

Tjoelker, M. G., Oleksyn, J., and Reich, P. B. Modelling respiration of vegetation: evidence for a general temperature-dependent q10. *Global Change Biology*, 7(2):223–230, 2001.

Tjoelker, M. G., Oleksyn, J., Reich, P. B., and Żytkowiak, R. Coupling of respiration, nitrogen, and sugars underlies convergent temperature acclimation in pinus banksiana across wide-ranging sites and populations. *Global Change Biology*, 14(4):782–797, 2008.

Tramontana, G., Ichii, K., Camps-Valls, G., Tomelleri, E., and Papale, D. Uncertainty analysis of gross primary production upscaling using random forests, remote sensing and eddy covariance data. *Remote Sensing of Environment*, 168:360–373, 2015. doi: 10.1016/j.rse.2015.07.015.

Tramontana, G., Jung, M., Schwalm, C. R., Ichii, K., Camps-Valls, G., Ráduly, B., Reichstein, M., Arain, M. A., Cescatti, A., Kiely, G., Merbold, L., Serrano-Ortiz, P., Sickert, S., Wolf, S., and Papale, D. Predicting carbon dioxide and energy fluxes across global fluxnet sites with regression algorithms. *Biogeosciences*, 13(14):4291–4313, 2016. doi: 10.5194/bg-13-4291-2016.

Turner, D. P., Ritts, W. D., Cohen, W. B., Maeirsperger, T. K., Gower, S. T., Kirschbaum, A. A., Running, S. W., Zhao, M., Wofsy, S. C., Dunn, A. L., Law, B. E., Campbell, J. L., Oechel, W. C., Kwon, H. J., Meyers, T. P., Small, E. E., Kurc, S. A., and Gamon, J. A. Site-level evaluation of satellite-based global terrestrial gross primary production and net primary production monitoring. *Global Change Biology*, 11(4):666–684, 2005. doi: https://doi.org/10.1111/j.1365-2486.2005.00936.x.

Turner, D. P., Ritts, W. D., Cohen, W. B., Gower, S. T., Running, S. W., Zhao, M., Costa, M. H., Kirschbaum, A. A., Ham, J. M., Saleska, S. R., and Ahl, D. E. Evaluation of modis npp and gpp products across multiple biomes. *Remote sensing of environment*, 102(3-4):282–292, 2006. doi: https://doi.org/10.1016/j.rse.2006.02.017.

USGS. Global 30-Arc-Second Elevation Data Set (GTOPO30), 1996. URL `http://lpdaac.usgs.gov`.

van der Schalie, R., Kerr, Y. H., Wigneron, J.-P., Rodríguez-Fernández, N. J., Al-Yaari, A., and de Jeu, R. A. Global smos soil moisture retrievals from the land parameter retrieval model. *International journal of applied earth observation and geoinformation*, 45:125–134, 2016. doi: 10.1016/j.jag.2015.08.005.

van der Schalie, R., de Jeu, R. A., Kerr, Y., Wigneron, J.-P., Rodríguez-Fernández, N. J., Al-Yaari, A., Parinussa, R. M., Mecklenburg, S., and Drusch, M. The merging of radiative transfer based

surface soil moisture data from smos and amsr-e. *Remote Sensing of Environment*, 189:180–193, 2017.

Van Marle, M., Van Der Werf, G., de Jeu, R., and Liu, Y. Annual south american forest loss estimates based on passive microwave remote sensing (1990–2010). *Biogeosciences*, 13(2):609–624, 2016. doi: 10.5194/bg-13-609-2016.

Vanderwel, M. C., Slot, M., Lichstein, J. W., Reich, P. B., Kattge, J., Atkin, O. K., Bloomfield, K. J., Tjoelker, M. G., and Kitajima, K. Global convergence in leaf respiration from estimates of thermal acclimation across time and space. *New Phytologist*, 207(4):1026–1037, 2015.

Verbesselt, J., Umlauf, N., Hirota, M., Holmgren, M., Van Nes, E. H., Herold, M., Zeileis, A., and Scheffer, M. Remotely sensed resilience of tropical forests. *Nature Climate Change*, 6(11):1028–1031, 2016. doi: 10.1038/nclimate3108.

Vicente-Serrano, S. M., Beguería, S., López-Moreno, J. I., Angulo, M., and El Kenawy, A. A new global 0.5 gridded dataset (1901–2006) of a multiscalar drought index: comparison with current drought index datasets based on the palmer drought severity index. *Journal of Hydrometeorology*, 11(4):1033–1043, 2010.

Vose, J. M. and Ryan, M. G. Seasonal respiration of foliage, fine roots, and woody tissues in relation to growth, tissue n, and photosynthesis. *Global Change Biology*, 8(2):182–193, 2002.

Vreugdenhil, M., Dorigo, W. A., Wagner, W., de Jeu, R. A., Hahn, S., and Van Marle, M. J. Analyzing the vegetation parameterization in the tu-wien ascat soil moisture retrieval. *IEEE Transactions on Geoscience and Remote Sensing*, 54(6):3513–3531, 2016. doi: 10.1109/TGRS.2016.2519842.

Vreugdenhil, M., Hahn, S., Melzer, T., Bauer-Marschallinger, B., Reimer, C., Dorigo, W. A., and Wagner, W. Assessing vegetation dynamics over mainland australia with metop ascat. *IEEE Journal of Selected Topics in Applied Earth Observations and Remote Sensing*, 10(5):2240–2248, 2017. doi: 10.1109/JSTARS.2016.2618838.

Vreugdenhil, M., Wagner, W., Bauer-Marschallinger, B., Pfeil, I., Teubner, I., Rüdiger, C., and Strauss, P. Sensitivity of sentinel-1 backscatter to vegetation dynamics: An austrian case study. *Remote Sensing*, 10(9):1396, 2018. doi: 10.3390/rs10091396.

Vreugdenhil, M., Navacchi, C., Bauer-Marschallinger, B., Hahn, S., Steele-Dunne, S., Pfeil, I., Dorigo, W., and Wagner, W. Sentinel-1 cross ratio and vegetation optical depth: A comparison over europe. *Remote Sensing*, 12(20):3404, 2020.

Wagner, F., Rossi, V., Stahl, C., Bonal, D., and Hérault, B. Asynchronism in leaf and wood production in tropical forests: a study combining satellite and ground-based measurements. *Biogeosciences*, 10 (11):7307–7321, 2013a. doi: 10.5194/bg-10-7307-2013.

Wagner, W., Lemoine, G., and Rott, H. A method for estimating soil moisture from ers scatterometer and soil data. *Remote sensing of environment*, 70(2):191–207, 1999. doi: 10.1016/S0034-4257(99)00036-X.

Wagner, W., Hahn, S., Kidd, R., Melzer, T., Bartalis, Z., Hasenauer, S., Figa-Saldana, J., De Rosnay, P., Jann, A., Schneider, S., Komma, J., Kubu, G., Brugger, K., Aubrecht, C., Züger, J., Gangkofner,

U., Kienberger, S., Brocca, L., Wang, Y., Blöschl, G., Eitzinger, J., Steinnocher, K., Zeil, P., and Rubel, F. The ascat soil moisture product: A review of its specifications, validation results, and emerging applications. *Meteorologische Zeitschrift*, 2013b. doi: 10.1127/0941-2948/2013/0399.

Waring, R., Landsberg, J., and Williams, M. Net primary production of forests: a constant fraction of gross primary production? *Tree physiology*, 18(2):129–134, 1998. doi: 10.1093/treephys/18.2.129.

Wigneron, J.-P., Fan, L., Ciais, P., Bastos, A., Brandt, M., Chave, J., Saatchi, S., Baccini, A., and Fensholt, R. Tropical forests did not recover from the strong 2015–2016 el niño event. *Science advances*, 6(6):eaay4603, 2020. doi: 10.1126/sciadv.aay4603.

Wild, B., Teubner, I., Moesinger, L., Zotta, R.-M., Forkel, M., van der Schalie, R., Sitch, S., and Dorigo, W. A. VODCA2GPP – a new global, long-term (1988–2020) GPP dataset from microwave remote sensing. *Earth System Science Data Discussions*, pages 1–37, 2021. doi: 10.5194/essd-2021-209.

Willmott, C. J. On the validation of models. *Physical geography*, 2(2):184–194, 1981. doi: 10.1080/02723646.1981.10642213.

Woodhouse, I. *Introduction to Microwave Remote Sensing*. CRC Press, 2005. ISBN 978-0-203-64652-6.

Wright, S. J. and Van Schaik, C. P. Light and the phenology of tropical trees. *The American Naturalist*, 143(1):192–199, 1994. URL http://www.jstor.org/stable/2462858?seq=1#page_scan_tab_contents.

Wu, M., Scholze, M., Kaminski, T., Voßbeck, M., and Tagesson, T. Using smos soil moisture data combining co2 flask samples to constrain carbon fluxes during 2010–2015 within a carbon cycle data assimilation system (ccdas). *Remote Sensing of Environment*, 240:111719, 2020. doi: 10.1016/j.rse.2020.111719.

Würth, M. K., Pelaez-Riedl, S., Wright, S. J., and Körner, C. Non-structural carbohydrate pools in a tropical forest. *Oecologia*, 143(1):11–24, 2005.

Wythers, K. R., Reich, P. B., and Bradford, J. B. Incorporating temperature-sensitive q10 and foliar respiration acclimation algorithms modifies modeled ecosystem responses to global change. *Journal of Geophysical Research: Biogeosciences*, 118(1):77–90, 2013.

Yang, F., Ichii, K., White, M. A., Hashimoto, H., Michaelis, A. R., Votava, P., Zhu, A.-X., Huete, A., Running, S. W., and Nemani, R. R. Developing a continental-scale measure of gross primary production by combining modis and ameriflux data through support vector machine approach. *Remote Sensing of Environment*, 110(1):109–122, 2007. doi: 10.1016/j.rse.2007.02.016.

Zha, T., Kellomäki, S., Wang, K.-Y., Ryyppö, A., and Niinistö, S. Seasonal and annual stem respiration of scots pine trees under boreal conditions. *Annals of Botany*, 94(6):889–896, 2004.

Zhang, Y. and Ye, A. Would the obtainable gross primary productivity (gpp) products stand up? a critical assessment of 45 global gpp products. *Science of The Total Environment*, 783:146965, 2021. doi: 10.1016/j.scitotenv.2021.146965.

Zhang, Y., Xiao, X., Zhou, S., Ciais, P., McCarthy, H., and Luo, Y. Canopy and physiological controls of gpp during drought and heat wave. *Geophysical Research Letters*, 43(7):3325–3333, 2016a.

Zhang, Y., Xiao, X., Wu, X., Zhou, S., Zhang, G., Qin, Y., and Dong, J. A global moderate resolution dataset of gross primary production of vegetation for 2000–2016. *Scientific data*, 4:170165, 2017. doi: 10.1038/sdata.2017.165.

Zhang, Y., Zhou, S., Gentine, P., and Xiao, X. Can vegetation optical depth reflect changes in leaf water potential during soil moisture dry-down events? *Remote Sensing of Environment*, 234:111451, 2019. doi: 10.1016/j.rse.2019.111451.

Zhang, Y., Guanter, L., Berry, J. A., van der Tol, C., and Joiner, J. Can we retrieve vegetation photosynthetic capacity paramter from solar-induced fluorescence? In *2016 IEEE International Geoscience and Remote Sensing Symposium (IGARSS)*, pages 1711–1713. IEEE, 2016b. doi: 10. 1109/IGARSS.2016.7729437.

Zhao, M., Heinsch, F. A., Nemani, R. R., and Running, S. W. Improvements of the modis terrestrial gross and net primary production global data set. *Remote sensing of Environment*, 95(2):164–176, 2005. doi: 10.1016/j.rse.2004.12.011.

Zribi, M., Chahbi, A., Shabou, M., Lili-Chabaane, Z., Duchemin, B., Baghdadi, N., Amri, R., and Chehbouni, A. Soil surface moisture estimation over a semi-arid region using envisat asar radar data for soil evaporation evaluation. *Hydrology and Earth System Sciences*, 15(1):345–358, 2011. doi: 10.5194/hess-15-345-2011.